Mystifying photoluminescence mechanisms

Unraveling and exploiting non-ideal
behavior of luminescent nanomaterials

PhD thesis, Utrecht University
Mystifying photoluminescence mechanisms: unraveling and exploiting non-ideal behavior of luminescent nanomaterials
Mark J. J. Mangnus

Printing: Ridderprint, www.ridderprint.nl
ISBN: 978-94-6483-736-0
DOI: https://doi.org/10.33540/2118

Cover: Chameleons are mystifying creatures, changing color in response to their environment. Although chameleons are most well known for their excellent camouflage, they are equally capable of taking on eye-catching colors when it suits them. Chameleons produce different colors by reflecting specific colors of light off their skin, which contains guanine nanocrystals in a stretchable periodic arrangement (*Nat. Commun*. **2015**, *6*, 6368).

Cover art is based on a photograph by Oleksandr Kuzmin on Unsplash.

Mystifying photoluminescence mechanisms

Unraveling and exploiting non-ideal behavior of luminescent nanomaterials

Raadselachtige mechanismes van fotoluminescentie

Het ontrafelen en benutten van de imperfecties van lichtgevende nanomaterialen

(met een samenvatting in het Nederlands)

Proefschrift

ter verkrijging van de graad van doctor aan de
Universiteit Utrecht
op gezag van de
rector magnificus, prof. dr. H.R.B.M. Kummeling,
ingevolge het besluit van het college voor promoties
in het openbaar te verdedigen op

14 februari 2024 des middags te 2.15 uur

door

Mark Joris Jeroen Mangnus

geboren op 6 juni 1996
te Goes

Promotor:
Prof. dr. B.M. Weckhuysen
Prof. dr. A. van Blaaderen

Copromotor:
dr. F.T. Rabouw

Beoordelingscommissie:
Prof. dr. P.C.A. Bruijnincx
Prof. dr. M. Dijkstra
Prof. dr. B. Ehrler
dr. ir. P. Geiregat
Prof. dr. P. van der Straten

Dit werk werd financieel ondersteund door het *Netherlands Center for Multiscale Catalytic Energy Conversion* (MCEC), een NWO Zwaartekrachtprogramma gefinancierd door het Nederlandse Ministerie van Onderwijs, Cultuur en Wetenschap.

Table of contents

Chapter 1

Introduction

Our twenty-first-century society would cease to exist without artificial light sources. After sunset we continue our daily lives simply by turning on the lights. Possibly just as important, lighting in displays allows us to digest information visually from a computer, television or smartphone screen. Importantly, the desired color and brightness of emitted light differs from one application to another. For example, we wish to have screen displays with vivid colors and strong contrast, while in traffic we require powerful bright lighting to guarantee safety, and at home we wish to have dim and warmer lighting to create a cozy atmosphere. Almost all artificial light sources are based on luminescent materials, but different types are required to meet the standards in different applications. We address two different classes of photoluminescent materials in this thesis: quantum dots and lanthanide-doped nanocrystals. These two different types of photoluminescent materials will be briefly introduced here, and the relevant theoretical background is provided in **Chapter 2**.

1.1 | Variations and fluctuations of single-quantum-dot emission properties

Quantum dots (QDs) are nanocrystals (NCs) of semiconductor materials. They have received much attention since their discovery in the 1990s, in particular because the color of their bright photoluminescence is tunable by controlling the size of the NCs. This means that QDs with the same chemical composition emit different colors of light, just because their dimensions are different. Utilizing a range of different NC compositions and sizes, one can obtain all colors of visible light (and more).[1] QDs are an important component in several types of devices, including television displays, white LEDs, lasers and luminescent solar concentrators.[2–5]

In the last decade chemists have made large progress by controlling the size and shape of QDs in a structurally monodisperse batch. Puzzlingly, however, studies at the single-particle level have shown that even nominally identical QDs may have very different emission colors. This negatively affects the color purity of QDs and hampers their incorporation in devices. Combating such heterogeneities in emission properties is an essential step to pave the way for a next generation of QDs but requires a better understanding of their photophysics. As our current understanding of emission from QDs is largely based on experiments performed on the workhorse material of CdSe, the mechanism of emission remains debated for many newly discovered types QDs—including the classes of less toxic III–V and ternary I-III-VI_2 QDs, with InP and $CuInS_2$ as the best-known examples.

In **Chapter 3**, we use single-particle spectroscopy to shed light on the peculiar emission properties of $CuInS_2$ QDs. We observe that the emission properties fluctuate in a manner that is fundamentally different from the behavior of CdSe-based QDs. We develop a quantum-mechanical framework to model this spectral diffusion and ascribe the observed behavior in terms of an excited state with an internal dipole moment. The internal dipole moment originates from the hole, which localizes on copper-related sites that may be off-center. Variations in the hole localization site lead to large variations in the emission properties of $CuInS_2$ QDs, which become even more pronounced in the presence of an external electric field.

Single-particle spectroscopy allows one to characterize particle-to-particle variations in emission properties that are otherwise obscured by ensemble averaging. However, the method of measuring QDs one after another is inherently slow, and a user-selection bias is inevitable. In **Chapter 4**, we develop a high-throughput method to characterize many single-quantum-dot emission spectra simultaneously, without a user-selection bias (Figure 1.1). We use this method of multiparticle spectroscopy (MPS) to map out particle-to-particle variations of

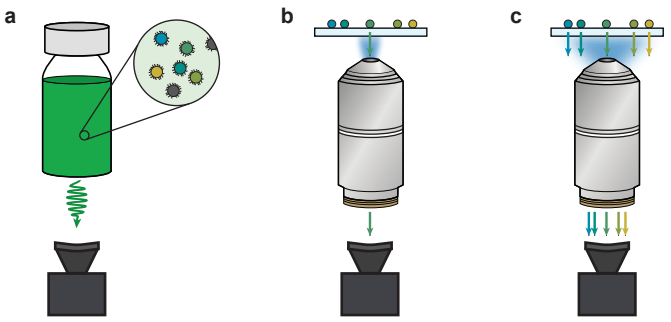

Figure 1.1 | Spectroscopy of quantum dots. (a) Most commonly, spectroscopy of QDs is performed at the ensemble level. Such methods are generally cheap and fast, but the results only reflect average emission properties. In other words, particle-to-particle variations within a batch, as well as fluctuations of single-QD properties, remain obscured. **(b)** Single-particle spectroscopy allows one to measure fluctuations of single-QD properties. One-by-one characterization of multiple QDs from the same batch is, however, time-consuming. This makes it hard to acquire statistically relevant information of single-QD properties within the batch. **(c)** In multiparticle spectroscopy, the emission from tens to hundreds of single QDs is measured simultaneously. As such, the experimentalist collects statistically strong information of batch properties in a short amount of time. A drawback of multiparticle spectroscopy is that the choice of detectors is limited: only pixel-array detectors are capable of monitoring the emission properties of multiple single QDs separately. This in principle excludes single-photon detectors, which operate at much better time resolutions.

emission properties within a batch of InP-based QDs. At the same time, we study fluctuations of single-particle properties at time scales ranging from milliseconds to minutes. Compared to a batch of superior CdSe-based QDs with well-defined emission properties, the batch of InP-based QDs features large particle-to-particle variations. Based on the distributions and correlations in single-particle properties, which could not have been mapped without a statistically strong method like MPS, we propose that the excited state of InP-based QDs is fundamentally different to CdSe-based QDs.

1.2 | Impact of the local environment on the emission from lanthanides in nanocrystals

The photoluminescence from lanthanide-based phosphors originates from atomic transitions of optically active lanthanide ions that take up lattice sites of an otherwise optically inactive host crystal. The color of their photoluminescence is defined by several sharp emission lines, which originate from a complex but well-defined energy-level structure. In commercial phosphors these emission lines contribute to an improved color rendering. For instance, a white LED may be supplemented with the narrow emission lines of Eu^{3+} in the red to create warm white light.[6] Other than lighting, lanthanide-doped materials have applications in photovolta-

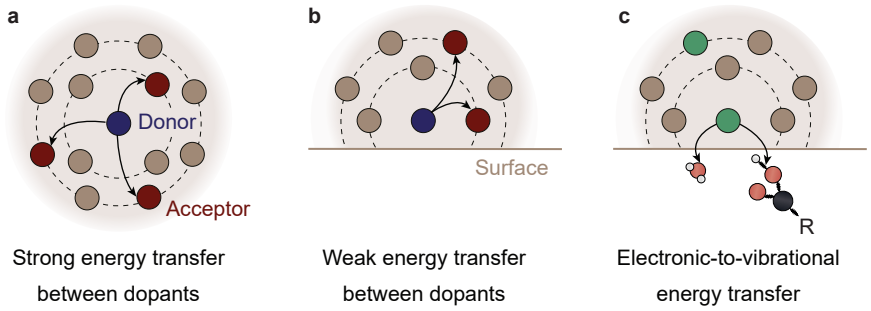

Figure 1.2 | Energy transfer processes in lanthanide-doped nanocrystals. (a) Many lanthanide-doped phosphors rely on energy transfer: a donor ion absorbs incident light and transfers the energy to nearby acceptors, which emit light of the desired color. **(b)** Close to the surface of a nanocrystal, energy transfer is less efficient because donor ions are coordinated by fewer acceptors. This affects the photoluminescence output, as emission from acceptors becomes less likely. **(c)** Another process that can happen at the nanocrystal surface is electronic-to-vibrational energy transfer (EVET), where the lanthanide dopant transfers its energy to molecular vibrations. The EVET-induced photoluminescence quenching depends on the type of molecules at the surface.

ics,[7] background-free bioimaging and biolabeling,[8–13] and sensing (e.g. temperature[14,15]). Nanocrystalline phosphors are required for various applications, for instance to prevent scattering losses, for temperature sensing with high spatial resolution, or to guarantee mobility of the NCs in narrow volumes. It is often assumed that the photoluminescence from lanthanide ions in NCs is size-independent—much unlike the strongly size-dependent optical properties of quantum dots—and hardly affected by their local environment. In this thesis, we challenge this consensus by demonstrating two examples where the emission properties of lanthanide-doped NCs change substantially as a result of differences in particle size, or due to the presence of specific molecules in proximity of the NCs surface (Figure 1.2).

In **Chapter 5**, we study NCs co-doped with two different types of lanthanide ions. Such nanophosphors are generally designed such that a donor lanthanide species (strongly) absorbs incident light and transfers the energy to an acceptor lanthanide ion of another species, which subsequently emit light of the desired color. We show experimentally that the efficiency of energy transfer (ET) between dopants is lower in NCs compared to their bulk counterparts. These finite-size effects become especially pronounced for NCs smaller than ~12 nm, where a large fraction of dopant ions resides close to the NC surface. Hampered ET from the donor species to the acceptor impacts the photoluminescence output, which is an important consideration for the design of future nanophosphors. We demonstrate that the efficiency of ET from the donor to the acceptor can nonetheless be boosted by slowing down the competitive pathway of photon emission from the donor ion.

Compared to dopants in a bulk(-like) environment, lanthanide ions close to the NC surface are less likely to transfer energy to other dopant ions but are often also less likely to emit photons themselves. The latter effect is caused by electronic-to-vibrational energy transfer (EVET), where an excited lanthanide ion transfers (part of) its energy to vibrations of molecules that reside close to the NC surface. While it is in general regarded as a deleterious effect that reduces the photoluminescence output, we show in **Chapter 6** that EVET can be

exploited as a mechanism to extract information about the type of molecules present in the local environment of lanthanide-doped NCs. In particular, we show that specific emission lines of lanthanide dopants are quenched only by specific molecules.

Chapter 2

Theoretical background

2.1 | Quantum dots

For over three decades, semiconductor nanocrystals, or quantum dots (QDs), have attracted much attention due to their uniquely bright and tunable photoluminescence (PL). Upon irradiation with blue/UV light, QDs emit a color of light that depends on their size (Figure 2.1a). The underlying process is that electrons from the valence band (VB) are excited across the band gap into the conduction band (CB), forming an electron–hole pair (the exciton). Excitons recombine by emitting photons with an energy determined by the band gap (Figure 2.1b), a material property that is crucially impacted by the QD size through quantum-confinement effects. In this thesis, we study photoluminescence from different types of quantum dots and attempt to identify the nature of the excited state. The relevant theoretical background is described in this section.

2.1.1 The effective-mass approximation

In the effective-mass approximation (EMA), the size-dependent properties of QDs are calculated based on the electronic band structure of the bulk semiconductor.[16–18] Electronic states in semiconductors are described as

$$\psi(\mathbf{r}) = \phi(\mathbf{r})u(\mathbf{r}), \tag{2.1}$$

where $u(\mathbf{r})$ is a basis function that describes the hybridization of atomic orbitals in the QD unit cell, and $\phi(\mathbf{r})$ is an envelope function that specifies the spatial extent. In QDs, $\phi(\mathbf{r})$ is restricted by the dimensions of the nanocrystal. In the EMA, the behavior of charge carriers is defined in terms of the electron and hole effective masses m_e^* and m_h^*. The effective masses are defined by the curvature of the VB and CB in the bulk electronic band structure and may deviate substantially from the electron rest mass m_0. Treating the charge carriers in QDs as a particle in a box with infinite potential barriers, and using the carrier effective mass, the (time-independent) Schrödinger equation becomes

$$\left(-\frac{\hbar^2}{2m^*}\nabla^2 + V(\mathbf{r})\right)\phi(\mathbf{r}) = E\phi(\mathbf{r}), \tag{2.2}$$

where $V(\mathbf{r})$ describes the potential well of the particle in a box. Assuming a spherical box of radius a, the electronic states of the QD—eigenfunctions of Eq. 2.2—are defined in terms of the principal, azimuthal and magnetic quantum numbers n, l, and m. The eigenfunctions, or wave functions, have a radial and an angular component:

$$\phi_{nlm}(\mathbf{r}) = R_{nl}(r)Y_l^m(\theta,\varphi). \tag{2.3}$$

The angular component can be described by the spherical harmonics $Y_l^m(\theta,\varphi)$, just like for the hydrogen orbitals. Electronic states with quantum number $l = 0, 1, 2, \ldots$ have s-, p-, d-, … symmetries and are named 1S, 1P, 1D, 2S, etc. Differences with the electronic states of the hydrogen atom are a consequence of the different potential landscape, which alters the radial component of the envelope functions $\phi(\mathbf{r})$ and lifts the restrictions in terms of allowed combinations n and l. The radial components are

$$R_{nl} = A_{nl}j_l(\chi_{nl}r/a), \tag{2.4}$$

with $j_l(x)$ the spherical Bessel function of order l, χ_{nl} the n^{th} zero of $j_l(x)$ and A_{nl} a normalization constant. The confinement energies—eigenvalues of Eq. 2.2—have an inverse-square dependence on the QD radius a,

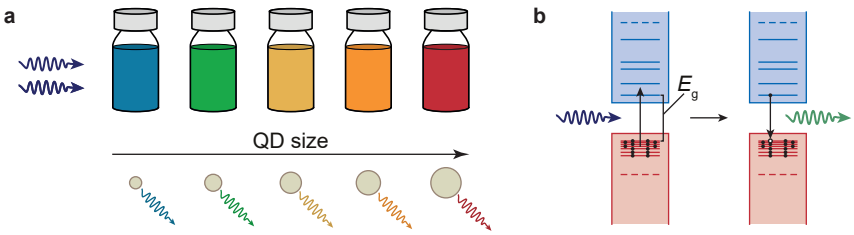

Figure 2.1 | Photoluminescence from QDs. (**a**) Upon irradiation with high-energy photons, QDs emit light with a wavelength that depends on the dimensions of the nanocrystals. Larger nanocrystals emit at longer wavelengths. (**b**) Using light with an energy that exceeds the band gap (E_g), a QD can be excited by promoting an electron from the occupied VB levels (red) to the empty CB (blue) and forming a hole in the VB (red). A photon is emitted when the CB electron and VB hole recombine. The energy of the emitted photon is determined by the size-dependent band-gap energy.

$$E_{nl} = \frac{\hbar^2 \chi_{nl}^2}{2m^* a^2}, \tag{2.5}$$

explaining the size-dependence of electronic properties. These confinement energies are a perturbation to the carrier energies in the bulk semiconductor. The theory of quantum dots focuses on the size-dependent effects imposed on the envelope functions $\phi(\mathbf{r})$. Therefore, the community often uses the term "wave function" for just the envelope function $\phi(\mathbf{r})$ rather the full wave function $\psi(\mathbf{r})$.[16–18]

2.1.2 Excitons in quantum dots

In the limit of strong confinement, an exciton behaves almost as if it were composed of a non-interacting electron–hole pair. In this simple picture, we assume that the wave function of the lowest exciton state is built up from the 1S particle-in-a-box electron and hole wave functions ($\psi_{1,0,0}$; Eq. 2.3 and Figure 2.2a):

$$\Psi_0^{(0)} = \psi_{1,0,0}^{e} \psi_{1,0,0}^{h}. \tag{2.6}$$

We treat the attractive Coulomb interaction between the electron–hole pair as a small perturbation that stabilizes (that is, lowers the energy of) the exciton. Using $\chi_{1,0} = \pi$, the exciton energy

$$E_0^0 = E_g + \frac{\hbar^2 \pi^2}{2a^2}\left[\frac{1}{m_e^*} + \frac{1}{m_h^*}\right] - 1.79\frac{e^2}{4\pi\varepsilon\varepsilon_0 a}, \tag{2.7}$$

with E_g the bulk semiconductor band gap. The second term describes the confinement energies of the electron and hole, and the third term the Coulomb stabilization of the exciton, with ε and ε_0 are the vacuum permittivity and dielectric constant of the semiconductor. We neglect the effects of dielectric contrast between the QD and the surrounding medium.

Beyond the assumption of strong confinement, a more exact way of treating Coulomb interactions is by explicitly taking into account that the electron and hole wave functions deform with respect to the 1S state to optimize overlap. The exact exciton wave function can be expressed in terms of a chosen set of electron and hole basis functions, such as the particle-in-a-box wave functions (Eq. 2.3):

$$\Psi_X(\mathbf{r}_e, \mathbf{r}_h) = \sum_{n_e,l_e,m_e,n_h,l_h,m_h} c_{n_e,l_e,m_e} \psi^e_{n_e,l_e,m_e}(\mathbf{r}_e) c_{n_h,l_h,m_h} \psi^h_{n_h,l_h,m_h}(\mathbf{r}_h). \quad (2.8)$$

Variational theory states that the "real" exciton state is the state with the lowest possible energy. Minimizing the exciton energy,

$$E_X = \langle \Psi_X | H | \Psi_X \rangle, \quad (2.9)$$

with the Hamiltonian (neglecting again the effects of dielectric contrast between the QD and the surrounding medium)

$$H = H^e_0(\mathbf{r}_e) + H^h_0(\mathbf{r}_h) + V_C(\mathbf{r}_e, \mathbf{r}_h), \quad (2.10)$$

by optimizing the coefficients c_{n_e,l_e,m_e} and c_{n_h,l_h,m_h} thus yields the solution for Ψ_X—given that a sufficient number of basis functions is used. In Eq. 2.10, the first two terms are the particle-in-an-infinite-spherical-box Hamiltonians of the electron and hole (with eigenvalues given by Eq. 2.5). The third term describes the electron–hole Coulomb attraction:

$$V_C(\mathbf{r}_e, \mathbf{r}_h) = -\frac{e^2}{4\pi\varepsilon\varepsilon_0} \frac{1}{|\mathbf{r}_e - \mathbf{r}_h|}. \quad (2.11)$$

The outcome of variational theory is that the exciton is not perfectly described by the $\psi_{1,0,0}$ (1S) wave functions, but instead contains contributions of higher particle-in-a-box states to optimize Coulomb attractions. The most important deformation with respect to the strong-confinement limit is mixing in of some 2S ($\psi_{2,0,0}$) character in the wave function of the hole (Figure 2.2b–d).

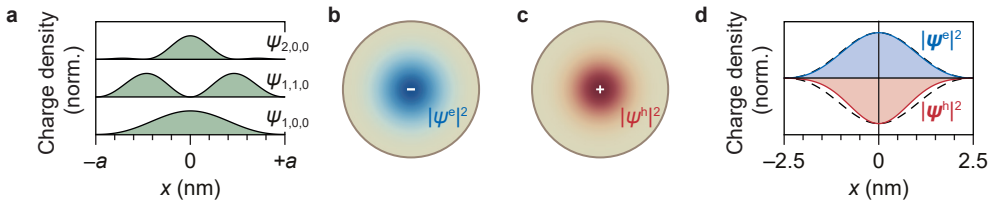

Figure 2.2 | Electron and hole wave functions in QDs. (**a**) Charge density of relevant particle-in-a-spherical box wave functions (Eq. 2.3), shown as a line trace through the center of the QD. (**b**) Two-dimensional crosscut of the electron charge density, calculated using variational theory. The charge density is specified by the shade of blue (**c**) Same as **b**, but for the hole charge density (red). (**d**) Same as **b**–**c**, but in one dimension. Dashed lines indicate the spatial extent of the electron and hole charge densities in the limit of strong confinement. Variational theory reveals that the Coulomb interaction is a small attractive force that pulls both the electron and hole charge densities toward the QD center. The hole wave function features a larger deformation than the electron due to the higher effective mass (weaker quantum confinement). Values used to calculate panels **b**–**d** are based on CdSe:[18,19] $m_e = 0.11\, m_0$, $m_h = 1.14\, m_0$, $\varepsilon = 10$.

2.1.3 Structural imperfections of quantum dots

The most common procedure to synthesize QDs bottom-up is via colloidal methods. The surface termination of QDs is in principle determined by the stability of different crystal facets in the presence of stabilizing passivating surface ligands, which are typically long amphiphilic organic molecules such as oleic acid and trioctylphosphine. Unpassivated surface atoms are notorious traps with energy levels within the band gap of the QD. The possibility of charge-carrier trapping on such trap states, followed by non-radiative recombination, reduces the photoluminescence efficiency of the QD. A typical strategy to prevent such surface-related carrier trapping is to encapsulate the QD core within a shell or multiple shells of a different semiconductor material with a wider band gap. The wider band gap prevents delocalization of the electron and/or hole into the shell region, and thus shields them from trap states at the QD surface. Common core–shell QD structures are e.g. CdSe/CdS and InP/ZnSe, where CdS and ZnSe have a wider band gap than CdSe and InP (see **Chapter 3**).

2.1.4 Fluctuations of single quantum-dot properties

The emission properties of single QDs are often unstable. Fluctuations of the single-particle emission spectrum and intensity manifest as spectral diffusion and PL blinking (Figure 2.3),[20–22] and occur spontaneously at ambient conditions. Experimentally, such spontaneous fluctuations have been intentionally reproduced by placing QDs in a tunable electric field between electrodes (Figure 2.4a). The leading hypothesis is that QDs experience external electric fields due to the dynamic nature of the surface, with mobile ligands or external charges hopping from one trap state to another. The electric field strengths required for spectral diffusion of the magnitude observed experimentally, can be produced by two opposite charges on either side of the QD (Figure 2.4b)—a scenario that is easily produced in case of, for instance, a surface vacancy or missing ligand.

An external electric field polarizes the exciton by pulling apart electron and hole charge densities and thereby lowers the energy through the quantum-confined Stark effect (QCSE). We model the effect of an external electric potential V_{ext} by including it as a term to the

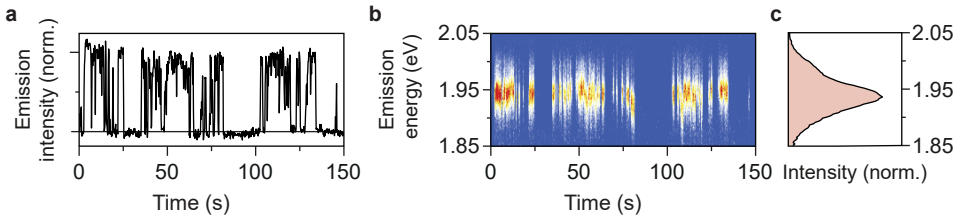

Figure 2.3 | Fluctuations of single-QD emission properties. (**a**) PL intensity time trace of a single InP/ZnSe QD, featuring clear blinking between an ON-state and an OFF-state. (**b**) Same experiment as in a, but showing the time trace of the single-QD emission spectrum. The PL intensity is specified by the color and increases from blue to yellow to red. The QD spectrum fluctuates over time (spectral diffusion). (**c**) The time-integrated single-QD spectrum corresponding to the time trace in **b**. Temporal fluctuations of the spectrum lead to spectral broadening and reduce the color purity of the PL. Experimental methods are described in **Chapter 4**. InP/ZnSe QDs were synthesized by Jur de Wit.

Hamiltonian in Eq. 2.10. In the limit of strong confinement, the QCSE is a small perturbation to the lowest exciton state (built up of 1S electron and hole wave functions; Eq. 2.7). Assuming a homogeneous electrostatic field (see Figure 2.4b), $V_{ext}(\mathbf{r}) = \mathbf{F} \cdot \mathbf{r}$, the Stark shift (up to second order) is

$$\Delta E = \langle \Psi_0^{(0)} | V_{ext} | \Psi_0^{(0)} \rangle + \sum_i \frac{\left| \langle \Psi_0^{(0)} | V_{ext} | \Psi_i^{(0)} \rangle \right|^2}{E_0^{(0)} - E_i^{(0)}} = -\xi F^2, \tag{2.12}$$

where only the second-order term survives. The polarizability ξ has contributions of both the electron and hole wave functions, which depend on the effective mass and the volume in which the carriers are confined:

$$\xi = \xi_e + \xi_h = 0.036 \frac{e^2}{\hbar^2} \left(m_e a_e^4 + m_h a_h^4 \right). \tag{2.13}$$

Eq. 2.13 can be used, for example, to calculate the exciton polarizabiliy of spherical CdSe/CdS core–shell QDs, where the electron is delocalized over the entire QD with radius a_e, and the hole is confined to the CdSe core with radius a_h. Besides the Stark shift of the exciton energy, the external electric field modifies the exciton ground state by mixing in a contribution of higher-energy particle-in-a-box states—similar to the effect of electron–hole Coulomb

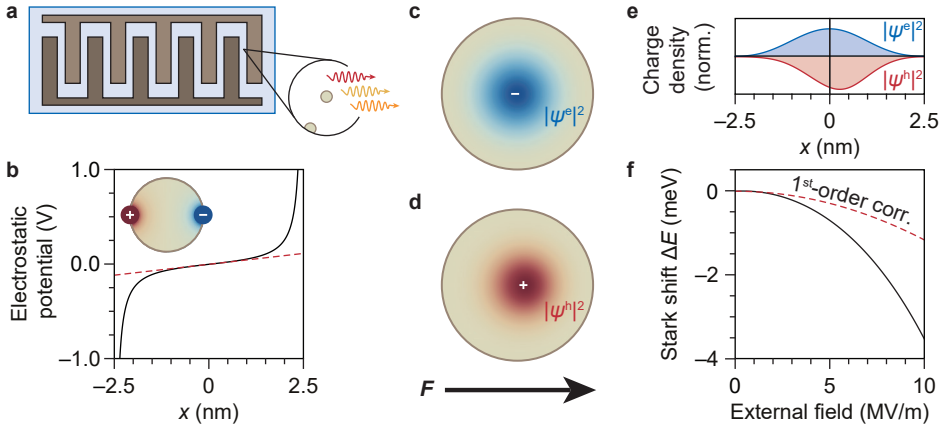

Figure 2.4 | Impact of external fields on the excited state of a QD. (a) Experimentally, modulation of the electric field around a QD induces spectral shifts comparable to the spectral fluctuations that occur spontaneously in the absence of electric fields. (**b**) Electrostatic potential induced by two oppositely charged species on either side of the QD, as shown in the inset, as a function of the position in the QD. The electrostatic potential is approximately homogeneous within the QD, except for regions close to the surface charges. The electric field in the QD is approximately described by the relation $F = q/2\pi\varepsilon\varepsilon_0 a^2 = 45\ \mathrm{MVm^{-1}}$ (red dashed line). (**c**) Charge density of the electron, shown as a two-dimensional crosscut, with a homogeneous electric field of $10\ \mathrm{MVm^{-1}}$ across the QD. The charge density is specified by the shade of blue. (**d**) Same as **c**, but for the hole charge density (red). (**e**) Same as **c**–**d**, but as a line trace through the center of the QD, showing that the external field pulls the electron and hole charge densities apart and thus polarizes the exciton. (**f**) Polarization of the exciton in an external electric field results in a Stark shift of the emission energy. Values used to calculate panels **b**–**f** are based on CdSe:[18,19] $m_e = 0.11\, m_0$, $m_h = 1.14\, m_0$, $\varepsilon = 10$.

attraction described earlier in this chapter. Variational theory describes the QCSE as mixing in of 1P-character in the exciton ground state (Figure 2.4c–e). At large electric field strengths, deformation of electron and hole charge distributions can become very large, inducing dipole moments up to 10-100 D, so that the strong-confinement Stark shift predicted by Eq. 2.12 is no longer accurate (Figure 2.4f).

2.2 | Lanthanide-doped nanocrystals

The lanthanide series comprises the elements with atomic numbers ranging from 57 to 71. These elements are most abundant in the trivalent oxidation state and have an electron configuration similar to that of the noble gas xenon, but with an additional n electrons in the 4f shell: $[Xe]4f^n$, with an empty 4f shell for La^{3+} ($n = 0$) and a completely filled shell for Lu^{3+} ($n = 14$). Most trivalent lanthanide ions absorb and emit light in the visible–infrared range.

From a chemical viewpoint, 4f-electrons can be considered "spectators", as they are localized close to the nucleus and effectively screened from the environment by electrons in the more delocalized 5s- and 5p-orbitals. In terms of their chemical properties all lanthanide ions—together with Sc^{3+} and Y^{3+}—are essentially equivalent: their chemistry is unaffected by the number of spectator electrons in the 4f-shell. Most common lanthanide-based phosphors are designed by doping lanthanide ions into insulator nanocrystals. Well-known examples are $Y_2Al_5O_{12}:Ce^{3+}$ (YAG:Ce^{3+}), $NaYF_4:Er^{3+},Yb^{3+}$, and phosphors based on $LaPO_4:Tb^{3+}$ or $LaPO_4:Eu^{3+}$, where optically active lanthanide ions substitute a fraction of the sites belonging to optically inactive ions (here: Y^{3+} and La^{3+}).[6,23,24]

Except for Ce^{3+} ($4f^1$), the optical transitions of trivalent lanthanide ions involve a redistribution of electrons among the hydrogen-like 4f-states (Figure 2.5), which are characterized by their orbital angular momentum (–3, –2, …, +2, +3, depending on the orbital) and spin angular momentum (–½, +½ for spin-up or spin-down, depending on the orbital). Each of the 14 available single-electron states can be occupied by one electron at most, so that lanthanides with electron configuration $4f^n$ have $\binom{14}{n}$ unique multi-electron states. In the simplest picture, considering only the kinetic energy of electrons and their attractive Coulomb interaction with the nucleus, all of these multi-electron states are degenerate. The degeneracy is lifted due to electron–electron repulsions (different for electrons in different orbitals), and spin–orbit coupling induces a further speciation of energy levels.

In the absence of strong crystal-field effects, optical transitions between the different multi-electron states of lanthanides are sharply defined regardless of the chemical environment (Figure 2.6a). The energy-level structure of lanthanide ions is ladder-like, as

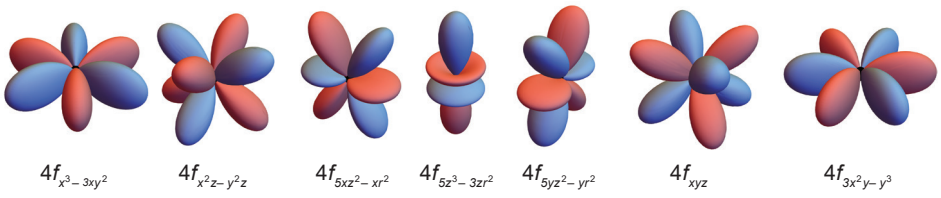

Figure 2.5 | Hydrogenic 4f-orbitals. Surface plots of the seven unique hydrogenic 4f-orbitals (not to scale). The real part of the wave functions is shown, with the phase indicated by the blue and red colors.

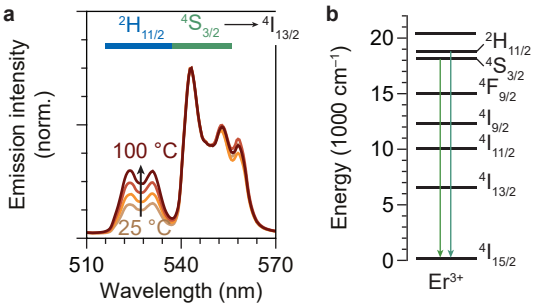

Figure 2.6 | Optical transitions in the erbium ion. (**a**) Emission spectrum of $NaYF_4$ nanocrystals, co-doped with Er^{3+}(2%) and Yb^{3+}(18%), obtained under near-infrared excitation. The relative populations of the $^4S_{3/2}$ and $^2H_{11/2}$ levels—and also the relative emission intensities—follow a Boltzmann distribution, as the energy gap is of the same order as the thermal energy (approximately 750 cm^{-1} versus a thermal energy of 207 cm^{-1} at room temperature). (**b**) Energy-level diagram of the Er^{3+} ion. The two emission bands highlighted in a originate from the two thermally coupled optical transitions from the $^4S_{3/2}$ and $^2H_{11/2}$ levels to the $^4I_{15/2}$ ground state.

often represented in the famous Dieke diagram (shown for the erbium ion in Figure 2.6b).[25–27] The nomenclature of multi-electron states is based on the $^{2S+1}L_J$ term symbols, specified by the total orbital angular momentum L (giving an S-, P-, D-, F-, …, term for L = 0, 1, 2, 3, …), the total spin angular momentum D, and the total angular momentum $J = L+S$. The degeneracy of each level is $2J+1$.

2.3 | Excited-state dynamics of luminescent materials

Following an excitation event, luminescent materials may spontaneously emit a photon and thereby relax to a lower-lying energy level—most commonly but not necessarily the ground state. Besides radiative decay, the emitter may also relax via competing nonradiative pathways. The photoluminescence quantum yield (PLQY) of the emitter depends on the rates of radiative decay Γ_{rad} and nonradiative decay Γ_{nr}:

$$\mathrm{PLQY} = \frac{\Gamma_{rad}}{\Gamma_{rad} + \Gamma_{nr}}. \tag{2.14}$$

2.3.1 Radiative and nonradiative decay

The radiative decay rate is given by Fermi's golden rule,

$$\Gamma_{rad} = \frac{2\pi}{\hbar}|V|^2\rho, \tag{2.15}$$

where V is the matrix element describing how strongly the radiative transition couples to the electromagnetic field of light, and ρ is the local density of optical states (LDOS; i.e. the number of available photon states at the position of the emitter). While excitonic transitions in QDs couple strongly to the electromagnetic field of light, this is not the case for the intra-

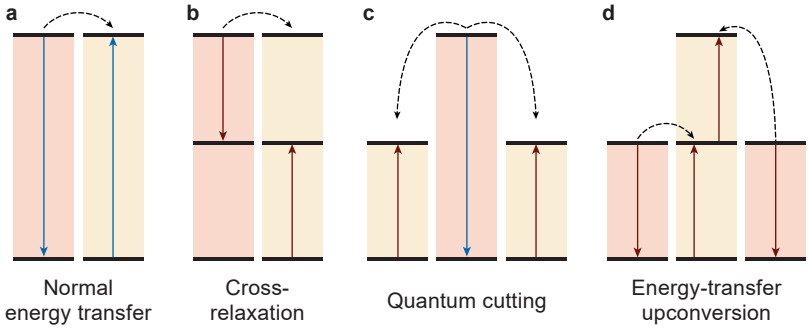

Figure 2.7 | Important energy-transfer processes. (**a**) The most common type of energy transfer is energy transfer (ET) between a donor (orange) in the excited state and an acceptor (yellow) in the ground state. As a result of ET, the donor relaxes back to the ground state and excites the acceptor to a resonant energy level. (**b**) Cross-relaxation is a type of energy transfer where the donor transfers part of its excited-state energy to an acceptor. (**c**) Quantum cutting, or downconversion) is the process where a single donor in a highly excited state transfers its energy to two or more acceptors that can emit multiple low-energy photons. (**d**) Upconversion is the reverse process of quantum cutting, where two donor ions (sequentially or simultaneously) transfer their energy to a single acceptor, which can in turn emit a high-energy photon.

configurational 4f–4f transitions of lanthanide ions. As a result, characteristic radiative decay rates of QDs are on the order of ns^{-1}, while 4f–4f transitions are much slower: on the order of ms^{-1}.

Depending on the local environment of the emitter, nonradiative decay pathways may exist such as (multi-phonon) relaxation and energy transfer (ET). The most common type of ET is of the Förster type,[28] which occurs via coupling of transition dipoles of an excited donor and an acceptor with a resonant energy level (Figure 2.7a). While ET is possible from one luminescent center to another center of the same species (in that case we call it energy migration), it may also occur between different species. In fact, we demonstrate in **Chapter 6** that an excited lanthanide ion can act as a donor to excite a vibrational mode of a nearby molecule. After transferring energy to molecular vibrations, of the order of 500–4000 cm^{-1}, the lanthanide ion remains in an (lower) excited state, from which it can emit a different color of light (schematic in Figure 2.7b).

The ET rate Γ_{ET} depends strongly on the donor–acceptor spacing R:

$$\Gamma_{ET} = \frac{C_{ET}}{R^6}. \tag{2.16}$$

The energy-transfer strength C_{ET} (with units of $m^6\,s^{-1}$) depends on the oscillator strengths of the donor and acceptor transitions, and their spectral overlap. The Förster radius,

$$R_0 = \left(\frac{C_{ET}}{\Gamma_{rad}}\right)^6, \tag{2.17}$$

is a useful parameter to quantify the competition between radiative decay of the donor and ET. It is defined as the donor–acceptor spacing at which radiative decay and ET are equally probable.

Although nonradiative decay pathways often reduce the quantum efficiency, some phosphors rely on ET from one species to another. The general design is that light of one color is strongly absorbed by a donor species, which transfers the energy to an acceptor that emits light of the desired color. The so-called processes of upconversion[29] and quantum cutting[30,31] are extreme examples (Figure 2.7c,d).[31] Lanthanide-based upconversion and quantum-cutting phosphors are promising materials to reshape the solar spectrum to better match the band gap of silicon solar cells and thereby drastically increase the energy-conversion efficiency.[7,32–34]

2.3.2 Decay dynamics

To extract information about decay dynamics, the typical experimental procedure is to excite a population of luminescent centers with a short laser pulse and measure the emission intensity as a function of the delay time. The number of photons detected at any delay time after the laser pulse is proportional to the number of luminescent centers in the excited state. The emission intensity decays mono-exponentially (Figure 2.8a–d) in case all emitters have the same decay rate Γ, i.e. the sum of radiative and nonradiative decay rates is equal:

$$I(t) = I_0 e^{-\Gamma t}. \tag{2.18}$$

Here, I_0 is the emission intensity directly after the laser pulse and t is the delay time between the laser pulse and detection of the emitted photon. Multi-exponential decay dynamics (Figure 2.8e,f) are obtained when multiple luminescent centers with different decay dynamics are measured, or in case the decay dynamics of a single emitter change during the course of

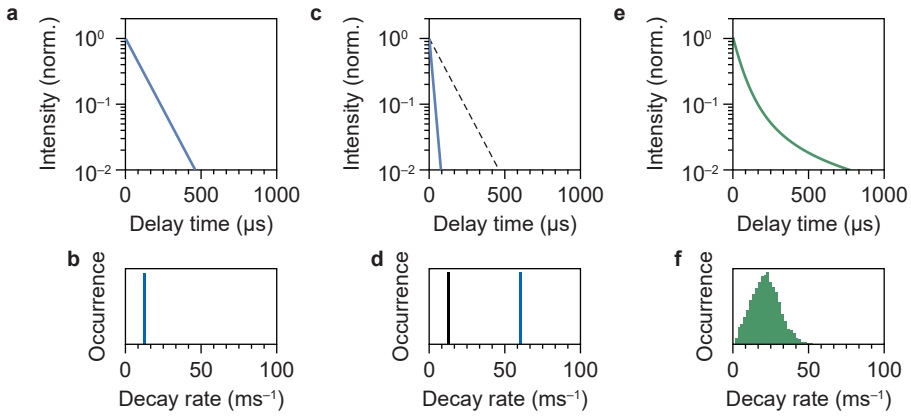

Figure 2.8 | Measuring photoluminescence decay dynamics. (**a**–**b**) Single-exponential decay is observed when the sample features a well-defined decay rate among all emitters. This is common for lanthanide ions in an environment where no significant nonradiative quenching pathways occur. (**c**–**d**) Introducing additional (nonradiative) decay pathways increases the total decay rate. This happens for instance upon introducing efficient ET acceptors. (**e**–**f**) Multi-exponential decay dynamics are observed when the sample features a range of different decay rates.

the measurement (see e.g. **Chapter 3**):

$$I(t) = I_0 \sum_{i=1} N e^{-\Gamma_i t}. \tag{2.19}$$

Introducing nonradiative decay pathways, such as inducing ET by incorporating acceptors ions, results in an acceleration of the decay dynamics. We demonstrate in **Chapter 5** and **6** that the competition between radiative decay and ET can be controlled by varying the concentration of acceptor ions or by varying the acceptor strength (C_{ET} in Eq. 2.16).

Chapter 3

Unusual spectral diffusion of single $CuInS_2$ quantum dots sheds light on the mechanism of radiative decay

This chapter is based on:

Unusual spectral diffusion of single $CuInS_2$ quantum dots sheds light on the mechanism of radiative decay. *Nano Lett.* **2021**, *21*, 658–665

Hinterding, S.O.M.; Mangnus, M.J.J.; Prins, P.T.; Jöbsis, H.J.; Busatto, S.; Vanmaekelbergh, D.; de Mello Donega, C.; Rabouw, F.T.

The luminescence of $CuInS_2$ quantum dots (QDs) is slower and spectrally broader than that of many other types of QDs. The origin of this anomalous behavior is still under debate. Single-QD experiments could help settle this debate, but studies by different groups have yielded conflicting results. Here, we study the photophysics of single core-only $CuInS_2$ and core–shell $CuInS_2$/CdS QDs. Both types of single QDs exhibit broad PL spectra with fluctuating peak position and single-exponential photoluminescence decay with a slow but fluctuating lifetime. Spectral diffusion of $CuInS_2$-based QDs is qualitatively and quantitatively different from CdSe-based QDs. The differences reflect the dipole moment of the $CuInS_2$ excited state, and hole localization on a preferred site in the QD. Our results unravel the highly dynamic photophysics of $CuInS_2$ QDs and highlight the power of the analysis of single-QD property fluctuations.

3.1 | Introduction

Semiconductor nanocrystals (quantum dots, QDs) are promising luminophores for use in numerous applications, such as displays and bioimaging.[35] While CdSe- and perovskite-based QDs are most studied, Cd- and Pb-free alternatives have also seen rapid development in recent years. QDs based on $CuInS_2$ (CIS) are one of these alternatives.[36,37] They are particularly interesting for use in luminescent solar concentrators[38–44] as they exhibit large global Stokes shifts, minimizing reabsorption losses. This peculiar property, along with broad photoluminescence (PL) line widths (ensemble full-width at half-maximum, FWHM ~400 meV)[11] and slow multi-exponential PL decay (PL lifetime ~200–400 ns),[45] shows that the photophysics of CIS QDs differ qualitatively from those of other types of QDs. In most other types of QDs (e.g., those based on CdSe, lead chalcogenide, or perovskite), luminescence occurs through recombination of delocalized quantum-confined electrons and holes.[46] In contrast, no consensus has yet been reached on the luminescence mechanism of CIS QDs and a number of different mechanisms has been proposed.[47–60] Recent optical transient absorption,[51,53,54,56,61] X-ray transient absorption,[62] and electrochemical[63–65] studies strongly support a mechanism in which a delocalized electron recombines with a localized hole, although other mechanisms are still claimed.[66,67] Striking similarities between the PL properties of CIS, Cu^+:CdSe, and Cu^+:InP suggest that the hole localizes on a Cu atom.[68]

Single-particle spectroscopy has proven essential to understand various aspects of the photophysics of QDs, as it yields data that are not obscured by ensemble-averaging.[69–72] Unfortunately, CIS QDs are notoriously unstable under the harsh excitation conditions used in single-QD experiments.[57,60] Consequently, single-particle studies on CIS-based QDs are scarce[57,60,73,74] and achieve limited data quality compared to studies on other types of QDs. Most strikingly, Whitham et al. reported broad single-QD PL line widths (minimum FWHM: 190 meV) from individual core–shell CIS/CdS QDs,[57] while Zang et al. found narrow PL line widths (minimum FWHM: 60 meV) from individual core–shell CIS/ZnS QDs.[60] A possible origin for these contrasting results is interdiffusion of Cu^+ and Zn^{2+} during overgrowth of a ZnS shell on CIS QDs,[75] as these two elements (in contrast to Cd^{2+}) have similar ionic radii.[76] The limited and conflicting data make it difficult to draw definite conclusions on the intrinsic photophysics of CIS nanomaterials.

Here, we study the PL properties of individual core-only CIS and core–shell CIS/CdS QDs. Careful sample optimization allows us to measure single-QD PL of both core-only CIS and core–shell CIS/CdS QDs for several minutes before irreversible photobleaching. We establish that the intrinsic PL properties of core-only CIS QDs are retained in core–shell CIS/CdS QDs. Variations between individual core–shell CIS/CdS QDs show the effect of inhomogeneous broadening on PL ensemble spectra and decay dynamics. Fluctuations in single-QD

PL properties over timescales of seconds to minutes provide insight into the emission mechanism. Spectral diffusion in CIS QDs is quantitatively and qualitatively different from that reported for CdSe QDs, consistent with radiative recombination of a delocalized electron with a Cu-localized hole. The correlations between the fluctuating PL peak position and PL lifetime provide evidence that the hole always localizes on a preferential Cu site in the QD. For a few QDs, we observe that the preferential Cu site changes. Quantum-mechanical calculations show that the dipolar character of the excited state underlies the strong fluctuations in PL energy and lifetime. These new insights into the emission mechanism of CIS-based QDs will be useful for the optimization of the optoelectronic properties of this class of materials.

3.2 | Results and discussion

We study core-only chalcopyrite CIS QDs of ~2.4 nm. These QDs are Cu-rich (atomic ratio Cu:In = 1.0 : 0.78). The core–shell CIS/CdSe QDs exhibit the same crystal structure, with an estimated particle size of 3.0 nm. Our sample preparation procedure allowed for single-QD measurements for several minutes before photobleaching. Details regarding the sample preparation, as well as extended data with additional measurements on 32 QDs that are not shown here, are provided in the publication on which this Chapter is based: *Nano Lett.* **2021**, *21*, 658–665.[77]

3.2.1 Comparison of core-only $CuInS_2$ and core–shell $CuInS_2$/CdS quantum dots

Figure 3.1 compares the single-QD PL properties of core-only CIS and core–shell CIS/CdS QDs. Both core-only CIS and core–shell CIS/CdS QDs exhibit PL blinking, characterized by fluctuations between periods of high intensity, and periods of lower intensity (Figure 3.1a,b). Both core-only CIS and core–shell CIS/CdS QDs are single-photon emitters, as evidenced by anti-bunching in the second-order correlation function $g^{(2)}(\tau)$ (Figure 3.1c,d). In the absence

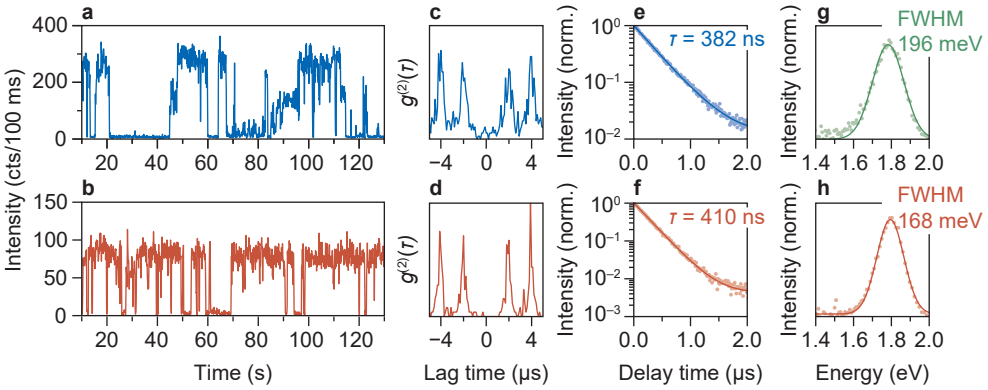

Figure 3.1 | Top row: results from single-QD measurements on two different core-only CIS QDs, bottom row: results from similar experiments on one CIS/CdS core/shell QD. (**a**,**b**) PL intensity as a function of time. (**c**,**d**) Second-order correlation function $g^{(2)}(\tau)$. (**e**,**f**) PL decay curve, constructed from time periods in which the QD was ON. (**e**) IPL ≥ 200 cts/100 ms, (**f**) IPL ≥ 65 cts/100 ms. Lines are fits to single-exponential decay with a constant background. (**g**,**h**) ON-state PL spectrum, integrated over (**g**) 6.5 s and (**h**) 91.3 s. Lines are Gaussian fits. As indicated by the color, data in **g** were measured on a different core-only CIS QD than the data depicted in **a**,**c**,**e**.

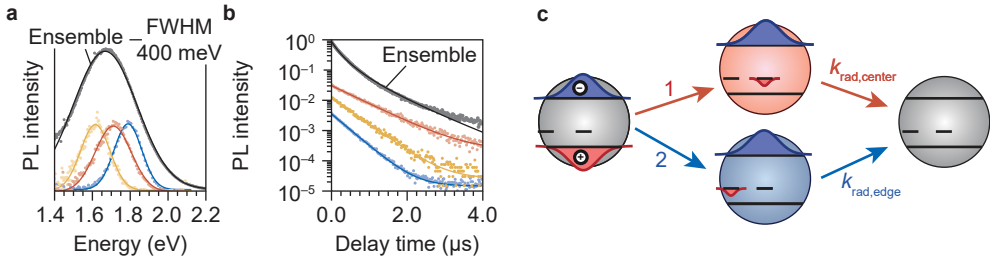

Figure 3.2 | (**a**) PL spectra of (black) an ensemble of CIS/CdS QDs dispersed in toluene, and (red, yellow, blue) single CIS/CdS QDs immobilized on a glass coverslip. Lines are fits to Gaussian peaks. (**b**) PL decay curve of (top, black) an ensemble of CIS/CdS QDs dispersed in toluene, and (red, yellow, blue) single CIS/CdS QDs. Red, yellow, and blue lines are single-exponential fits, while the black line is a fit to the model incorporating variations in the hole localization site. (**c**) Schematic depiction of hole localization at a random Cu site (which, potentially, may be any Cu^{+} ion present in the nanocrystal) after each excitation. The radiative decay rate of the excited state is determined by the electron–hole wave function overlap and thus by the location of the hole.

of spectral diffusion, the PL decay of the ON-state of these QDs is single-exponential (Figure 3.1e,f). We observe broad PL line widths for both the core-only CIS and core–shell CIS/CdS QDs (Figure 3.1g,h). From the similarity between the optical properties of these two types of QDs (see also the extended data; Ref. 77), we conclude that the intrinsic PL properties of core-only CIS are retained in core–shell CIS/CdS QDs. This is expected because the CIS core material should be unaffected by CdS shelling, as a large mismatch in ionic radii prevents Cu^{+} and Cd^{2+} interdiffusion.[76]

3.2.2 Ensemble heterogeneity

Ensemble-scale measurements on CIS and CIS/CdS QDs are strongly influenced by sample inhomogeneity. Sample inhomogeneities become particularly apparent when comparing single-QD properties to those of the ensemble. The single-QD PL line widths of core-only CIS and core–shell CIS/CdS QDs are approximately twice narrower than the ensemble line width (Figure 3.2a). The origin of sample inhomogeneity may be manifold, including polydispersity in size, shape, and composition.[48,58,61,78] In addition, as we will show and discuss in more detail below, inhomogeneous broadening is enhanced as a result of the peculiar emission mechanism of CIS QDs involving a Cu-localized hole and a dipolar excited state.

Variations in the PL lifetime between single QDs (Figure 3.2b) provide insights into the emission mechanism. Transient absorption[51,53,54,56,61] and spectro-electrochemical[63–65] studies have established that luminescence in CIS-based nanomaterials involves the radiative recombination of a delocalized electron with a localized hole. One can envision two different mechanisms of PL decay via Cu centers, which would be indistinguishable in ensemble-scale measurements, but yield different results at the single-QD level. In the first mechanism, after each excitation the hole may localize at any of the Cu^{+} ions present in the QD (Figure 3.2c).[68] Such behavior would lead to multi-exponential decay dynamics on the single-QD scale, as the localization site of the hole affects the electron–hole wavefunction overlap and thus the radiative lifetime.[45,46] Alternatively, the hole may always localize at one specific Cu site in the QD, perhaps because of the presence of a nearby defect[60] or electrostatic interactions with the

QD surface.[59] This scenario would lead to single-exponential decay of single-QD PL, as the electron–hole overlap and thereby radiative decay rate is the same after each excitation. The near-single-exponential character of single-QD PL decay curves indicate that one specific Cu site (or at most a few) is active in a QD at any given time, and that the hole does not move between Cu sites on the timescale of emission. The distribution of single-QD lifetimes is consistent with a distribution of the localization site over the QD ensemble, resulting in an ensemble-wide distribution of radiative lifetimes (Figure 3.2b; see Methods for fitting procedure).[60] However, it is important to realize that the single-QD PL decay curve would be virtually indistinguishable from single-exponential decay—especially in the case of noisy data—if a few hole localization sites were active with not so dissimilar lifetimes. Although our data does not allow us to conclude what distinguishes a "favorite" localization site from any other Cu site, we speculate that a nearby defect or surface charge could provide some charge stabilization, thereby attracting the hole. A preferential site could also be distinguished by a slight change in the local atomic arrangement: if the local structure is distorted in such a way that it more closely resembles the arrangement after hole localization, this could decrease a possible activation barrier involved in hole localization, thereby favoring localization at this specific site. Indeed, DFT calculations have shown that the presence of surface charges can determine where the hole localizes.[59]

3.2.3 Different types of spectral diffusion

Fluctuations of the PL spectrum and lifetime of single QDs, and correlations therein, reveal surprising dynamics of hole localization and their significant effect on the broadening of the ensemble properties. Our single core–shell CIS/CdS QDs are sufficiently photostable to allow for the simultaneous measurement of their PL decay curve and PL spectrum at a 100-ms temporal resolution (see also the extended data; Ref. 77).

Strikingly, some QDs show no spectral diffusion at all while featuring broad PL spectra nonetheless, with FWHM on the order of 160–170 meV. In comparison, single CdSe-based QDs generally exhibit FWHM of 50–60 meV.[79,80] Clearly, broad PL line widths in CIS-based QDs are not due to time averaging and spectral diffusion. Instead, they are intrinsic to these nanomaterials, and likely due to strong electron–phonon coupling.[81] Such broad single-particle PL spectra cannot be explained by a mechanism involving the recombination of a delocalized exciton.[49,67]

In other QDs, we observed two different types of emission fluctuations: (i) spectral diffusion wherein higher PL peak energies are correlated with shorter PL lifetimes (Figure 3.3), and (ii) spectral diffusion wherein higher PL peak energies are correlated with longer PL lifetimes (Figure 3.4). Additionally, some QDs exhibit spectral diffusion without a clear correlation between PL lifetime and PL peak energy, possibly because both types of fluctuations occur simultaneously.

Type-1 spectral diffusion with a "negative" correlation between peak energy and PL lifetime (Figure 3.3a–c; higher energies correlate with shorter lifetimes) is known from experiments on CdSe-based nanocrystals. However, the fluctuations in our CIS/CdS QDs are significantly stronger. The PL peak positions of our CIS/CdS QDs fluctuate on average over a range of 110 meV, with some QDs exhibiting fluctuations in excess of 200 meV, while CdSe-based nanocrystals show spectral diffusion over at most a few tens of meV.[79,80,82] Even more striking, type-2 spectral diffusion with a "positive" correlation between peak energy and PL lifetime (Figure 3.4a–c; higher energies correlate with longer lifetimes) is never observed for CdSe-based nanocrystals.[79,80]

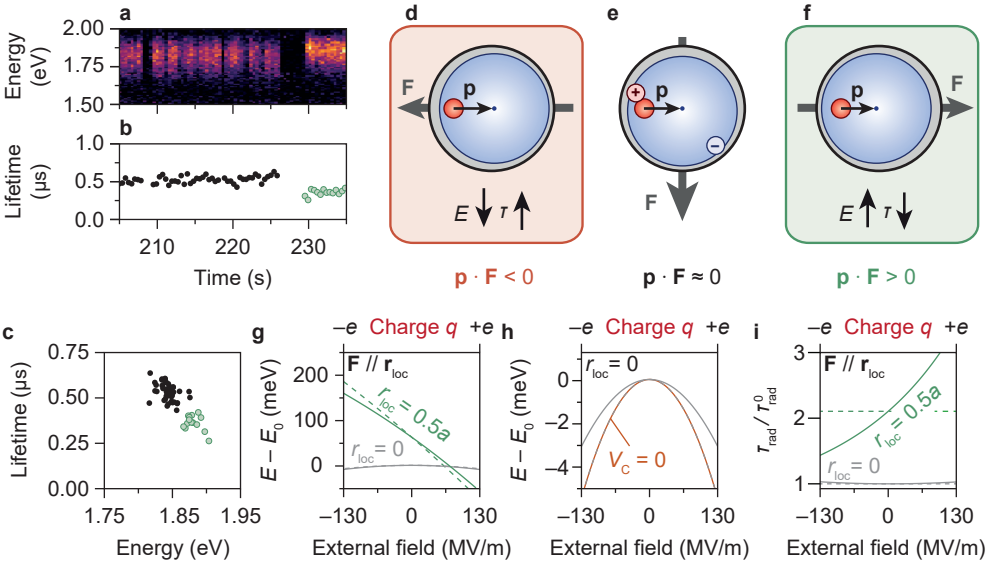

Figure 3.3 | Single-QD (**a**) PL spectra and (**b**) average lifetime, as a function of experiment time. The color scale in **a** (black to purple to yellow) indicates PL intensity. (**c**) Type-1 correlation between average lifetime and the fitted emission peak position. (**d**–**f**) Schematic depiction of spectral diffusion induced by the quantum-confined Stark effect. Mobile surface atoms or ligands create a fluctuating electric field **F**. We depict three possible orientations with respect to the excited-state dipole **p**: (**d**) antiparallel, (**e**) orthogonal, and (**f**) parallel. (**g**–**i**) Impact of the quantum-confined Stark effect, obtained from quantum-mechanical calculations. (**g**) Stark shift as a function of the external electric-field strength, with the hole localized at $\mathbf{r}_{loc} = 0$ and $0.5a$. Electric fields up to 130 MV/m correspond to a geometry that assumes a spherical CIS QD of radius $a = 1.5$ nm, with two opposite elementary charges on either side of the particle (see Figure 2.4b). (**h**) Zoom-in view of **g**, highlighting the (weak) quadratic component of the Stark shift. (**i**) Changes in the exciton radiative lifetime as a function of the external electric field. Exciton energies and lifetimes are relative to the exciton energy E_0 and lifetime τ^0_{rad} at zero external field and $\mathbf{r}_{loc} = 0$. Solid lines in (**g**–**i**) are the Stark shifts calculated using our variational approach and dashed lines are predicted by treating the external electric field as a perturbation (up to a second-order correction in energy, but to zeroth order in wave function). The orange line in h was calculated using the variational approach, but neglecting Coulomb interactions ($V_C = 0$).

3.2.4 Quantum-mechanical calculations

We will show below that both anomalies of the spectral diffusion of CIS/CdS QDs are a direct signature of the peculiar emission mechanism. Treating the quantum-confined Stark effect (QCSE) as a perturbation (see Eq. 2.12–2.13), the electric-field induced energy shift (the Stark shift; up to a second-order correction) of excited-state energy of CIS QDs can be written as

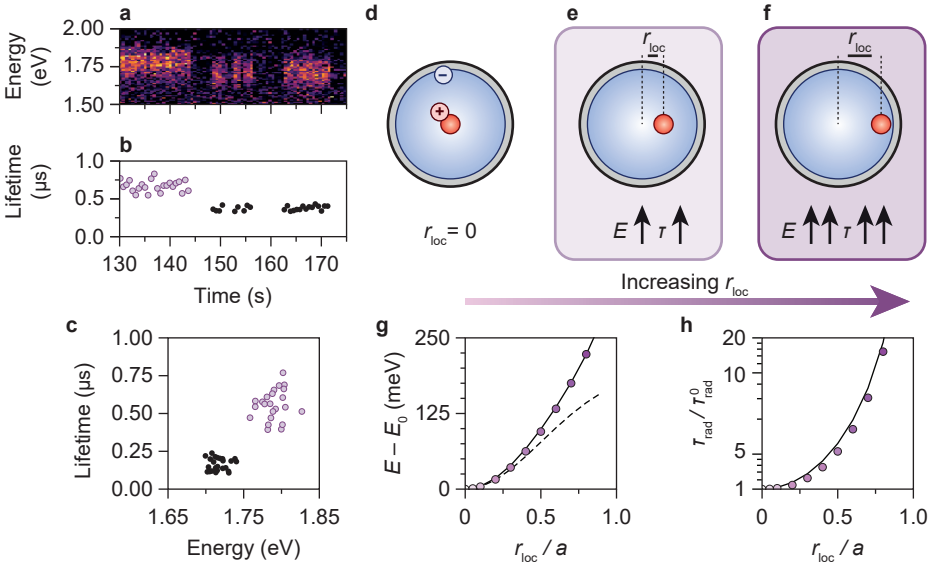

Figure 3.4 | Single-QD (**a**) PL spectra and (**b**) average lifetime, as a function of experiment time. The color scale in a (black to purple to yellow) indicates PL intensity. (**c**) Type-2 correlation between average lifetime and the fitted emission peak position. (**d–f**) Schematic depiction of spectral diffusion due to changes in the hole localization site $\mathbf{r}_{loc}$. Effects on the exciton energy E and lifetime τ are indicated in the cartoons. (**g–h**) Impact of the hole localization site, obtained from quantum-mechanical calculations. (**g**) Energy shift as a function of the hole localization site. (**h**) Changes in the exciton radiative lifetime as a function of the hole localization site. Exciton energies and lifetimes are relative to the exciton energy E_0 and lifetime τ^0_{rad} at zero external field and $\mathbf{r}_{loc} = 0$. Colored data points in **g–h** are the changes predicted by our variational approach and solid lines are predictions based on by treating the hole localization site as a perturbation (up to a second-order correction in energy, but to zeroth order in wave function). The dashed lines are correspond to a scenario where the effects of dielectric contrast are ignored ($P = 0$).

$$\Delta E = \mathbf{p} \cdot \mathbf{F} - \xi F^2, \tag{3.1}$$

where $\mathbf{p}$ is the internal static dipole moment of the excited state, and ξ the exciton polarizability. $\mathbf{F}$ is the electric field that the excited state experiences due to charges at the surface of the QD, which can be missing ligands or dangling bonds. "Conventional" spectral diffusion of CdSe-based nanocrystals is explained in terms of the QCSE,[79,80,82,83] induced by spontaneous fluctuations in $\mathbf{F}$ due to mobility of the surface charges. Experiments with applied external fields on type-I CdSe-based nanocrystals have revealed a dominant contribution of the quadratic term in the resulting change of the exciton energy E: Stark shifts due to the exciton polarizability ξ.[83,84] This effect induces a negative correlation between PL peak energy and PL lifetime, as polarization of the exciton increases the radiative lifetime (see Figure 3.3d–f).[79,80] CIS-based QDs are different from CdSe in three ways because of hole localization: (1) The electron–hole Coulomb interaction V_C depends strongly on the location $\mathbf{r}_{loc}$

of the hole, (2) **p** can be large if the hole localizes off-center, (3) Assuming a non-polarizable (localized) hole, ξ is small because of the low electron effective mass. Taking $a = 1.5$ nm, $m_e = 0.153\ m_0$ and $\varepsilon = 10$ inside the QD, the electron polarizability $\xi / 4\pi\varepsilon_0$ equals 5×10^2 Å^3 (Eq. 2.13).

We developed a simple effective-mass model (see **Chapter 2.1**), where we approximate the (core–shell) CIS QD as a spherical infinite potential well. In our model, the hole resides on specific localization sites distributed in the $CuInS_2$ core with inner radius a, while the electron is delocalized over the entire particle with radius b. We consider the possibility of spectral diffusion due to a fluctuating external electric field **F** (e.g. induced by mobile ligands/dangling bonds) that interacts with the exciton wave function (i.e., the QCSE), as well as a changing hole localization site. We approximate the hole wave function as a delta function $\delta(\mathbf{r}_h - \mathbf{r}_{loc})$ centered around $\mathbf{r}_{loc}$ and describe the electron wave function as a linear combination of particle-in-a-sphere wave functions $\psi^e_{n_e,l_e,m_e}(\mathbf{r}_e)$ (Eq. 2.3). The exciton wave function is then

$$\Psi_X(\mathbf{r}_e, \mathbf{r}_h) = \delta(\mathbf{r}_h - \mathbf{r}_{loc}) \sum_{n_e,l_e,m_e} c_{n_e,l_e,m_e} \psi^e_{n_e,l_e,m_e}(\mathbf{r}_e), \tag{3.2}$$

with coefficients $c^e_{n_e,l_e,m_e}(\mathbf{r}_e)$ obtained by minimizing the exciton energy (Eq. 2.9). The Hamiltonian,

$$H = H^e_0(\mathbf{r}_e) + V_C(\mathbf{r}_e, \mathbf{r}_{loc}) - eV_{ext}(\mathbf{r}_e) + eV_{ext}(\mathbf{r}_{loc}), \tag{3.3}$$

contains the electron-in-an-infinite-spherical-box Hamiltonian (with eigenvalues given by Eq. 2.5), and also has contributions of Coulomb interactions (direct and indirect) and the external electric field V_{ext}. The exciton lifetime τ_{rad} is inversely proportional to the square of electron–hole overlap integral:

$$\tau_{rad} = \tau^0_{rad} \left| \iint \Psi_X(\mathbf{r}_e, \mathbf{r}_h) d\mathbf{r}_e d\mathbf{r}_h \right|^{-2} = \tau^0_{rad} \left| \sum_{n_e,l_e,m_e} c_{n_e,l_e,m_e} \psi^e_{n_e,l_e,m_e}(\mathbf{r}_{loc}) \right|^{-2}. \tag{3.4}$$

Here, τ^0_{rad} is the lifetime of an exciton with the hole localized at $\mathbf{r}_{loc} = 0$, in the absence of an external electric field.

Based on our calculations (see the Methods for further details), we can understand how the qualitatively and quantitatively different spectral diffusion behavior of CIS-based QDs is a consequence of hole localization. We can attribute type-1 spectral diffusion—a negative correlation between peak energy and PL lifetime—to the QCSE due to fluctuating **F** (see schematic depiction in Figure 3.3d–f). The response of the peak energy to **F** can be much stronger than in CdSe-based QDs, because the CIS exciton can have a large internal dipole moment $\mathbf{p} = e\,\mathbf{r}_{loc}$ (where e is the elementary charge). Indeed, our effective-mass model confirms that the strength of the QCSE depends strongly on $\mathbf{r}_{loc}$ (Figure 3.3g–h). Stark shifts of several tens to hundreds of meV, as well as a manifold increase of the radiative lifetime (see Figure 3.3i), can be explained in terms of fluctuations of the external electric field (e.g. by the addition or removal of an elementary charge on the QD surface). The dipolar nature of the excited state, arising from the hole localizing at a preferential Cu^+ ion inside the QD, is thus responsible for the strong spectral diffusion in CIS/CdS QDs. The dipolar contribution to the QCSE is weak when $r_{loc} \approx 0$, or when the parallel external electric-field component is insignificant. In that case, the dominant contribution to the QCSE is the (much) weaker second-order effect—a field-induced polarization of the electron wave function—which can only account for Stark shifts on the order of a few meV.

The observation of type-1 spectral diffusion on timescales of seconds implies that **F** fluctuates on these timescales (as is common in CdSe-based QDs) while $\mathbf{r}_{loc}$ is fixed. That means, the hole must localize on the same Cu site over millions of consecutive photocycles. If it did

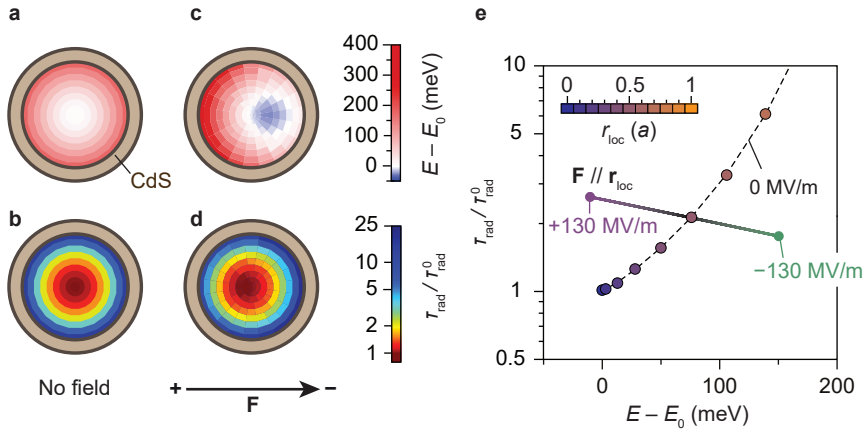

Figure 3.5 | Results from quantum-mechanical calculations depicting in color scale how the location of hole localization affects (**a**,**c**) the exciton energy and (**b**,**d**) the radiative lifetime, with (**a**,**c**) no external field and (**b**,**d**) an external field of +130 MV/m in the horizontal direction. Exciton energies and lifetimes are relative to the exciton energy E_0 and lifetime τ^0_{rad} at zero external field and $r_{loc} = 0$. (**e**) The same results as in panels (**a**–**d**), but now showing correlations between lifetime and energy. The solid purple–green line shows the relation between τ_{rad}/τ^0_{rad} and $E-E_0$ for hole localization at 0.5*a* with a varying external field from (purple) +130 MV/m to (green) −130 MV/m. The dashed line considers hole localization at increasing r_{loc}, indicated by the colored circles, without external field. The more complex relationship of τ_{rad}/τ^0_{rad} and $E-E_0$ for varying r_{loc}, with an external field of 130 MV/m, is depicted in Figure 3.6. Spectral diffusion in excess of 200 meV, observed in some QDs, is likely due to fluctuating electric fields stronger than 130 MV/m, which may occur occasionally in smaller particles.

not, the linear term in Eq. 3.1 would average out to $\langle \mathbf{p} \cdot \mathbf{F} \rangle = 0$ independent of $\mathbf{F}$. This agrees well with the single-exponential PL decay in absence of spectral diffusion (see Figure 3.2 and corresponding discussion).

While fluctuations in $\mathbf{F}$ explain type-1 spectral diffusion (see Figure 3.3a–c), they cannot explain type-2 spectral diffusion (i.e. with positive correlations between energy and lifetime; Figure 3.4a–c). Instead, type-2 spectral diffusion requires fluctuations in $\mathbf{r}_{loc}$ on the timescale of seconds (depicted schematically in Figure 3.4d–f). The dominant contribution to the energy change comes from V_C. As the hole localization site moves toward the edge of the QD, the Coulomb interaction becomes less attractive, increasing the excited-state energy (see Figure 3.4g, Figure 3.5a). Likewise, the electron–hole wave function overlap is decreased, increasing the radiative lifetime (Figure 3.4h, Figure 3.5b).

The situation is somewhat more complex if $\mathbf{r}_{loc}$ changes in the presence of an external field (Figure 3.5c,d). In most cases this produces a positive correlation of changes in energy and lifetime (Figure 3.5e) but, for some scenarios, a negative correlation can occur (Figure 3.6). However, clearly, the alternative model of a QCSE due to fluctuating $\mathbf{F}$ (purple–green curve in Figure 3.5e) cannot produce positive correlations. We thus attribute type-2 spectral diffusion

events—with a positive correlation between emission energy and PL lifetime—to a spontaneous change in $\mathbf{r}_{loc}$, the Cu site at which the hole preferentially localizes.

A change in $\mathbf{r}_{loc}$ need not involve a change in the inorganic crystalline part of the QD; DFT calculations have shown that the position at which the hole localizes can be strongly influenced by the presence of charges on the QD surface.[59] This may explain why some QDs exhibit spectral diffusion without a correlation between PL lifetime and PL peak position: (movement of) surface charges may induce both the QCSE and simultaneously a change in the hole localization site, resulting in an unclear net correlation. We observed clear type-2 spectral diffusion in only 3 of the 32 CIS/CdS QDs studied (Extended Data; Ref. 77). Together, fluctuations of $\mathbf{F}$ and $\mathbf{r}_{loc}$, possibly correlated, can produce complex and strong fluctuations of exciton energy and PL lifetime, as we observe experimentally.

3.3 | Conclusions

In summary, our single-QD experiments have shown how sample inhomogeneities determine the broad PL linewidths and multi-exponential PL decay of CIS nanomaterials. Even in absence of spectral diffusion, the PL linewidth of CIS/CdS QDs is broad (minimum FWHM > 0.16 eV). This points to electron–phonon coupling, which is, along with the long PL lifetimes, consistent with hole localization prior to radiative recombination. Additionally, the PL decay is single exponential in absence of spectral diffusion, suggesting that the hole localizes at the same Cu site after each excitation. Most QDs exhibit spectral diffusion to a much stronger extent (with shifts in excess of 200 meV) than previously observed in CdSe-based nanomaterials. We observe two types of spectral diffusion. First, spectral diffusion due to the QCSE is much stronger than in CdSe because the CIS electron–hole pair has a dipole moment. Second, changes in the hole localization site account for a spectral diffusion mechanism unique to CIS. A combination of factors, involving QD size, shape, composition, and surface-ligand coverage likely determines at which Cu site the hole preferentially localizes. In all, our results highlight how emission fluctuations provide valuable information on the photophysics of QDs. Similar experiments on InP QDs may shed light on the recent claim that trapped charge carriers are involved in the fluorescence mechanism.[85]

3.4 | Contributions

Huygen J. Jöbsis synthesized the CIS and CIS/CdS QDs and measured the ensemble-level emission spectra and decay curves. P. Tim Prins supervised Huygen J. Jöbsis and interpreted the data. Stijn O.M. Hinterding conducted the single-QD measurements, and analyzed and interpreted the data. Serena Busatto performed electron microscopy and EDS elemental analysis (see also the extended data; Ref. 77) Mark J.J. Mangnus developed the quantum-mechanical framework and performed the corresponding calculations. Daniel Vanmaekelbergh, Celso de Mello Donega and Freddy T. Rabouw supervised the project.

3.5 | Methods

Fitting of ensemble-scale PL decay

The PL decay curve of the ensemble of CIS/CdS core–shell QDs was fitted with a simple model of a distribution of radiative decay rates due to a distribution of hole localization sites. We assume that the electron wave function is the lowest-energy solution to the particle-in-a-spherical-box problem, $\psi^{e}_{100}(r) = a\sin(\pi r/a)/\pi r$ (see Eq. 2.3–2.5), and the hole is a delta function $\delta(\mathbf{r}_h - \mathbf{r}_{loc})$, with $\mathbf{r}_{loc}$ the localization site. The radiative lifetime is inversely proportional to the square of the electron–hole overlap integral (see also Eq. 3.4):

$$\tau_{rad}(r_{loc}) = \tau^0_{rad}\frac{\pi^2 r^2_{loc}}{a^2\sin^2(\pi r_{loc}/a)}, \tag{3.5}$$

where τ^0_{rad} is the radiative lifetime for $r_{loc} = 0$. We assume that the distribution of hole localization sites (over the ensemble and time) is homogeneous over a sphere of radius $r_{max} < a$ and that there is no effect of nonradiative recombination. This produces

$$I(t, A, \tau^0_{rad}, r_{max}) = \int_0^{r_{max}} \frac{e^{-t/\tau_{rad}(r_{loc})}}{\tau_{rad}(r_{loc})} 4\pi r^2_{loc}\,dr_{loc} \tag{3.6}$$

as a model for the PL decay curve. Fitting this to the data of Figure 3.2b yields a best fit with $\tau^0_{rad} = 111.2$ ns and $r_{max} = 0.735a$. This is in good agreement with the expected maximum radial position at which the hole can localize ($a_{core}/a_{core-shell} = 0.8$).

Quantum-mechanical calculations

We apply a simple effective-mass model, where the CIS/CdS core–shell quantum dot is approximated as a spherical infinite potential well with radius a of 1.5 nm. The hole resides on specific localization sites within the CIS core (with radius $b = 0.8\,a = 1.2$ nm), while the electron is delocalized over the entire nanocrystal volume. There are two factors that strongly influence the exciton energy and lifetime, namely the radial position of the hole localization site and the presence of an external electric field, which we approximate as a homogeneous field: $F = q/2\pi\varepsilon\varepsilon_0 a^2$ (see Figure 2.4b). In the scenario of two oppositely charged species on either side of the QD this implies a field of ±130 MV/m.

Calculation of matrix elements

Considering both the direct electron–hole attraction and effects due to dielectric contrast between the QD and the outer medium, the Coulomb potential V_C (see Eq. 3.3) has the form

$$V_C(\mathbf{r}_e, \mathbf{r}_h) = -\frac{e^2}{4\pi\varepsilon\varepsilon_0}\left[\frac{1}{|\mathbf{r}_e - \mathbf{r}_h|} + \frac{P(\mathbf{r}_e, \mathbf{r}_e) + P(\mathbf{r}_h, \mathbf{r}_h)}{2} - P(\mathbf{r}_e, \mathbf{r}_h)\right], \tag{3.7}$$

where the first term is the direct interaction and the other terms describe indirect interactions with image charges. The direct interaction describes the attraction between the electron and hole (drawing the electron toward the hole localization site), while the indirect contribution describes the effect that charge carriers are attracted toward the point of highest dielectric stabilization (i.e., the center of the QD).

The function $P(\mathbf{r}_1, \mathbf{r}_2)$ is given by

$$P(\mathbf{r}_1, \mathbf{r}_2) = \sum_{s=0}^{\infty} \alpha_s \frac{r^s_1 r^s_2}{a^{2s+1}} P_s(\cos\zeta), \tag{3.8}$$

with $\alpha_s = (\gamma - 1)(s + 1)/\varepsilon(\gamma s + s + 1)$, $\gamma = \varepsilon_{QD}/\varepsilon_{medium}$ and P_s is the s^{th} Legendre polynomial of the cosine of the angle ζ between $\mathbf{r}_1$ and $\mathbf{r}_2$.[16,17,60] The operator for the direct electron–hole potential can be expressed in terms of spherical harmonics using a multipole expansion:

$$\frac{1}{|\mathbf{r}_e - \mathbf{r}_h|} = \sum_{q=0}^{\infty}\sum_{p=-q}^{q} \frac{4\pi}{2q+1}\frac{\min(r_e, r_h)^q}{\max(r_e, r_h)^{q+1}} Y^p_q(\theta_e, \varphi_e)\, Y^{p*}_q(\theta_h, \varphi_h). \tag{3.9}$$

As a result, the electron–hole interaction integrals can be separated into a radial integral and an angular integral. The radial integrals are solved numerically and have the form

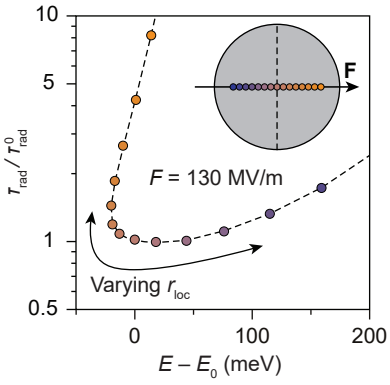

Figure 3.6 | The correlation between exciton energy and lifetime, calculated using the variational approach in the presence of an electric field of 130 MV/m. The circle colors represent the location of the hole within the CIS QD.

$$\iint_0^a R^{e}_{n_1,l_1}(r_e) R^{e}_{n_2,l_2}(r_e) \delta(r_h - r_{loc}) \frac{\min(r_e,\ r_h)^q}{\max(r_e,\ r_h)^{q+1}} re^2 dr_e = \int_0^a R^{e}_{n_1,l_1}(r_e) R^{e}_{n_2,l_2}(r_e) \frac{\min(r_e,\ r_{loc})^q}{\max(r_e,\ r_{loc})^{q+1}} re^2 dr_e. \tag{3.10}$$

The angular integrals contain the spherical harmonics and are of the form:

$$I_{l_1,m_1,l_2,m_2} = \int_0^{2\pi}\int_0^{\pi}\int_0^{2\pi}\int_0^{\pi} \sum_{q=0}^{\infty}\sum_{p=-q}^{q} \frac{4\pi}{2q+1} Y^{m_1}_{l_1}(\theta_e,\varphi_e) Y^{m_2 *}_{l_2}(\theta_e,\varphi_e) \delta(\theta_h - \theta_{loc}) \delta(\varphi_h - \varphi_{loc}) Y^{p}_{q}(\theta_e,\varphi_e) Y^{p*}_{q}(\theta_h,\varphi_h) \sin(\theta_e) d\theta_e d\varphi_e d\theta_h d\varphi_h. \tag{3.11}$$

Using the 3-*j* symbols,

$$\int_0^{2\pi}\int_0^{\pi} Y^{m_1}_{l_1}(\theta,\varphi) Y^{m_2}_{l_2}(\theta,\varphi)\ Y^{m_3}_{l_3}(\theta,\varphi) \sin(\theta) d\theta\, d\varphi = \sqrt{\frac{(2l_1+1)(2l_2+1)(2l_3+1)}{4\pi}} \begin{pmatrix} l_1 & l_2 & l_3 \\ 0 & 0 & 0 \end{pmatrix} \begin{pmatrix} l_1 & l_2 & l_3 \\ m_1 & m_2 & m_3 \end{pmatrix}, \tag{3.12}$$

and

$$Y^{m*}_{l}(\theta,\varphi) = (-1)^m\ Y^{-m}_{l}(\theta,\varphi), \tag{3.13}$$

the angular integrals can be simplified to

$$I_{l_1,m_1,l_2,m_2} = \sum_{q=0}^{\infty}\sum_{p=-q}^{q} \frac{4\pi}{2q+1} (-1)^{m_2}\ Y^{p*}_{q}(\theta_{loc},\varphi_{loc}) \sqrt{\frac{(2l_1+1)(2l_2+1)(2q+1)}{4\pi}} \begin{pmatrix} l_1 & l_2 & q \\ 0 & 0 & 0 \end{pmatrix} \begin{pmatrix} l_1 & l_2 & q \\ m_1 & -m_2 & p \end{pmatrix}. \tag{3.14}$$

Defining the hole localization site to be along the *z*-axis, combined with the relation $P_s(\cos\zeta) = \sqrt{4\pi/(2s+1)}$ $Y^0_l(\theta,\varphi)$ the contribution of indirect Coulomb interactions can be calculated using a similar mathematical procedure.

We approximated that external charges generate a homogeneous electric field F, giving rise to an electrostatic potential

$$V_{\text{ext}}(\mathbf{r}) = \mathbf{F} \cdot \mathbf{r}. \tag{3.15}$$

Variational theory

To achieve convergence in our variational approach, we used 80 basis functions, with quantum numbers n_e = {1, 2, …, 5}, l_e = {1, 2, 3} and m_e = {–3, –2, …, +2, +3}. The results of this variational approach differ slightly from the simple model predicted by perturbation theory (assuming a 1S electron wave function and an energy correction up to second order; see Fig. 3.3g–i and Fig. 3.4g–h). The most important discrepancies are that:

- Perturbation theory overestimates the exciton dipole moment (Fig. 3.3g)
- Perturbation theory overestimates the polarizability of the exciton (Fig 3.3h)

Both discrepancies originate from the fact that in our second-order perturbation description of the impact of an external field, the effect of the hole on the electron wave function is neglected: attraction of the electron wave function to the localized hole decreases the dipole moment (the electron is pulled toward the hole) of the exciton as well as the polarizability of the exciton (electron–hole attraction that opposes polarization of the electron cloud by an external field). The effective dipole moments calculated in the absence of an external electric field are in good agreement with the slopes found in Figure 3.3g. Similarly, the polarizabilities as expected from second-order perturbation theory are equivalent to what we find using variational theory without taking into account electron–hole interactions (compare orange and black dashed line in Figure 3.3h).

Chapter 4

High-throughput characterization of single-quantum-dot emission spectra and spectral diffusion by multiparticle spectroscopy

This chapter is based on:

High-throughput characterization of single-quantum-dot emission spectra and spectral diffusion by multiparticle spectroscopy. *ACS Photonics* **2023**, *10*, 2688–2698

Mangnus, M.J.J.; de Wit, J.W.; Vonk, S.J.W.; Geuchies, J.J.; Albrecht, W.; Bals, S.; Houtepen, A.J.; Rabouw, F.T.

In recent years, quantum dots (QDs) have emerged as bright, color-tunable light sources for various applications such as LEDs, lasing, and bioimaging. One important next step to advance their applicability is to reduce particle-to-particle variations of the emission properties as well as fluctuations of a single QD's emission spectrum, also known as spectral diffusion (SD). Characterizing SD is typically inefficient as it requires time-consuming measurements at the single-particle level. Here, however, we demonstrate multiparticle spectroscopy (MPS) as a high-throughput method to acquire statistically relevant information about both fluctuations at the single-particle level and variations at the level of a synthesis batch. In MPS, we simultaneously measure emission spectra of many (20–100) QDs with a high time resolution. We obtain statistics on single-particle emission line broadening for a batch of traditional CdSe-based core–shell QDs and a batch of the less toxic InP-based core–shell QDs. The CdSe-based QDs show significantly narrower homogeneous line widths, less SD, and less inhomogeneous broadening than the InP-based QDs. The time scales of SD are longer in the InP-based than in the CdSe-based QDs. Based on the distributions and correlations in single-particle properties, we discuss possible origins of line-width broadening of the two types of QDs. Our experiments pave the way to large-scale, high-throughput characterization of single-QD emission properties and will ultimately contribute to facilitating rational design of future QD structures.

4.1 | Introduction

Major advances in colloidal synthesis[86] have facilitated large-scale production of durable, color-tunable and bright quantum dots (QDs) with applications in LEDs,[87,88] lasing,[5] (bio) imaging,[89] and solar energy conversion[38,90–92]. In recent years, much effort has been directed at improving the quantum efficiency and/or color-purity of various types of QDs, including the traditional families of II–VI and III–V semiconductors, but also the more recently discovered perovskites[93] and non-toxic I–III–VI_2 QDs.[45] Narrow emission line widths and high photoluminescence quantum yields (PLQYs) are desired for many applications. Improving these key performance features requires uniform and well-defined emission properties for all QDs within a batch. However, eliminating property variations is challenging as the origins often remain obscured in ensemble measurements. Single-particle studies have revealed that the properties among single QDs can be very different, even when they originate from the same synthesis batch and are almost identical in terms of size, shape and composition.[60,77,94] In fact, emission properties are not only different from one QD to another, but are also often unstable. This manifests as blinking and spectral diffusion (SD)—temporal fluctuations in the luminescence intensity and color.[70,82,95–102] Mechanisms of blinking and SD have been identified for different types of semiconductor QDs.[70,77,82,84,97,103] Knowledge of such undesired mechanisms has facilitated steps toward rational design of superior QDs—in particular CdSe-based core–(graded) shell heterostructures.[103–106] Despite these substantial developments, extending design rules to the more promising but less well-understood class of environmentally friendly III–V QDs remains challenging. The best results have been obtained with InP/ZnSe, InP/ZnS or InP/ZnSe/ZnS core–shell(–shell) structures,[107–114] but their mechanism of luminescence is still under discussion. In particular, while a type-I band alignment is often claimed based on the bulk band energies,[108,109,111,112] delocalization of the electron[115] or hole[113] into the ZnSe shell has also been proposed. Furthermore, defect-related trapping of charge carriers may strongly impact the nature of the exciton.[85,116–118] Experimental data with simultaneous single-particle detail and statistical relevance can help resolve such debates.

Here, we use multiparticle spectroscopy (MPS) as an unbiased high-throughput technique to study variations and fluctuations of the emission properties within batches of QDs. In MPS, we simultaneously excite many (20–100) QDs and spectrally disperse the photoluminescence

from their diffraction-limited emission spots before focusing the image onto a pixel-array electron-multiplying CCD (EM-CCD) detector. Operating the EM-CCD at a frame rate of 10 Hz, we collect statistically relevant information about temporal fluctuations of single-particle emission spectra, as well as about particle-to-particle variations that occur within the batch. Compared to traditional single-particle spectroscopy, MPS facilitates a characterization speed that is at least ten times faster, and is less easily affected by the problem of a user-selection bias.[119–122] We characterize the emission from a batch of CdSe-based and a batch of InP-based core-shell QDs ($N = 491$ for CdSe/CdS/ZnS and $N = 154$ for InP/ZnSe). The batch of InP/ZnSe QDs has more heterogeneous emission properties than the CdSe/CdSe/ZnS QDs and shows more SD. The time scales associated with SD in InP/ZnSe are longer than in CdSe/CdS/ZnS QDs. We ascribe the variations and fluctuations of single-QD properties to variations in size, shape, materials properties, and to the quantum-confined Stark effect (QCSE).[82–84] Interestingly, the strong SD observed in InP/ZnSe QDs can be explained both in the framework of a delocalized exciton and an exciton with a trapped charge carrier. The introduction of MPS in the field of colloidal QDs is an important step as it facilitates unbiased high-throughput characterization of single-particle emission properties that may greatly aid the development of future generations of QDs.

4.2 | Results

4.2.1 Multiparticle spectroscopy of semiconductor quantum dots

The most common method to obtain emission spectra from individual QDs is time-consuming, making the acquisition of statistically relevant data difficult. Particles are typically measured one by one, guiding the emission of a QD through the narrow entrance slit of a spectrometer. The spectrometer contains a dispersing element such as a grating or a prism that disperses the light before it is projected onto a pixel-array camera. Calibration of the emission spectrum is relatively straightforward: all luminescence detected on the camera

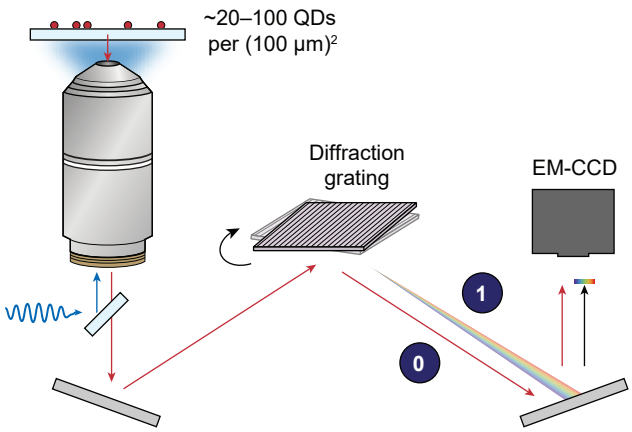

Figure 4.1 | Setup for multiparticle spectroscopy. The luminescence from 20–100 QDs is collected simultaneously by a microscope objective. The image is directed to the entrance of a spectrometer (without the use of a slit) equipped with a diffraction grating. By positioning the grating at different angles, we project either the 0th-order reflection image (0), or the 1st-order diffraction image (1) onto a pixel-array camera.

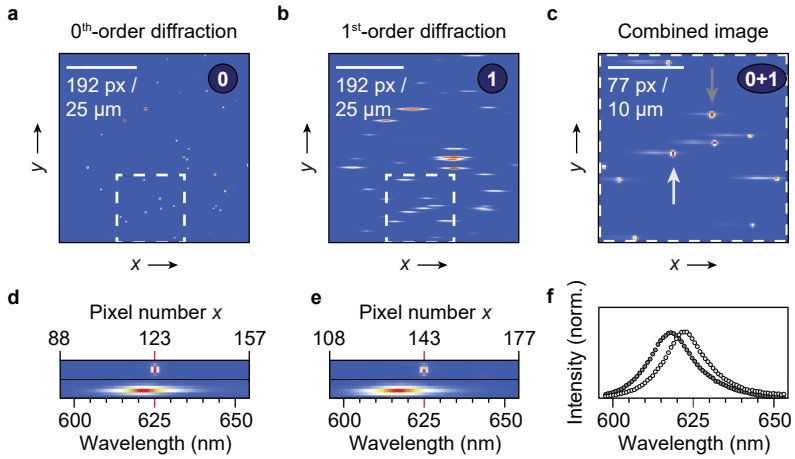

Figure 4.2 | Obtaining single-particle emission spectra. (**a**) Image of the 0th-order diffraction of a field of view containing several tens of CdSe/CdS/ZnS QDs. (**b**) The corresponding image of the dispersed 1st-order diffraction. The horizontally elongated emission spots contain spectral information. (**c**) Overlay of the 0th-order and 1st-order diffraction images. (**d**–**e**) Zoom-in views of the 0th-order and 1st-order diffraction images of the QDs highlighted in panel **c** (vertically offset for clarity). To obtain emission spectra, the wavelength axis is calibrated by fixing a center wavelength (625 nm in this experiment, approximately at the ensemble emission peak) at the pixel number *x* that corresponds to the center of the emission spot in the 0th-order diffraction image. (**f**) Resulting single-QD emission spectra of the two CdSe/CdS/ZnS QDs highlighted in panel **c**.

originates from a sharply defined position, and the light diffraction by the dispersing element is known. Measuring spectra of multiple QDs in this way usually involves scanning over the sample area, although it is possible to use a densely covered substrate and measure several QDs at different vertical positions within the slit simultaneously.[123]

Rather than measuring the photoluminescence of selected QDs one by one, we use MPS to measure emission spectra of typically 20–100 QDs simultaneously. The method is inspired by a recent study of QD blinking at the multiparticle level[124] and slitless strategies that have previously been applied in the fields of bioimaging and astrophysics.[125–127] In MPS (Figure 4.1), QDs are sparsely distributed on a glass substrate and excited by wide-field illumination. Without the use of an entrance slit, the emission from these QDs is directed to our spectrometer that is equipped with a reflective diffraction grating. Depending on the orientation of the diffraction grating in the spectrometer, either the 0th-order (i.e. the specular) reflection or the 1st-order diffraction is projected onto our pixel-array EM-CCD camera. The 0th-order reflection is just the real-space image of the field of view containing information about the position of the individual emitters (see Figure 4.2a; an example of a measurement on CdSe/CdS/ZnS core–shell QDs). In the 1st-order diffraction (Figure 4.2b), light of different colors is dispersed at different angles, with blue light diffracted at smaller angles and red light at wider angles. The image of the 1st-order diffraction thus contains the spatial information in one dimension (vertical), while the other dimension (horizontal) is a convolution of spatial

and spectral information (see Figure 4.2b). Overlaying the 0th-order and 1st-order diffraction images (Figure 4.2c), we see clearly that the emission from each individual QD is dispersed horizontally around its original position. We used a background-subtraction procedure to obtain the clean images in Figure 4.2a–c, as explained in the Methods Section (Figure 4.10, 4.11). The horizontal positions of the diffraction-limited emission spots in the 0th-order diffraction image form the basis for wavelength calibration of the numerous emission spectra in Figure 4.2b: the horizontal pixel number of the emission spot coincides with a center wavelength around which the light is dispersed (see Figure 4.2d,e). The wavelength of pixel position x_1 in the 1st-order diffraction image is calibrated as $\lambda(x_1) = \lambda_{cent} + d\lambda(x_1 - x_0^*)$, with λ_{cent} the grating's center wavelength, which depends on the grating orientation, x_0^* the pixel position of the QD in the 0th-order diffraction image, and $d\lambda = c_{(x_1 - x_0^*)} d\lambda_0$. $c_{(x_1 - x_0^*)}$ is a correction factor that accounts for a small dependence of $d\lambda$ on x (ranges from 1.01 to 0.99 for the leftmost and rightmost pixels). Using this calibration, we can reconstruct the emission spectra of many individual QDs simultaneously (Figure 4.2f). We verified that this calibration procedure of our MPS images returns a QD emission spectrum correctly, independently of the horizontal position of the QD on the sample, and confirmed that the sample does not drift on the time scale of our measurements (see Methods; Figure 4.13, 4.14).

Using MPS, we can measure the emission spectra of many single QDs with high time resolutions down to ~20–100 ms (depending on the signal-to-noise requirements), resolving the behavior of both blinking and SD. As we can simultaneously characterize 20–100 QDs, it is possible to measure hundreds of QDs within an hour—more than ten times faster than single-particle spectroscopy, and without user-selection bias. An even better level of statistical information about single-QD line widths and SD, and with better time resolution down to the ns range, can be obtained using solution-phase photon-correlation Fourier spectroscopy (sPCFS).[119,128,129] However, sPCFS does not capture SD, because each individual QDs is probed for no longer than a couple of milliseconds as they move through the detection volume.[129] Furthermore, it provides information only about average single-particle line widths and relative emission energies. sPCFS thus does not offer a complete picture of emission variations and fluctuations. Our strategy of MPS fills the gap of high-throughput characterization of absolute emission energies, variations in single-particle properties, and SD (at 10^{-2}–10^{3} s time scales) with a good level of statistics. According to previous sPCFS measurements,[129] this range of accessible time scales is exactly the interesting range in which SD occurs.

In this chapter, we first demonstrate examples of single-particle emission properties that can be extracted from high-throughput MPS measurements, before characterizing variations among particles within a batch. We finish by identifying correlations in the particle-to-particle variations and we discuss the different behaviors observed for CdSe/CdS/ZnS and InP/ZnSe QDs.

4.2.2 Spectral diffusion of single CdSe/CdS/ZnS and InP/ZnSe core–shell quantum dots

MPS at high frame rates reveals SD, i.e. fluctuations of the emission spectrum, of all QDs in the field of view simultaneously. To optimize the fluorescence signal while maintaining a high time resolution, we measured SD at a frame rate of 10 Hz for two different types of QDs: a batch of CdSe/CdS/ZnS ($N = 491$) and a batch of InP/ZnSe ($N = 154$) core–shell QDs. The CdSe/CdS/ZnS QDs are the same batch as measured in Ref. 130. The QDs are spherical, with a core diameter of 3.7 nm, and the shell consists of 8 monolayers of CdS and 2 monolayers of ZnS, so that the total QD diameter is 9.2 ± 0.8 nm (mean ± standard deviation).[130] The InP/ZnSe QDs are truncated tetrahedrons[131] with a core size of 3.2 nm and an edge length of 10.5 ± 1.2 nm (Figure 4.3a,b).

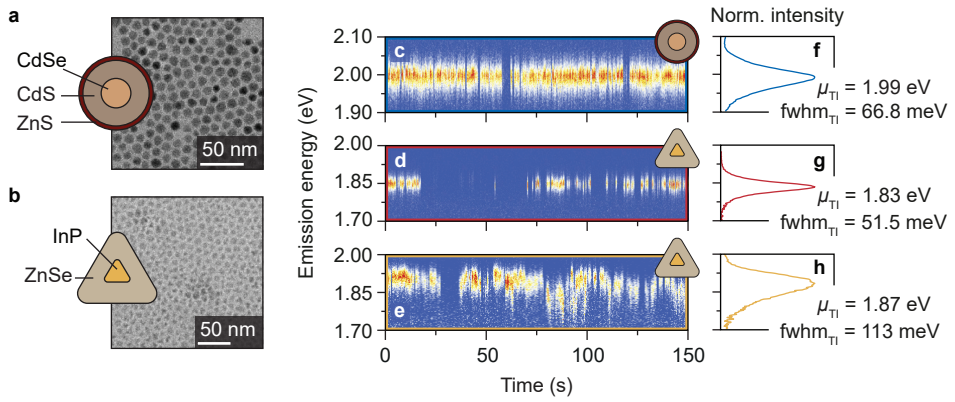

Figure 4.3 | Spectral diffusion of single QDs. (**a**–**b**) Transmission electron microscopy images of the CdSe/CdSe/ZnS core–shell QDs and InP/ZnSe QDs. Geometries of the core–shell(–shell) QDs are schematically shown in the insets. (**c**) Time trace of the emission spectra of a representative CdSe/CdS/ZnS QD with a 100-ms time resolution. The PL intensity is specified by the color and increases from blue to yellow to red. (**d**–**e**) Same as **c**, but for two InP/ZnSe QD that exhibit weak and strong spectral diffusion. (**f**–**h**) Time-integrated emission spectra corresponding to the time traces in **c**–**e**.

The CdSe/CdS/ZnS QDs show minor SD. A representative time trace of the emission spectrum is shown in Figure 4.3c. Upon close inspection, small jumps (<5 meV) of the emission peak are apparent. Two different types of behavior, observed in two different InP/ZnSe QDs from the same synthesis batch, are shown in the time traces in Figure 4.3d,e. The first InP/ZnSe QD (Figure 4.3d) exhibits SD similar to that of our CdSe/CdS/ZnS QDs, featuring only small spectral jumps. The second QD (Figure 4.3e), on the other hand, shows spectral jumps as large as 100 meV, as well as more gradual shifts. For every 100-ms spectral frame, we fitted an empirical Gaussian function to estimate the single-frame emission peak energy μ_{SF} and line width fwhm$_{SF}$. The emission peak energy μ_{SF} exhibits fluctuations because of SD, which increases the line width of the time-integrated emission spectra (Figure 4.3f–h). In the following analysis of emission energy and line width, we used an intensity threshold to reject frames during which the QD blinked off (see Methods).

More information about SD is encoded in the correlation between the emission energy and line width that a single QD features over the recorded frames. We describe the correlation in terms of the Pearson correlation coefficient $\rho_{\mu,\text{fwhm}}$: the covariance of μ_{SF} and fwhm$_{SF}$ normalized to the product of their respective standard deviations. Possible values range from –1 (perfect negative correlation) to +1 (perfect positive correlation). Figure 4.4a shows a 2D histogram of the single-frame emission energies and line widths for the CdSe/CdS/ZnS that was previously highlighted in Figure 4.3c. Higher emission energies μ_{SF} are correlated with narrower line widths fwhm$_{SF}$, with a $\rho_{\mu,\text{fwhm}}$ of –0.69. The two previously selected InP/ZnSe QDs exhibit two different types of behavior, with the first showing a weak negative correlation between μ_{SF} and fwhm$_{SF}$ and the second showing a more pronounced correlation ($\rho_{\mu,\text{fwhm}}$ of –0.19 and –0.52, respectively). 2D histograms are shown in Figure 4.4b,c. We will further discuss the observed correlations at a later point.

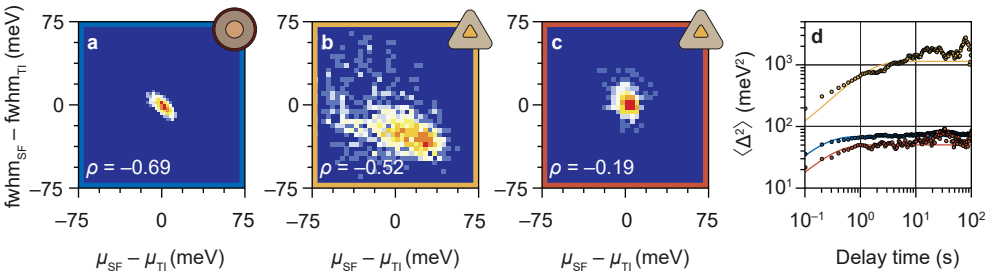

Figure 4.4 | Further characterization of single-QD spectral diffusion. (**a**–**c**) Correlation between the single-frame (100 ms) emission energy and line width, μ_{SF} and $fwhm_{SF}$. The correlations are shown as 2D histograms of μ_{SF} and $fwhm_{SF}$, relative to the time-integrated peak energy and line width, for the QDs in Fig. 4.3c–h (same colors). Note that the histograms are centered at values (just) below (0,0) as the single-frame line width is narrower than the time-integrated line width. (**d**) Mean square energy difference, $\langle\Delta^2\rangle$, of the emission energy as a function of the delay time between recorded frames. Colors correspond to the colors in Fig. 4.3c–h. Solid lines are fits to Eq. 4.1.

Based on the emission time traces (Figure 4.3c–e), SD in the CdSe/CdS/ZnS and InP/ZnSe QDs appears to occur at time scales of seconds, although it is not possible to identify SD at sub-100-ms time scales because of the time resolution. To quantify the relevant time scale at which SD occurs, we calculate the mean square energy difference between emission peaks, $\langle\Delta^2\rangle = \langle[\mu_{SF}(t) - \mu_{SF}(t+\tau)]^2\rangle_t$, as a function of delay time τ between frames (Figure 4.4d). The emission energies of a QD are correlated at short delay times, as indicated by the small $\langle\Delta^2\rangle$. For longer delay times $\langle\Delta^2\rangle$ increases because of the fluctuations in emission energy, which we observed directly in Figure 4.3c–e. $\langle\Delta^2\rangle$ reaches a plateau at delay times of several seconds, indicating that the spectrum wanders within finite bounds. The $\langle\Delta^2\rangle$-curves of the CdSe/CdS/ZnS QD and the two selected InP/ZnSe QDs (Figure 4.4d) are qualitatively similar. However, the characteristic time scales at which SD takes place are different. We determine the characteristic time scale of SD, t_c, by fitting the model function

$$\langle\Delta^2\rangle = \Delta^2_\infty\left(1 - e^{-\tau/t_c}\right) + 2\sigma^2, \tag{4.1}$$

to the experimental $\langle\Delta^2\rangle$-curve, where Δ^2_∞ is the plateau value and $2\sigma^2$ is a constant offset accounting for the fit error on the single-frame emission peak energy (see Methods). The exponential term is exactly the expected time dependence of $\langle\Delta^2\rangle$ for a single charge diffusing randomly on the surface of a spherical QD with a polarized exciton (see Methods) but may also be the result of more complex charge diffusion and a polarizable exciton. This model function provides a reasonable estimate for the magnitude and time scale of SD, but is not an equally perfect match to all experimental $\langle\Delta^2\rangle$-curves. The selected CdSe/CdS/ZnS QD of Figure 4.3c has $\Delta^2_\infty = 6.5\times10^2$ meV^2 and $t_c = 0.16$ s (blue solid line in Figure 4.4d). The two InP/ZnSe QDs yield fit parameters $\Delta^2_\infty = 4.7\times10^1$ meV^2 and $t_c = 0.26$ s and $\Delta^2_\infty = 1.1\times10^3$ meV^2 and $t_c = 1.2$ s, respectively (Figure 4.4d). Based on the values for t_c, we can conclude that for all QDs, SD probes the full range of possible emission energies μ_{SF} within a time scale of a few seconds. As indicated by the higher plateau value of the orange $\langle\Delta^2\rangle$-curve in Figure 4.4d, the range of energies over which μ_{SF} fluctuates is much larger for this InP/ZnSe QD compared to the other QDs. This is consistent with the time traces in Figure 4.3c–e.

4.2.3 Interparticle variations within batches of QDs

Our method of MPS can statistically map out single-particle fluctuations (Figure 4.3) on the one hand, and interparticle variations on the other hand. Together, they determine the emission properties of a batch of QDs. In Figure 4.5a, we show the inhomogeneous broadening of our batches of CdSe/CdS/ZnS and InP/ZnSe QDs, i.e. the distributions of time-integrated emission maxima (491 and 154 single-particle measurements, respectively). It is immediately evident that the batch of CdSe-based core–shell QDs has a more well-defined emission energy, while the batch of InP/ZnSe QDs shows wider variations. The CdSe/CdS/ZnS QDs emit at 2.004 ± 0.014 eV and the InP/ZnSe QDs at 1.86 ± 0.07 eV. The single-frame emission line width fwhm_{SF} is a measure for the homogeneous emission line width (Figure 4.5b), only affected by SD-induced broadening on sub-100-ms time scales.[129,132] For CdSe/CdS/ZnS, this single-frame line width is narrow for all particles: 61 ± 5 meV. The batch of InP/ZnSe, instead, features a broader average line width and a much wider spread: 80 ± 16 meV.

Fluctuations of the emission spectrum are observed in both types of QDs, as previously highlighted in Figure 4.3. For the batch of CdSe/CdS/ZnS QDs, a large majority of 67.3% of QDs exhibit a clear negative correlation between emission energy and line width ($-1.00 < \rho_{\mu,\text{fwhm}} < -0.25$). In other words, most single-QD spectra broaden when they shift toward the red, similar to Figure 4.4a. For the remaining QDs, a clear negative correlation may be obscured by the fit uncertainty which is large compared to the SD-induced spread of emission properties (see Figure 4.15). Most InP/ZnSe QDs (76.1%) also exhibit spectral diffusion where the emission energy and line width are negatively correlated, similar to Figure 4.4b. The other QDs shows no clear correlation, similar to Figure 4.4c. Hence, the SD in CdSe/CdS/ZnS and InP/ZnSe QDs are alike in terms of the predominantly negative correlation between μ_{SF} and fwhm_{SF}. Realize that $\rho_{\mu,\text{fwhm}}$ quantifies the degree of correlation but does not carry information about the ranges of μ_{SF} and fwhm_{SF} over which the single-QD spectrum fluctuates.

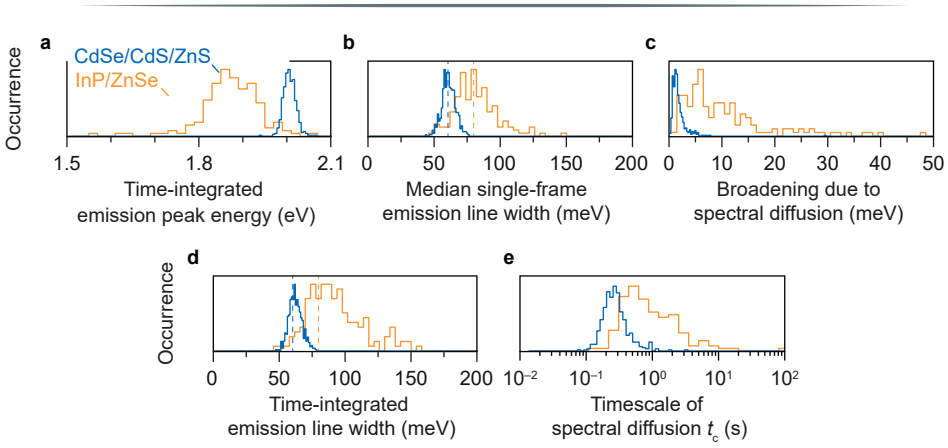

Figure 4.5 | Variations in single-particle emission properties within batches of QDs. (**a**) Distribution of the time-integrated emission energy, (**b**) single-frame emission line width, and (**c**) spectral diffusion-induced broadening. (**d**) As a result of spectral diffusion, the time-integrated emission line width is broadened with respect to the single-frame line width. (**e**) Histograms of the relevant time scales associated with SD. Results are shown for 491 CdSe/CdS/ZnS and 154 InP/ZnSe QDs (blue and yellow histograms, respectively).

We define the SD-induced broadening of the emission spectrum as the difference between the time-integrated and the median single-frame line width. Histograms of this SD-induced broadening and the resulting time-integrated emission line widths are shown in Figure 4.5c,d. The CdSe-based QDs show minor SD, with a broadening of only 1.5 ± 0.8 meV and thus the time-integrated line width (62 ± 5 meV) is almost identical to the single-frame line width (61 ± 5 meV). The batch of InP-based QDs, on the other hand, features QDs with strong SD. The SD-induced broadening of 10 ± 7 meV (mean ± standard deviation) is a substantial contribution to the time-integrated emission spectra that have a line width of 92 ± 25 meV, compared to 80 ± 16 meV for the single-frame line width. We note that our batch of InP/ZnSe QDs is highly heterogeneous: while some QDs are strongly affected by SD and feature emission line widths as broad as 120–150 meV, others are only mildly affected by SD and have emission spectra as narrow as 50–60 meV—comparable or even superior to the Cd-based QDs. Figure 4.5e shows the distribution of relevant time scales associated with SD in the two batches of CdSe/CdS/ZnS and InP/ZnSe. The characteristic time scale of SD t_c (Eq. 4.1) in the CdSe/CdS/ZnS QDs is rather uniform, with values of 0.22 ± 0.08 s (mean ± standard deviation). In our InP/ZnSe t_c is 0.9 ± 0.9 s, which is four times longer on average and more widely distributed.

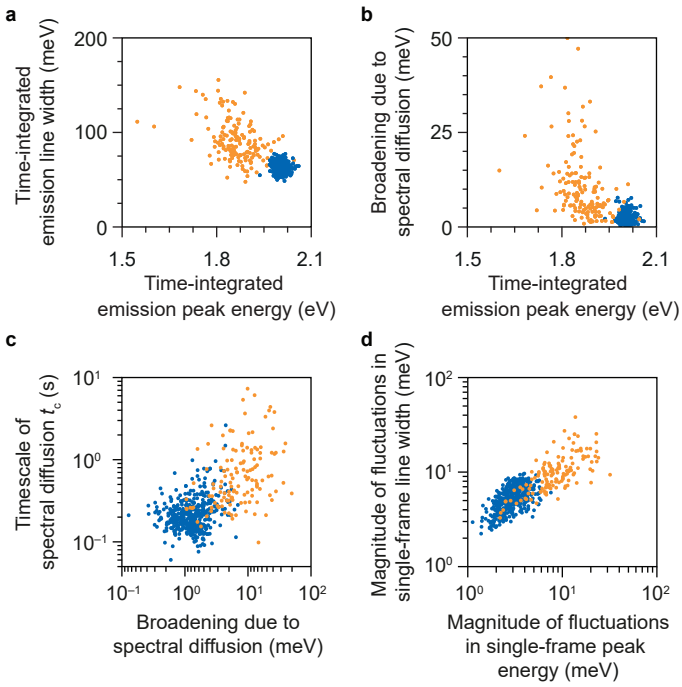

Figure 4.6 | Correlations in single-particle emission properties. Each data point in panel **a**–**d** represents an individual QD. Results for CdSe/CdS/ZnS (blue) and InP/ZnSe (yellow) are shown in the same plots. (**a**) Correlation between the emission peak energy and line width. (**b**) Relationship between the SD-induced line broadening and the emission energy of the QDs. (**c**) Correlation between the time scale of SD and broadening due to SD. (**d**) Magnitude of single-particle fluctuations in emission peak energy μ_{SF} and line width fwhm_{SF}.

Based on the distributions of emission properties we can conclude that the batch of CdSe/CdS/ZnS is a superior batch of QDs, with little inhomogeneous broadening (Figure 4.5a), and a narrow (Figure 4.5b) and stable (Figure 4.5c) single-particle emission line width. Instead, the batch of InP/ZnSe QDs is highly diverse, containing some high-quality QDs with narrow emission line widths (Figure 4.5d), but also containing a large fraction of QDs that is severely affected by SD (Figure 4.5c). We speculate that the large variations in emission properties among particles in our batch of InP/ZnSe QDs may be a consequence of variations in size, geometry, composition[115], and defects[85,116–118]. This discussion will be resumed later. At this point, we emphasize that the heterogeneity of emission properties observed in this batch highlights the unique capabilities of MPS to characterize particle-to-particle variations of the emission properties with strong statistics and without a user-selection bias.

Having characterized the variations between particles within the two batches of QDs, we will now explore possible correlations in the emission properties. We did not observe clear trends related to the brightness of the QDs, which suggests that SD cannot be linked to large variations in the PLQY, and hence will not address intensity-based correlations in the following discussion. Figure 4.6a shows the relation between the emission peak energy and the broadening due to SD. Interparticle variations are uncorrelated for CdSe/CdS/ZnS QDs. For InP/ZnSe QDs, instead, lower emission energies appear to be associated with broader line widths. Figure 4.6b shows the possible correlation between the emission peak energy and the broadening due to SD. There is no clear correlation for the CdSe/CdS/ZnS QDs, while for the InP/ZnSe QDs stronger SD-induced broadening appears to be correlated with lower emission energies. Figure 4.6c shows a positive correlation between the timescale of SD t_c and the SD-induced emission line broadening.

Figure 4.6d highlights the magnitude of the fluctuations in emission energies and line widths due to SD. Large fluctuations of μ_{SF} are in general associated with concomitant large fluctuations in $fwhm_{SF}$. Both μ_{SF} and $fwhm_{SF}$ fluctuate by up to 30 meV for InP/ZnSe versus approximately 2–6 meV for CdSe/CdS/ZnS. The magnitude of the fluctuations is unrelated to the correlation coefficient but is, on average, very different between the two types of QDs.

4.3 | Discussion

We can explain the SD of both batches of QDs (Figure 4.5, 4.6) in terms of the commonly invoked QCSE.[77,82–84] The QCSE is the energy shift of the exciton state due to polarization by an electric field. A fluctuating electric field, and hence fluctuating exciton energy, is thought to originate from the random movement of mobile charges.[133] These charges may be charged ligands hopping from site to site, or charge carriers hopping between trap states on the surface or inside the QD. If such hopping occurs on time scales of milliseconds to seconds, it manifests as SD. The quantitative effect, i.e. the magnitude of emission shift, depends on the charge distribution in the excited state of the QDs and on the position and charge of species on the QD surface. In the following discussion, we shall take into account the nature of the excited states in our CdSe/CdS/ZnS and InP/ZnSe QDs to explain the differences in their interparticle variations and fluctuations.

Mobile charges at the QD surface cause an electric field across the QD and polarize the exciton wavefunction, which not only lowers the emission energy (i.e. QCSE) but also broadens the spectrum because of enhanced coupling of the polarized exciton to optical phonons.[82–84] This twofold effect of wavefunction polarization causes the negative correlation between emission energy and line width, which has been reported before for CdSe-based core–shell structures.[79,82] Our experimental results reproduce this clear negative correlation for the majority of the CdSe/CdS/ZnS (Figure 4.4a) and InP/ZnSe QDs (Figure 4.4b). The correlation is less

clear for a subset of the QDs but, as discussed above, this may be a result of fit uncertainties that are large compared to the observed SD-induced spread of μ_{SF} and fwhm_{SF} (Figure 4.15).

The CdSe/CdSe/ZnS QDs show a minor SD-induced broadening of 1.5 ± 0.8 meV (Figure 4.5c), seemingly uncorrelated to the emission energy (Figure 4.6b). This corresponds with fluctuations of the exciton energy of 3.2 ± 1.0 meV (Figure 4.6d; convolution with the single-frame line width produces the 1.5 ± 0.8 meV broadening; see Figure 4.15). The model of the QCSE predicts that the exciton energy red shifts by an amount ΔE because of an instantaneous electric field **F** due to mobile surface charges.[77,83,84] The first (linear) term of Eq. 3.1 describes the interaction of the external electric field with a static dipole moment of the excited state **p**, which may be absent ($p = 0$) but can arise due to asymmetric (de)localization of the charge carriers. The second term is the effect of the polarizability ξ of the exciton wavefunction. High-resolution scanning transmission electron microscopy and energy dispersive X-ray (EDX) mapping show that our CdSe/CdS/ZnS QDs may have slight off-center positions of the CdSe core (Figure 4.9). As the electron delocalizes over the CdS shell while the hole is confined to the core, an asymmetric shell could produce a small dipole moment **p**. However, previous experiments with intentional external electric fields have shown that the quadratic term in Eq. 3.1 is the dominant contribution to the QCSE in spherical CdSe-based nanocrystals.[83,84]

The magnitude of the energy fluctuations depends on the maximum electric field that the exciton may experience due to the fluctuating charges on the QD surface. As a back-of-the-envelope calculation, we consider the maximum electric field $\mathbf{F}_{max}$ in the center of a spherical QD of radius a due to two elementary charges at opposite side of the surface:[77,83,84]

$$F_{\max} \approx \frac{e}{2\pi\varepsilon\varepsilon_0 a^2}, \tag{4.2}$$

where e is the elementary charge, ε_0 is the vacuum permittivity, and ε is the relative permittivity of the QD material. The QCSE is consistent with the estimated polarizability of the exciton in our CdSe/CdS/ZnS QDs, which, to first order, is the sum of electron and hole contributions (Eq. 2.13).[77,84] The contributions of the electron and hole to the exciton polarizability are $\xi_e/4\pi\varepsilon_0 = 2\times10^4$ Å^3 and $\xi_h/4\pi\varepsilon_0 = 8\times10^3$ Å^3, as estimated assuming an electron with $m_e = 0.11\,m_0$ delocalized into the CdS shell and a core-confined hole with $m_h = 1.14\,m_0$.[18,19]

Fluctuating electric fields on the order of 20 MV m^{-1} (Eq. 4.2) would hence explain emission-energy fluctuations of 3.2 ± 1.0 meV. The low polarizability and a small off-center position of the CdSe core can thus explain the minor impact of SD on our CdSe/CdS/ZnS QDs (Figure 4.7a,b). As a side note: as ξ scales with the fourth power of a_e and a_h (Eq. 2.14) and F scales with the inverse second power of the QD size, the quadratic energy term of the QCSE ($\xi F^2/2$ in Eq. 2.14) depends hardly on QD size.

The clear negative correlation between fluctuations in μ_{SF} and fwhm_{SF}, which we (Figure 4.4a) and others[79,82] have observed in many single CdSe-based QDs, is not obvious for interparticle variations within the batch of CdSe/CdS/ZnS ($\rho_{\mu,\mathrm{fwhm}}$ of –0.08; Figure 4.6a). We conclude that fluctuations at the single-particle level and interparticle variations must have different underlying causes. Whereas the correlated fluctuations in emission energy and line width are consistent with the QCSE, the uncorrelated variations at the ensemble level are likely simply due to (slight) variations in size and/or shape/geometry of the QDs (Figure 4.9), while differences in wavefunction polarization play no significant role.

The fluctuations of InP/ZnSe QDs are also consistent with the QCSE. However, the emission properties of our InP/ZnSe QDs are clearly more broadly distributed (Figure 4.5a) and fluctuate more (Figure 4.5b,c) than those of the CdSe/CdS/ZnS QDs. This wider inhomogeneous

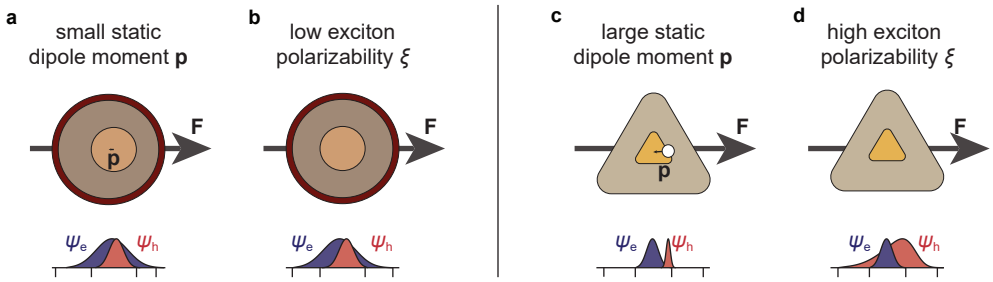

Figure 4.7 | Linear and quadratic contributions to spectral diffusion. (**a**) CdSe/CdS/ZnS core–shell–shell QDs are nominally spherically symmetric but a small offset of the core may result in a small intrinsic dipole moment of the excited state **p**. (**b**) Exciton polarizability in CdSe/CdS/ZnS QD is low because the electron effective mass is low and the hole's delocalization volume is small. (**c**) The proposal of hole localization at defect sites in InP-based QDs[85,117,118] comes with a static dipole moment **p** in the excited state. Depending on the position of this defect site, the interaction with external electric fields may be strong. (**d**) The proposal of the hole delocalization into the shell implies a large polarizability of the exciton, as the effective mass of the hole is large. This would make the exciton energy strongly dependent on fluctuating electric fields.

broadening of InP-based confirms previous studies, which found similar trends.[114,119] To understand why the InP/ZnSe QDs are so different quantitatively, we consider two types of proposals for the nature of the excited state in InP/ZnSe.

Shallow electron or hole traps in InP-based QDs have been proposed, such as Zn on an In site in the core or In on a Zn shell in the shell,[85,116–118] from which radiative recombination could occur. Carrier localization should be associated with large lattice reorganizations and thus a red shift and line broadening of the emission.[77,85,117,118] The proposal of carrier localization also implies reduced electron–hole wave function overlap, which is consistent with previous observations that exciton lifetimes are longer at the low-energy side of the emission spectrum.[134,135] The degree of carrier localization may vary depending on the interdiffusion of core and shell materials, which could cause the variations between QDs: deeper localization causes a stronger red shift and more broadening. Indeed, we observe that QDs emitting at lower energies typically have broader time-integrated (Figure 4.6a; correlation coefficient $\rho_{\mu,\mathrm{fwhm}} = -0.48$) as well as single-frame line widths (Figure 4.17). Localization of a charge carrier at defect sites can also result in a significant static dipole moment **p** in the excited state. This would interact strongly with fluctuating external electric fields through the linear term in Eq. 2.13,[84] as has previously been observed for $CuInS_2$ QDs.[60,77] For example, if the hole is trapped 1 nm off-center while the electron occupies the entire InP core, this creates a dipole moment with magnitude $p = 1.6 \times 10^{-28}$ C m. In the presence of an external field of 20 MV m^{-1} of an InP/ZnSe QD, the emission energy may change by as much as 20 meV. This is consistent with the observed fluctuations of the emission maximum of 11 ± 7 meV due to SD (Figure 4.6d and Figure 4.15).

An opposite picture of the excited state of InP/ZnSe QDs has also been proposed, in which the hole delocalizes into the ZnSe shell and the electron remains core-confined.[113] While InP/ZnSe would be a type-I QD according to the bulk band alignments, a charge disbalance at

the core–shell interface could change the band offsets and cause hole delocalization.[115] Full delocalization of the hole would increase its polarizability ξ_h 100-fold according to Eq. 2.13, going from a_h = 1.5 nm for a core-localized hole to a_h = 4 nm for a delocalized hole. As the hole in InP is relatively heavy ($m_h = 0.6\, m_0$; Ref. 111), the overall exciton polarizability of our InP/ZnSe QDs would be as high as $\xi/4\pi\varepsilon_0 = 3\times10^5$ Å^3. The tenfold higher exciton polarizability in InP-base QDs compared to CdSe-based QDs may thus be responsible for the strong SD observed in (some of) the InP/ZnSe QDs. The interparticle variations in emission energy and line width could be due to differences in the charge disbalance at the core–shell interface, which would cause differences in delocalization and hence differences in polarizability. In this picture, correlations between emission energy and line broadening emission (Figure 4.6a,b) could also be due to the degree of (de)localization.

The two possible options for the nature of the excited state in CdSe/CdS/ZnS and InP/ZnSe are illustrated in Figure 4.7. Ironically, both a localized and a delocalized hole can explain the strong SD that we observe for our InP/ZnSe QDs. In the case of a localized hole, the static dipole moment **p** of the excited state increases the influence of the QCSE through the linear term in Eq. 2.13. In the case of a delocalized hole, the exciton polarizability ξ is high and the influence of the QCSE is strong through the quadratic term in Eq. 2.13. Interparticle variations in the degree of (de)localization may well explain the strong inhomogeneous broadening that we and others[85,114,119,136] have observed for InP/ZnSe QDs.

The different characteristic time scales of SD, as observed in Figure 4.6c may be explained in terms of the different geometries of the CdSe/CdS/ZnS and InP/ZnSe QDs. Specifically, the spherical geometry of the Cd-based core–shell–shell QDs implies that the energy shift of the exciton depends only on the magnitude of the fluctuating charge disbalance on the QD surface, irrespectively of where this charge disbalance occurs. The InP/ZnSe truncated tetrahedra lack this spherical symmetry so different possible locations of mobile charge on the surface are inequivalent. For example, the exciton would be affected less by a surface charge disbalance at the apices of the tetrahedron than by one at the sides. The longer time scale of SD in InP/ZnSe may be a consequence of this lower symmetry: mobile surface charges need to move over a larger area of inequivalent positions on the QD surface before all possible emission energies are sampled. An alternative explanation may be that the nature of the mobile charges is different. Their mobilities may depend on the surface chemistry of the QD.

Further experiments are required to get a complete picture of SD and its underlying chemophysical dynamics. Regarding our CdSe/CdS/ZnS and InP/ZnSe QDs, characterizing SD while externally controlling the static electric fields across the QDs[83,84] may distinguish between contributions of a static dipole moment (producing a linear field dependence; Eq. 2.13) and/or strong polarizability of the exciton wave function (quadratic field dependence; Eq. 2.13). Information from single-particle lifetimes and excitation spectra may further help settle this debate. The relevant time scales associated with SD—on the order of seconds—may be related to binding and dissociation of ligands on the surface. Such processes typically have an activation energy that could be extracted from temperature-dependent experiments or a systematic study with different types of capping ligands. To design future QDs with reduced SD, anchoring ligands in a rigid inorganic shell[137] could be a promising strategy.

4.4 | Conclusions

In summary, we have introduced MPS as a high-throughput method to measure individual emission spectra of 20–100 single emitters simultaneously at relevant time scales ranging from tens of milliseconds to several minutes. MPS provides statistically relevant information about variations and fluctuations in absolute emission spectra. The results are not affected by

an undesired user-selection bias that is inherent to single-particle spectroscopy. Using MPS, we characterized the variations of the emission properties in a batch of CdSe/CdS/ZnS and InP/ZnSe QDs. We find that the CdSe/CdS/ZnS QDs have a well-defined emission energy and a narrow line width (62 ± 5 meV). Our batch of InP/ZnSe is much more diverse, with a wide distribution of emission energies and featuring both wide and narrow line widths (92 ± 25 meV). Whereas the line width of our CdSe/CdS/ZnS QDs is hardly affected by SD (broadening of 1.5 ± 0.8 meV), SD can play a substantial role for InP/ZnSe QDs (10 ± 7 meV). For most QDs, SD exhibits a negatively correlated behavior between single-frame emission energy and line width, which we ascribe to the QCSE. Differences in homogeneous broadening and SD between the two types of QDs are likely related to differences in charge distribution/localization in the excited state or differences in crystallite symmetry. Our data and discussion may help in the further understanding of the excited states of InP-based QDs, which is not yet as mature as for CdSe-based QDs. Various variations and extensions of the MPS method are possible, such as cryogenic measurements on the simultaneous diffusion of dark and bright exciton, trion, and/or biexciton emission lines,[72] or polarization-resolved measurements to correlate emission properties with nanocrystal anisotropy.[138] MPS could further allow for statistically significant studies of the influence of external parameters on single-QD emission, such as ligand coverage, humidity, or gas environment, which are otherwise very challenging. It may thus serve as a versatile high-throughput technique to evaluate single-QD properties as and contribute to the development of future generations of QDs with tailored emission properties.

4.5 | Contributions

Jur W. de Wit and Jaco J. Geuchies synthesized the InP/ZnSe and CdSe/CdS/ZnS QDs. Electron microscopy experiments at EMAT were supported by the European Commission (EUSMI grant E210100474) and were performed by Jaco J. Geuchies and Wiebke Albrecht. Mark J.J. Mangnus performed multiparticle spectroscopy experiments, and analyzed the data. Mark J.J. Mangnus, Jur W. de Wit, Sander J.W. Vonk, Jaco J. Geuchies, Arjan J. Houtepen and Freddy T. Rabouw discussed and interpreted the data. Freddy T. Rabouw supervised the project.

4.6 | Methods

Synthesis of CdSe/CdS/ZnS core–shell–shell QDs

The batch of CdSe/CdS/ZnS core–shell—shell QDs was the same as in Ref. 130. The synthesis procedure is described in Ref. 130.

Synthesis of InP/ZnSe QDs

Nanocrystals were synthesized using a modified method based on Tessier et al.[136] Briefly, a mixture of 100 mg indium(III) chloride, 300 mg zinc(II) chloride in 5.0 mL oleylamine was degassed at 120 °C for 1 hour and then heated to 180 °C under nitrogen atmosphere. 0.46 mL of tris-(diethylamino)phosphine was rapidly injected once the mixture reached the temperature of 180 °C. The formation of InP cores proceeded for 20 minutes, after which 1.08 mL of stoichiometric TOP-Se (1.87 M) was injected dropwise over the course of 10 minutes At 140 minutes, 4 g of zinc stearate dissolved in 4 mL oleylamine and 16 mL ODE (both previously degassed) was injected in the reaction mixture. When the temperature reached 180 °C again, 3.36 mL TOP-Se (1.87 M) was injected dropwise while increasing the temperature to 320 °C. After 240 minutes the reaction was stopped removing the heat source and cooling with pressurized air. The InP/ZnSe NCs were precipitated by adding 1 eq. volume ethanol and centrifuging at 2750 rpm for 5 minutes. The precipitate containing the NCs was collected and redispersed in toluene. The washing step with ethanol was repeated twice.

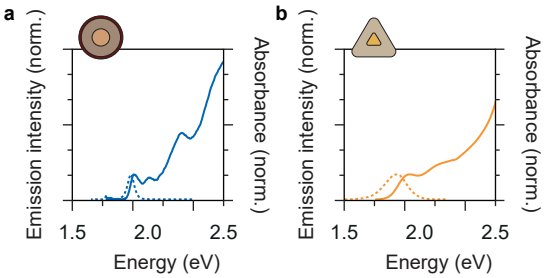

Figure 4.8 | Ensemble absorption and emission spectra. (**a**) Ensemble absorption (solid line) and emission spectrum (dashed line) of the CdSe/CdS/ZnS QDs. (**b**) Same, but for the InP/ZnSe QDs. The emission spectra have a fwhm of 70.7 meV (CdSe/CdS/ZnS) and 224 meV (InP/ZnSe). Emission spectra were recorded for a layer of QDs excited at 445 nm (CW) under the same conditions as we used for multiparticle spectroscopy experiments.

Sample preparation for multiparticle spectroscopy

In MPS, eliminating background luminescence is possibly even more important than in "regular" single-particle spectroscopy, as we use wide-field excitation scheme that may excite fluorescent organic residues and/or impurities in/on the glass coverslip as well as QDs. In the absence of an emission slit, this background light strikes the diffraction grating and subsequently the detector, causing a broad background profile that complicates the identification of single-particle emission spectra. Samples for MPS were prepared by drop-casting 40 μL of QD solution (diluted from the crude QD solution by a factor 10^5–10^7 in spectrophotometric-grade toluene; InP/ZnSe QDs were diluted in a 1 v% solution of ethyl thioglycolate/toluene) onto glass #1.5 coverslips. After letting the solvent evaporate, the samples were sealed in an inert nitrogen atmosphere. An ideal QD coverage on the glass substrate is around 20–100 particles per (100 μm)^2. To minimize background luminescence, the glass coverslips were cleaned prior to drop-casting the QD solutions, using a low-pressure plasma cleaner (Diener Zepto), operated at 0.2–0.4 mbar, at the maximum power setting.

Multiparticle spectroscopy

MPS experiments were performed on a homebuilt microscopy setup centered around an inverted microscopy body (Nikon Ti-U) that held the sample. Samples were excited in a wide-field setup using a 445-nm fiber-coupled laser (Coherent OBIS LX, 45 mW), operated at full power in CW mode. The laser light was attenuated using ND filters and focused onto the back-focal plane of an oil-immersion objective (Nikon CFI Plan Apochromat Lambda 100×, NA 1.45), using a dichroic long-pass mirror. A laser beam expander was used, so that the excitation spot on the sample surface was approximately Gaussian with a full width at half maximum (fwhm) of 60 μm. To optimize the luminescence signal while limiting possible effects of photodegradation, we used mild CW excitation powers of 20–80 W/cm^2.

Luminescence was collected using the same objective and was filtered using a 550 nm long-pass and 700 nm short-pass filter for the measurements on CdSe/CdS/ZnS and a 500 nm long-pass and 900 nm short-pass filter for the measurements on InP/ZnSe (Thorlabs FELH550/FESH700 and FELH500/FESH900). The emission light was then directed at the entrance of a spectrometer (Andor Kymera 193i) equipped with a reflective diffraction grating (150 lines/mm, blazed at 500 nm). The diffraction grating and mirrors inside the spectrometer were positioned so that either the 0th-order or 1st-order diffraction image of the grating was directed at an electron-multiplying CCD-camera (Andor iXon Ultra 888). For our measurements on InP/ZnSe QDs, the image was cropped at the entrance of the spectrograph to select a narrow horizontal region of ~6.5 μm (50 pixels). We corrected for the wavelength-dependent detection efficiency of the setup using a broadband calibrated light source (Ocean Optics HL-3Plus-CAL).

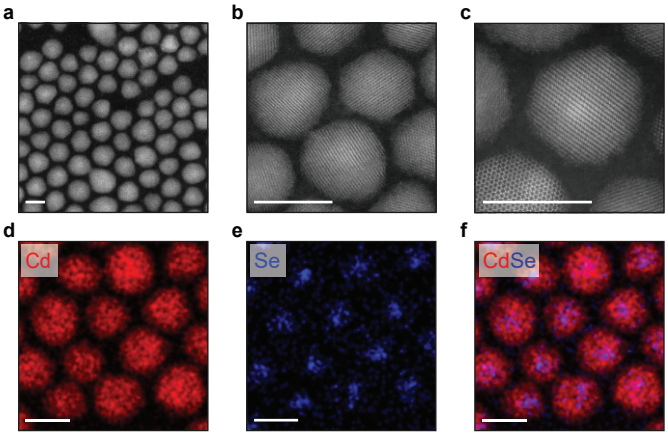

Figure 4.9 | Structural characterization of CdSe/CdS/ZnS QDs. (**a**–**c**) HAADF-STEM images of the CdSe/CdS/ZnS QDs. The CdSe core appears slightly more bright than the CdS shell. (**d**–**f**) EDX net count maps of the elements Cd (red) and Se (blue), shown separately in **d** and **e**, and overlaid in **f**. Scale bars are 10 nm.

Electron microscopy characterization

High-resolution high-angle annular dark-field scanning transmission electron microscopy (HAADF-STEM) images and EDX maps (Fig. 4.9) were acquired on a Thermo Fisher Scientific/FEI Titan microscope operated at 300 kV. HAADF-STEM images and EDX maps were acquired with a 50 pA and 150 pA current, respectively.

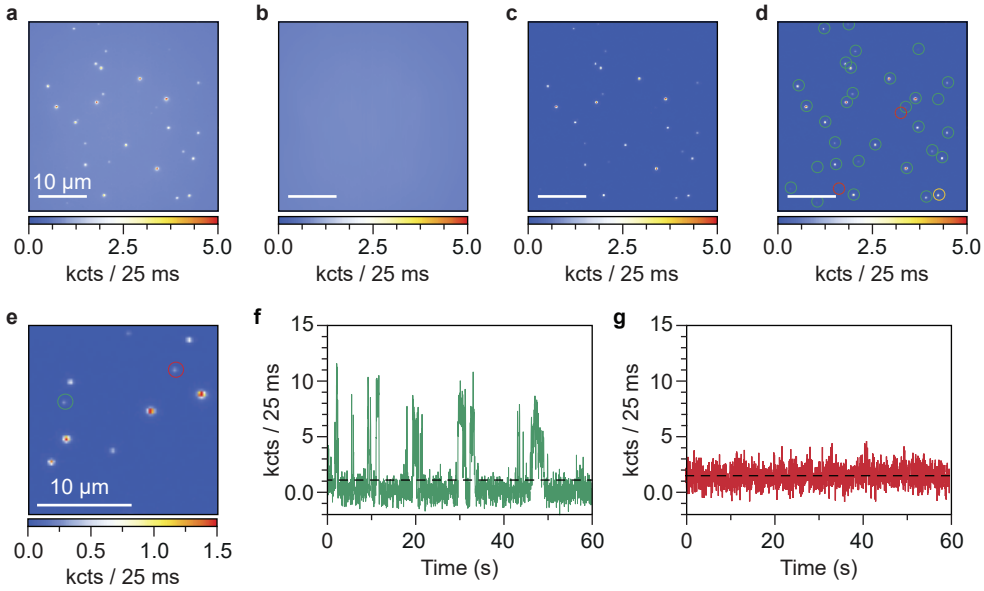

Figure 4.10 | Procedure of particle identification and background subtraction of CdSe/CdS/ZnS QDs. (**a**) Non-dispersed image of 10–100 CdSe/CdS/ZnSe quantum dots (QDs), obtained by integrating a video over 60 s. A single QD emitter appears as a bright spot. QD positions are found by identifying isolated clusters of pixels with a high measured intensity. Color scale bars represent average count rates (in kcts / 25 ms). (**b**) Map of the background intensity, calculated by taking a moving average over 25 pixel intensities in the vertical direction, excluding pixels corresponding to QD positions. (**c**) Corrected 0^{th}-order image, obtained by subtracting the background. (**d**–**e**) Identification of QD positions. An initial guess of QD positions is based on pixel intensities. Bright positions (green circles) always correspond to a QD (or a cluster of QDs), while identification of QDs on some of the ”dimmer” positions is less certain (red circles). Panel **e** is a zoom-in view of panel d. (**f**–**g**) Intensity time traces of the emission from the red and green encircled QDs in panel **e**. The intensity traces can be used to distinguish between QDs that are often in a non/weakly emissive state and positions with a relatively high background level (e.g. due to defects in glass or residual fluorescent organics). “Real” QD positions exhibit characteristic blinking, where the intensity fluctuates between a bright and dark state (e.g. the green spot in e, corresponding to the intensity trace in **f**). Intensity traces without such fluctuations are clusters, permanently dim QDs, or spots with a source of constant background intensity (e.g. the red circle in **e**, corresponding to the intensity trace in **g**). The intensity threshold used to distinguish QDs from background signal was set at 3.5 kcounts / 25 ms.

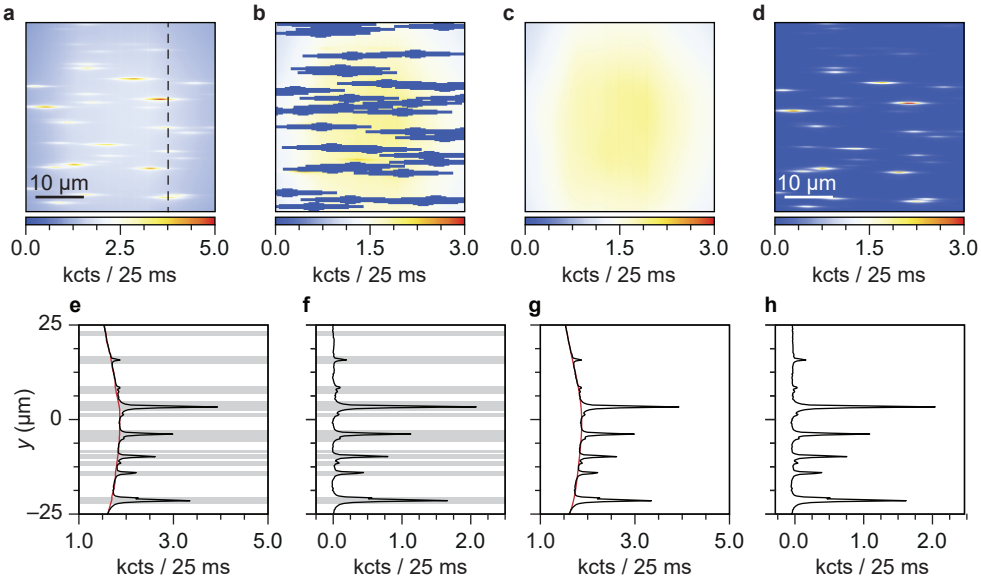

Figure 4.11 | Procedure of obtaining single-particle emission spectra of CdSe/CdS/ZnS QDs. (**a**) Spectrally dispersed image of the same field of view as in Figure 4.10a–d. Vertical positions of the emission spots remain approximately the same, while the emitted light is dispersed horizontally. Because wide-field excitation is used without a slit in the experiment, various sources of background light contribute to a complex background that may obscure some QD signal. (**b**) Same as a, but the regions around identified QD positions (see Figure 4.10d) are masked. (**c**) Map of the background intensity, calculated using a polynomial fit along each pixel column, excluding pixels that have a higher intensity as a result of spectrally dispersing QD signal (see panels **e**–**h**). (**d**) Background-corrected, spectrally dispersed image of the emission of multiple QDs. This image serves as the starting point for the analysis of single-particle emission properties. Color scale bars represent average count rates (in kcts/25 ms). (**e**) Vertical cross-cut of the data along the dashed line in **a**, with datapoints corresponding to the masked pixels in panel **b** highlighted by grey shading. These datapoints were excluded as they correspond to regions of higher intensity as a result of QD emission. From the adjusted dataset, a first guess of the background is made by taking a moving average over 25 pixel intensities along the vertical direction (red solid line). (**f**) Same as **e**, but with the guess-background subtracted. The pixels with counts below 100 are selected as pixels unaffected by emission from QDs. These correspond to the unshaded areas and are used to fit the position dependence of the background intensity. (**g**) Same as e, but with a one-dimensional 12^{th}-order polynomial fit to the background defined by the selected pixel positions shown in grey in **e**–**f**. (**h**) Background-corrected cross-section of the dispersed image, obtained by subtracting the polynomial fit to the background.

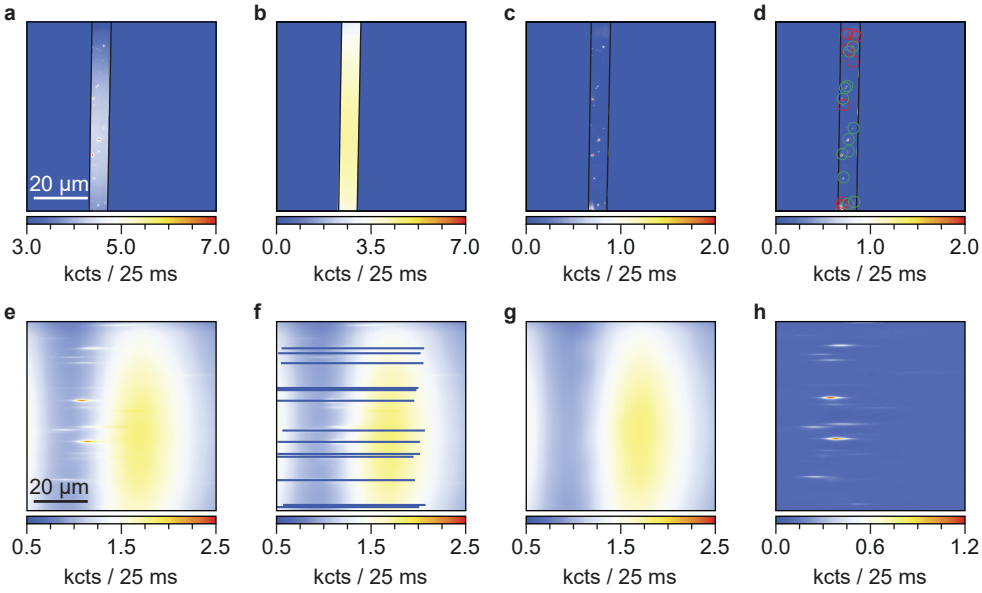

Figure 4.12 | Multiparticle spectroscopy experiments on InP/ZnSe QDs. (**a**–**d**) Same as Figure 4.10a–d, but for InP/ZnSe QDs and integrating over 150 s instead of 60 s. To simplify particle identification and to prevent overlapping of potentially broad emission spectra, the image of the field of view was cropped prior to entering the spectrometer (to a horizontal region with a width of 6.5 µm). The intensity threshold used to distinguish QDs from background signal was set at 7.5 kcounts / 200 ms.'False' QD positions are highlighted in red. (**e**–**h**) Same as Figure 4.11a–d, but using a different masked region (panel **b**) that better corresponds to the signal from the InP/ZnSe QDs. Scale bars represent average count rates (in kcts / 50 ms).

Calibration of the emission spectra obtained from multiparticle spectroscopy

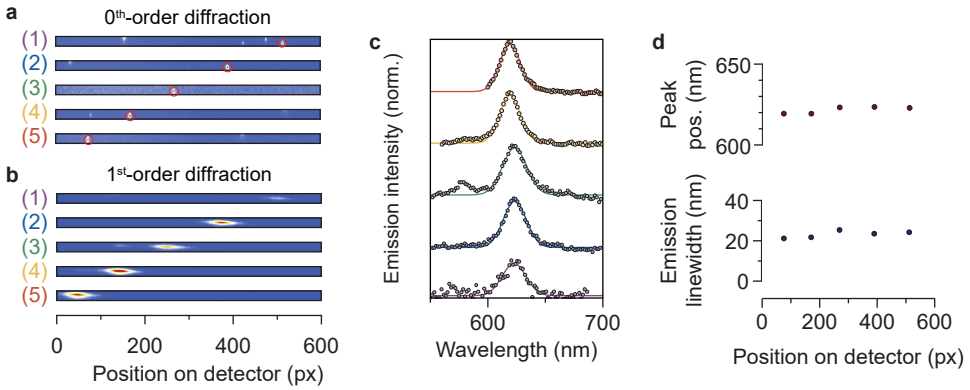

Figure 4.13 | Calibration of the emission spectra. (**a**) Emission from a single CdSe/CdS/ZnS QD, obtained by measuring the image of the 0th-order diffraction. Panels 1–5 are horizontal slices of the 0th-order diffraction image, measured after moving the QD to five different horizontal positions. (b) Corresponding horizontal slices of the 1st-order diffraction image (measured without a slit). As a result of moving the QD to five different horizontal positions, the emission spectra are centered at five different horizontal pixel positions of the detector. (**c**) Wavelength-calibrated emission spectra. (**d**) Emission peak wavelength of the QD, measured at five different horizontal positions. (**e**) Same as **d**, but for the emission line width (fwhm). Both the QD's emission wavelength and line width obtained in our multiparticle spectroscopy setup are independent of the horizontal position of the QD.

Characterization of sample drift

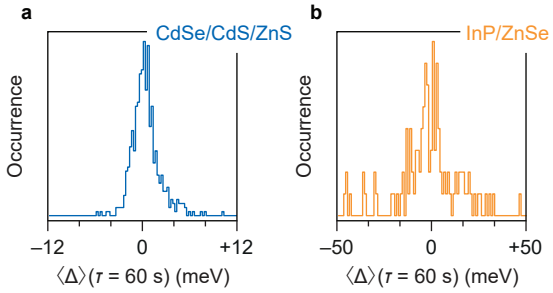

Figure 4.14 | Characterization of sample drift. (**a**) Histogram of $\langle\Delta^2\rangle(\tau = 60\,\text{s})$, for all CdSe/CdS/ZnS QDs. In our multiparticle spectroscopy experiments, sample drift should manifest itself as a systematic shift of all QD spectra (positions) to higher/lower energies (left/right). However, as the histogram of the mean energy difference is approximately symmetric around $\langle\Delta^2\rangle = 0$ meV, we conclude that there is no significant sample drift at the timescale of our measurements. (**b**) Same, but for the InP/ZnSe QDs.

Uncertainties in the correlation between single-frame emission energies and line widths

Figure 4.15 shows histograms of the spread (standard deviation) and average fit uncertainties of the emission peak energy μ_{SF} and line width $fwhm_{SF}$, for different values of $\rho_{\mu,fwhm}$. For both the CdSe/CdS/ZnS and the InP/ZnSe QDs, the SD-induced variations of the emission peak energy and line width are larger than the associated fit uncertainties. We observe that the fit uncertainties are typically larger for the QDs where we did not see a clear negative correlation between μ_{SF} and $fwhm_{SF}$.

A minor fraction (2.7%) of the CdSe/CdS/ZnS QDs displayed a weak positive emission energy–line width correlation ($+0.25 < \rho_{\mu,fwhm} < +0.50$). One QD (0.2%) exhibited a strong positive correlation with $\rho_{\mu,fwhm} > +0.50$.

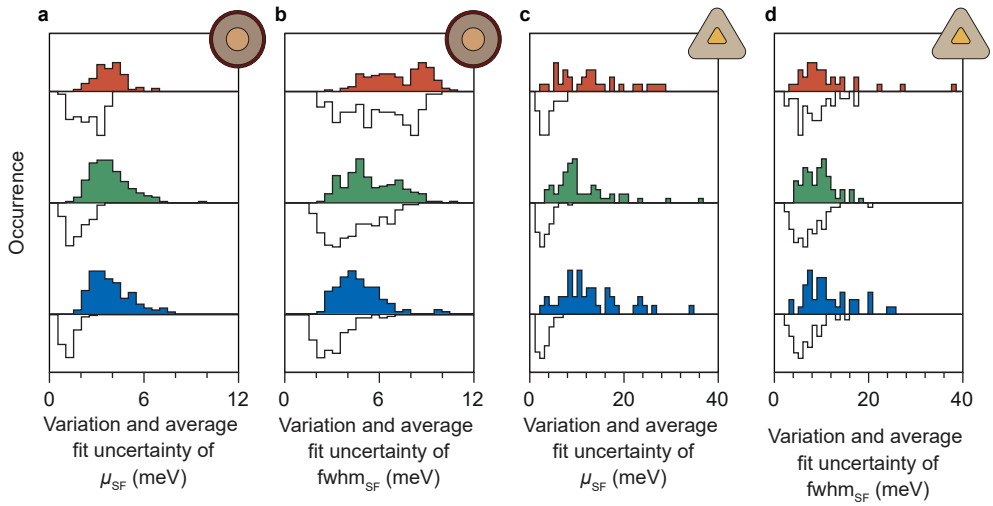

Figure 4.15 | Impact of fit uncertainties on the correlated behavior between μ_{SF} and $fwhm_{SF}$. (**a**) Histogram of the SD-induced variation (standard deviation; colored histograms) and average fit uncertainties (open histograms, upside-down) of the emission peak energy μ_{SF} for the measurements on CdSe/CdS/ZnS QDs. The different colors correspond to QDs with strongly negative, moderate negative, and unclear correlations between μ_{SF} and $fwhm_{SF}$, as indicated by the values of $\rho_{\mu,fwhm}$. (**b**) Same, but for the variation and fit uncertainty of the emission line width $fwhm_{SF}$. (c–d) Same as **a**–**b**, but for the InP/ZnSe QDs.

Upon closer inspection of these 13 QDs, we find that these positive correlations do not represent intrinsic photophysics of the QDs as they have come about due to either (1) an experimental artifact that occurs when two QDs are spaced closely together (see Figure 4.16a–b), (2) imperfect background subtraction of the emission spectrum for weakly-emitting QDs, or (3) photodegradation of the QD that leads to a gradual blue shift of the emission spectrum[95,139] (see Figure 4.16c–d). The experimental artifact occurs when two QDs are spaced closely together leading to overlap of the emission spectra in the 1st-order diffraction image (see e.g. Figure 4.6a–b). Since the wavelength calibration (see Figure 4.2d,e) is based on the position of one selected QD, overlap of two emission spectra leads to a shoulder in the emission spectrum that originates from emission of the neighboring QD, either on the red or blue side of the actual emission spectrum. At times when the selected QD emits weakly, emission signal from a blue (red) neighboring QD will lead to a Gaussian fit with a blue-shifted (red-shifted) center wavelength and a broadened emission spectrum. As a strategy to minimize the occurrence of this experimental artifact, we fitted only to the wavelength region around the relevant emission peak. As such, the actual emission spectrum of the selected QD is at most affected by a shoulder of a neighboring QD.

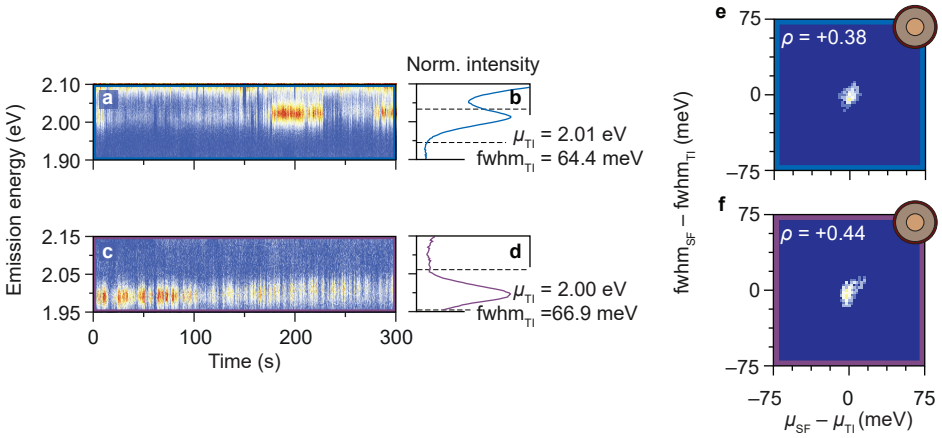

Figure 4.16 | Quantum dots exhibiting a 'false' positive correlation between μ_{SF} and fwhm$_{SF}$. (**a**) Example of a result from a multiparticle spectroscopy experiment where emission from a QD was measured while spaced closely together with another QD. Since the wavelength calibration (see Figure 4.2d,e) is based on the position of one selected QD, overlap of two emission spectra leads to a shoulder in the emission spectrum that originates from emission of the neighboring QD. In this case the contribution of the neighboring QD adds a shoulder on the blue side of the actual emission spectrum. At times when the selected QD emits weakly, emission signal from this blue (red) ghost QD will lead to a Gaussian fit with a blue-shifted (red-shifted) center wavelength and a broadened emission spectrum. (**b**) Time-integrated emission spectrum of the actual and ghost QD (solid black line), and histogram of the fitted emission peak energies (colored histogram). As a strategy to minimize the occurrence of the experimental artifact, we selected only the wavelength region around the emission peak to be fitted with a Gaussian. As such, the fit of the emission spectrum of the selected QD is at most affected by a shoulder of a neighboring QD's emission spectrum. (**c**–**d**) Same as **a**–**b**, but for a QD that exhibits photodegradation. A characteristic gradual blue shift is apparent in the emission time trace. (**e**–**f**) Correlation between the single-frame (100 ms) emission energy and line width, μ_{SF} and fwhm$_{SF}$. The correlations are shown as 2D histograms of μ_{SF} and fwhm$_{SF}$, relative to the time-integrated peak energy and line width, for the QDs in **a**–**d** (same colors).

Correlation between emission energy and single-frame emission width

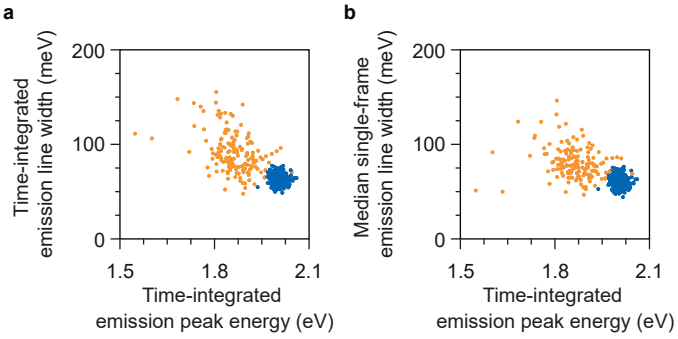

Figure 4.17 | Correlations in single-particle emission properties. (**a**) Correlation between the time-integrated emission peak energy and line width. (**b**) Correlation between the time-integrated emission peak energy and the single-frame (100 ms) emission line width.

Derivation and fitting of $\langle\Delta^2\rangle$-curves

Due to spectral diffusion, the emission peak energy μ_t fluctuates around the maximum of the time-integrated emission spectrum, μ_{TL}. For random diffusion, the expected mean energy displacement of the emission peak from time t to $t + \tau$ is zero:

$$\langle\Delta\rangle = \langle\mu_t - \mu_{t+\tau}\rangle_t = 0. \tag{4.3}$$

The mean square energy difference $\langle\Delta^2\rangle$, however, is nonzero:

$$\langle\Delta^2\rangle = \langle[\mu_t - \mu_{t+\tau}]^2\rangle_t > 0. \tag{4.4}$$

Experimentally, the fitted values of μ_{SF} deviate may from the actual μ^*_{SF} due to Poisson noise, or a non-Gaussian shape of the emission spectrum. As a result, the experimentally obtained $\langle\Delta^2\rangle$-curve can be expressed as

$$\langle\Delta^2\rangle = \int \left[\mu_t - \mu_{t+\tau}\right]^2 e^{-\left[\mu_t-\mu^*_{SF}\right]^2/2\sigma^2} e^{-\left[\mu_{t+\tau}-\mu^*_{SF}+d\mu\right]^2/2\sigma^2} e^{-d\mu^2/2\delta^2} d\mu_t d\mu_{t+\tau} d(d\mu) = \delta^2 + 2\sigma^2, \tag{4.5}$$

where δ^2 is the SD-induced mean square energy difference for emission spectra recorded at different times, and σ is the error on the emission maximum. The magnitude of σ is 1.9 ± 0.8 meV and 3.2 ± 1.1 meV for the experiments on CdSe/CdS/ZnS and InP/ZnSe, respectively. The $\langle\Delta^2\rangle$-curves in Figure 4.4d thus contain the information about the dynamics of SD and are vertically offset by a finite value of σ.

We fitted experimental $\langle\Delta^2\rangle$-curves, obtained with 100-ms binning, to Eq. 4.1 using all data points up to a delay time of 12 s with weights $\sqrt{N_i}\log\left(\tau_i/\tau_{i+1}\right)/\sigma_{\Delta^2_i}$. Here, τ_i is the delay time of data point i, N_i is the number of pairs of frames that contributed and $\sigma_{\Delta^2_i}$ is the error on the data point. We used the logarithmic term to compensate for the fact that there are few data point at small delay times τ and more at longer delays. We fixed the value of $2\sigma^2$ using the mean fit uncertainty of the emission maximum of the respective QD.

Rotational diffusion model for spectral diffusion

We consider a model of a spherical QD in which the lowest-energy exciton state has a static dipole moment p due an off-center core or off-center localization of a charge carrier. The first-order correction to the exciton energy due to the presence of an elementary charge on the QD surface is

$$E = \frac{q}{4\pi\varepsilon\varepsilon_0}\frac{\mathbf{p}\cdot\mathbf{r}}{r^3}, \tag{4.6}$$

where $\mathbf{r}$ is the location of the charge and ε the relative permittivity of the QD material. This expression neglects dielectric contrast between the QD and its surroundings. If we align the z-axis of our coordinate system with $\mathbf{p}$ and express $\mathbf{r}$ in spherical coordinates with $\mathbf{r}$ equal to the QD radius a, the energy correction depends only on the polar angle θ:

$$E(\theta) = \frac{q}{4\pi\varepsilon\varepsilon_0}\frac{p\cos\theta}{a^2}. \tag{4.7}$$

As the simplest possible model of spectral diffusion, we consider the effect of a single charge of fixed magnitude q diffusing over the spherical QD surface. The movement is described in terms of the probability density $f(\theta,\varphi,t)$ to encounter the charge at location (θ,φ) at time t, which obeys

$$D_{\mathrm{rot}}\nabla^2 f = \frac{\partial f}{\partial t}, \tag{4.8}$$

where D_{rot} is the rotational diffusion constant. The general solution to this differential equation is

$$f(\theta,\varphi,t) = \sum_{l=0}^{\infty}\sum_{m=-l}^{l} C_{lm}\,Y_l^m(\theta,\varphi)\,\mathrm{e}^{-D_{\mathrm{rot}}l(l+1)t}, \tag{4.9}$$

where Y_l^m are the spherical harmonics and C_{lm} are expansion coefficients determined by boundary conditions. We see that only the term with $l=0$ survives as t approaches infinity, yielding a uniform distribution $f(\theta,\varphi,t)$. If f is a Dirac delta function at location (θ_0,φ_0) at $t=0$, then the expansion coefficients are

$$C_{lm} = \int_0^{2\pi}\int_0^{\pi} Y_l^{m*}(\theta,\varphi)\,f(\theta,\varphi,0)\sin\theta\,\mathrm{d}\theta\mathrm{d}\varphi = Y_l^{m*}(\theta_0,\varphi_0), \tag{4.10}$$

yielding an expression for the more general probability density to encounter the charge at location (θ,φ) at time t given that it was at location (θ_0,φ_0) at time $t=0$:

$$f(\theta,\varphi,t\,|\,\theta_0,\varphi_0) = \sum_{l=0}^{\infty}\sum_{m=-l}^{l} Y_l^{m*}(\theta_0,\varphi_0)\,Y_l^m(\theta,\varphi)\,\mathrm{e}^{-D_{\mathrm{rot}}l(l+1)t}, \tag{4.11}$$

We obtain spectral-diffusion statistics and dynamics by averaging $E(\theta)$ and $E^2(\theta)$ over the probability density $f(\theta,\varphi,t\,|\,\theta_0,\varphi_0)$. We will use that

$$E(\theta) = \frac{q}{4\pi\varepsilon\varepsilon_0}\frac{p}{a^2}\sqrt{\frac{4\pi}{3}}\,Y_1^0(\theta,0), \tag{4.12}$$

and the orthonormality of the spherical harmonics. This means that from the expansion of f only terms with $l\le 2$ and $m=0$ contribute to spectral diffusion.

$$E(\theta)^2 = \left(\frac{q}{4\pi\varepsilon\varepsilon_0}\frac{p}{a^2}\right)^2\left[\sqrt{\frac{16\pi}{45}}\,Y_2^0(\theta,0) + \sqrt{\frac{4\pi}{9}}\,Y_0^0(\theta,0)\right], \tag{4.13}$$

If the charge starts at (θ_0,φ_0) and then evolves as described by $f(\theta,\varphi,t\,|\,\theta_0,\varphi_0)$, the energy correction starts at $E_0 = E(\theta_0)$ and then evolves as

$$\begin{aligned}\langle E\rangle_\Omega = \int_0^{2\pi}\int_0^{\pi} E(\theta)\,f(\theta,\varphi,t\,|\,\theta_0,\varphi_0)\sin\theta\,\mathrm{d}\theta\mathrm{d}\varphi = \\ \frac{q}{4\pi\varepsilon\varepsilon_0}\frac{p}{a^2}\sqrt{\frac{4\pi}{3}}\,Y_1^0(\theta_0,0)\,\mathrm{e}^{-2D_{\mathrm{rot}}t} = E(\theta_0)\,\mathrm{e}^{-2D_{\mathrm{rot}}t},\end{aligned} \tag{4.14}$$

where $\langle . \rangle_\Omega$ denotes averaging over all possible locations (θ,φ) of the charge at time t. Similarly, the square of the energy correction evolves as

$$\langle E^2\rangle_\Omega = \left(\frac{q}{4\pi\varepsilon\varepsilon_0}\frac{p}{a^2}\right)^2\left[\sqrt{\frac{16\pi}{45}}Y_2^0(\theta_0,0)\,\mathrm{e}^{-6D_{\mathrm{rot}}t}+\sqrt{\frac{4\pi}{9}}Y_0^0(\theta_0,0)\right]= \left[E(\theta_0)^2-E_\infty^2\right]\mathrm{e}^{-6D_{\mathrm{rot}}t}+E_\infty^2, \tag{4.15}$$

where in the last step we have introduced

$$E_\infty^2 = \frac{1}{3}\left(\frac{q}{4\pi\varepsilon\varepsilon_0}\frac{p}{a^2}\right)^2. \tag{4.16}$$

Now we can average the above two expressions over the uniform distribution of possible initial charge locations θ_0:

$$\langle E\rangle_{\Omega,\Omega_0} = \frac{1}{2}\int_0^\pi \langle E\rangle_\Omega \sin\theta_0\,\mathrm{d}\theta_0 = 0 \tag{4.17}$$

$$\langle E^2\rangle_{\Omega,\Omega_0} = \frac{1}{2}\int_0^\pi \langle E^2\rangle_\Omega \sin\theta_0\,\mathrm{d}\theta_0 = E_\infty^2 \tag{4.18}$$

And finally:

$$\langle E_tE_0\rangle_{\Omega,\Omega_0} = \frac{1}{2}\int_0^\pi \langle E\rangle_\Omega E(\theta_0)\sin\theta_0\,\mathrm{d}\theta_0 = E_\infty^2\,\mathrm{e}^{-2D_{\mathrm{rot}}t} \tag{4.19}$$

With the above expressions, we can calculate the mean squared energy shift due to spectral diffusion as a function of delay time t between spectral measurements:

$$\langle (E_t-E_0)^2\rangle_{\Omega,\Omega_0} = \langle E_t^2\rangle - 2\langle E_tE_0\rangle + \langle E_0^2\rangle = 2E_\infty^2\left(1-\mathrm{e}^{-2D_{\mathrm{rot}}t}\right) \tag{4.20}$$

Chapter 5

Finite-size effects on energy transfer between dopants in nanocrystals

This chapter is based on:

Finite-size effects on energy transfer between dopants in nanocrystals. *ACS Nanosci. Au* **2022**, *2*, 111–118

Mangnus, M.J.J.; Zom. J; Welling, T.A.J.; Meijerink, A.; Rabouw, F.T.

Many phosphor materials rely on energy transfer (ET) between optically active dopant ions. Typically, a donor species absorbs light of one color and transfers the energy to an acceptor species that emits light of a different color. For many applications it is beneficial, or even crucial, that the phosphor is of nanocrystalline nature. Much unlike the widely recognized finite-size effects on the optical properties of quantum dots, the behavior of optically active ions is generally assumed to be independent of the size or shape of the optically inactive host material. Here, we demonstrate that ET between optically active dopants is also impacted by finite-size effects: donor ions close to the surface of a nanocrystal (NC) are likely to have fewer acceptors in proximity compared to donors in a bulk-like coordination. As such, the rate and efficiency of ET in nanocrystalline phosphors are low in comparison to that of their bulk counterparts. Surprisingly, these undesired finite-size effects should be considered already for NCs with diameters as large as 12 nm. If we suppress radiative decay of the donor by embedding the NCs in media with low refractive indices, we can compensate for finite-size effects on the ET rate. Experimentally, we demonstrate these finite-size effects and how to compensate for them in YPO_4 NCs co-doped with Tb^{3+} and Yb^{3+}.

5.1 | Introduction

Phosphors convert the color of incident light. Generally, they are crystalline materials doped with optically active dopant ions, such as lanthanide ions. It may be advantageous to incorporate multiple species of dopant ions in the same material. In such a design, one species can have a strong absorption overlapping with the spectrum of incident photons, while a second species emits light of the desired color. To combine these two functionalities, energy transfer (ET) between the dopant species is crucial. ET between lanthanide ions via dipole–dipole interactions has been extensively studied in microcrystalline phosphors and several mechanisms of ET have been identified.[29,140–144] However, certain applications—including nano-thermometry,[15,145,146] bio-imaging and cancer treatment,[9,147] and spectral conversion for photovoltaics[7]—require that the phosphor is a nanomaterial.

Photoluminescence (PL) from doped nanocrystals (NCs) is typically less efficient than that of microcrystalline phosphors, especially when their dimensions become increasingly small.[148,149] This phenomenon is often ascribed to ET from luminescent ions to vibrational modes of organic ligands or solvent molecules, that competes with radiative decay and thereby quenches the PL.[150–155] A common strategy to prevent such quenching is to grow a protective shell of undoped material around the NC core, shielding it from external influences.[148,151–155] An additional feature of doped NCs seems to be mostly overlooked: a donor ion close to the surface of a NC is likely to have fewer acceptors ions in its local environment,[156] so that the probability for ET between the two species is lower. These finite-size effects will reduce the PL efficiency of NCs compared to bulk materials but have never been quantified, nor has the relevant size regime been identified.

Here, we investigate the impact of finite-size effects on ET in Tb^{3+}, Yb^{3+} co-doped YPO_4 NCs. In bulk form, YPO_4:Tb^{3+},Yb^{3+} has previously been identified as a promising blue-to-near-infrared quantum-cutting phosphor for photovoltaics: absorption of a single high-energy photon by a Tb^{3+} donor and subsequent ET to two Yb^{3+} acceptors leads to emission of two near-infrared photons that match the band gap of silicon. We measure the ET efficiency of the Tb^{3+} donor for NCs with different concentrations of Yb^{3+} acceptor ions and make a comparison with their previously investigated bulk counterparts.[142] The ET dynamics in nanocrystalline YPO_4:Tb^{3+},Yb^{3+} are markedly different. As donor ions close to the NC surface have fewer acceptor ions in proximity than donors in a bulk-like coordination, they have a lower rate of ET to acceptors and are less efficient quantum cutters. We demonstrate that this fundamental

limitation on the ET efficiency can be combated by suppressing the competitive pathway of radiative decay from Tb^{3+} donors in media with low refractive indices. Using these photonic effects,[157] we achieve high ET efficiencies despite the negative impact of the NC boundary. Our experimental results are supported by a Monte-Carlo model that accounts for finite-size effects on the ET dynamics of Tb^{3+} donors in NCs. We identify the size range at which the ET efficiency in doped NCs is impacted by finite-size effects, which surprisingly includes NCs with diameters up to 12 nm. Our results are relevant to enable rational design of efficient NC-based phosphor materials that rely on ET between a donor and an acceptor species.

5.2 | Results and discussion

5.2.1 Quantum cutting in YPO_4:Tb^{3+},Yb^{3+} NCs

We synthesized NCs of YPO_4 co-doped with Tb and Yb using the method by Oertel et al.[158] Based on transmission electron microscopy (Figure 5.1a), the NCs are anisotropic and appear similar in shape to the oblate octahedra reported for microcrystalline YPO_4.[159,160] The NCs is have a long side of 8.1 ± 1.0 nm and a short/long axis ratio of 0.63 (see Methods; Figure 5.7). Upon excitation of Tb^{3+}, we observe PL both in the visible and in the near-infrared windows (Figure 5.1b). From experiments on bulk YPO_4, it is known that two competing pathways are responsible for the observed PL. On one hand, the $^5D_4$ level of Tb^{3+} decays by direct photon emission in the green–red. On the other hand, cooperative ET to two Yb^{3+} ions may occur—that is, Tb^{3+} acts as a donor and simultaneously transfers half of the excited-state energy to each Yb^{3+} acceptor—followed by photon emission in the near-infrared.[142]

We systematically measure the excited-state dynamics of the $^5D_4$ donor level for YPO_4 NCs doped with 1% Tb^{3+} and a range of Yb^{3+} concentrations. NCs doped solely with Tb^{3+} exhibit single-exponential decay with a rate of 0.31 ms^{-1} when dispersed in toluene (Figure 5.2a), typical for the rate of photon emission from the $^5D_4$ donor level.[4] By co-doping Yb^{3+} into the crys-

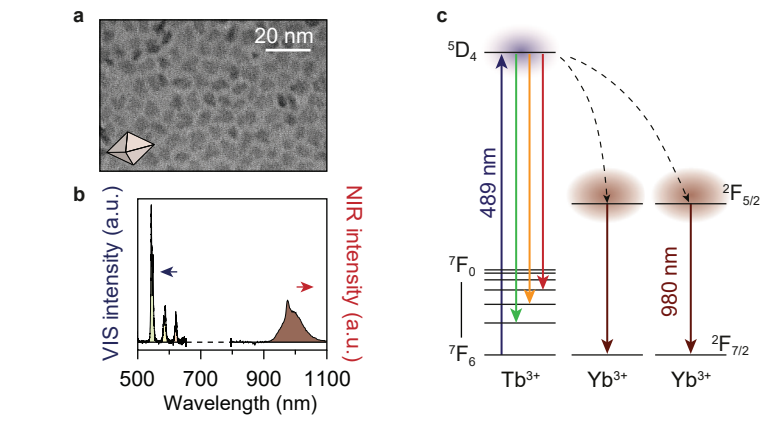

Figure 5.1 | Quantum cutting in YPO_4:Tb^{3+},Yb^{3+} nanocrystals. (a) Transmission electron micrograph of octahedron-shaped YPO_4:Tb^{3+},Yb^{3+} nanocrystals. (b) Visible-near-infrared emission spectrum of $YbPO_4$ doped with 1% Tb^{3+} upon excitation in the $^5D_4$ level. (c) Energy level diagram: upon excitation in the $^5D_4$ level of Tb^{3+} with blue light, cooperative energy transfer yields two excited Yb^{3+} ions that emit in the near-infrared.

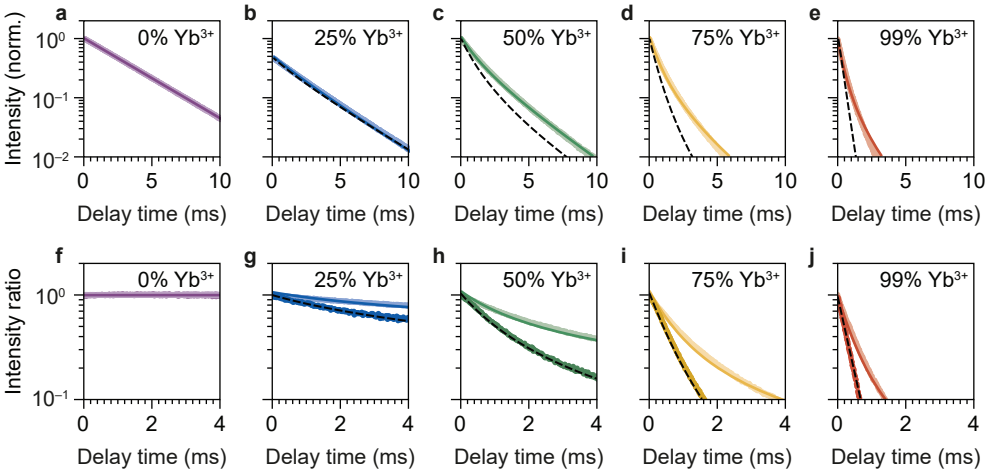

Figure 5.2 | Excited-state dynamics of the Tb^{3+} $^5D_4$ level for NCs dispersed in toluene. (**a**–**e**) PL decay curves of YPO_4:Tb^{3+},Yb^{3+} with Yb^{3+} doping percentages of 0, 25, 50, 75 and 99%. Dashed lines are Monte-Carlo simulations based on Tb^{3+} donors in a bulk-like coordination. Solid lines are fits to the Monte-Carlo model based on Tb^{3+} donors randomly positioned in a nanocrystal with octahedral shape. (**f**–**j**) Contribution of ET to the decay dynamics, obtained by dividing the PL decay curves in panels **a**–**e** by the radiative decay in **a**. Dark curves are the results for bulk YPO_4:Tb^{3+}, Yb^{3+}, reproduced from previous work of Vergeer et al.[142] The solid and dashed lines are the curves predicted by the Monte-Carlo models for bulk and nanocrystalline YPO_4.

tals (Figure 5.2b–e), we introduce the additional decay pathway of cooperative ET. The rate of cooperative ET from a donor to two nearby acceptors at distances r_A and r_B, respectively, scales as

$$\Gamma_{coop} = C_{coop} r_A^{-6} r_B^{-6} \tag{5.1}$$

where C_{coop} is a constant prefactor that we call the cooperative ET strength (previously determined to be 2.0×10^{-6} nm^{12} ms^{-1} for YPO_4:Tb^{3+},Yb^{3+}; Refs. 142, 161). Assuming that dopants randomly occupy Y^{3+} lattice sites, the local coordination of a Tb^{3+} donor with Yb^{3+} acceptors is subject to statistical fluctuations. An ensemble of Tb^{3+} donors thus features a broad distribution of ET rates, giving rise to multi-exponential decay.

The rate at which the $^5D_4$ level decays increases for higher concentrations of Yb^{3+} in our NCs, indicating that ET to acceptors becomes more dominant. Intuitively, we indeed expect that ET is faster when Tb^{3+} donors can transfer their excited-state energy to more acceptors. The total decay dynamics of the Tb^{3+} PL due to the two competing pathways can be described as

$$I(t) = R(t)T(t) \tag{5.2}$$

where $R(t)$ is the contribution of radiative decay of Tb^{3+} and $T(t)$ is the decay resulting from cooperative ET to Yb^{3+}. To get a more direct measure of the ET dynamics, we extract the contribution of $T(t)$ by dividing the decay curves in Figure 5.2a–e by the single-exponential decay dynamics of Tb^{3+} in the absence of Yb^{3+} The curves for the ET dynamics $T(t)$ are plotted in Figure 5.2f–j for different concentrations of Yb^{3+}. For the sake of comparison, the $T(t)$

curves for bulk YPO_4 are shown in the same panels (data reproduced from Ref. 142). The samples with Yb^{3+} all show multi-exponential ET dynamics, reflecting contributions of the many Tb^{3+} centers with different rates of cooperative ET. Interestingly, the ET dynamics in NCs are markedly slower in comparison to their bulk counterpart (Figure 5.2f–j, dark curves). This, in turn, makes the efficiency of ET in NCs lower than in the bulk material.

We resort to theoretical modeling to understand the fundamental differences between ET in NCs and in bulk. Several models exist that describe ET dynamics between dopant ions in a host crystal. In crystalline host materials, acceptor ions can only occupy sites at discrete distances from the donor—that is in shells of nearest neighbors, next-nearest neighbors, etc. While some models provide approximate expressions for the ET dynamics that ignore the discreteness of donor–acceptor spacings,[140,141] more dedicated models account for the crystal structure of the host material.[142,143,161,162] For instance, a donor ion in YPO_4 is coordinated by a shell of 4 nearest neighbors at a distance of 3.76 Å, 4 next-nearest-neighbors at 5.68 Å, and 8 next-next-nearest neighbors at 5.72 Å.[163,164] To identify the mechanism of ET in bulk YPO_4:Tb^{3+},Yb^{3+}, Vergeer et al. used a Monte-Carlo model based on the crystal parameters.[142] The Monte-Carlo algorithm generated a multitude of random different donor environments, from which the ensemble-averaged ET dynamics could be predicted. The experimental data for bulk YPO_4:Tb^{3+},Yb^{3+} were found to be in excellent agreement with a cooperative ET mechanism involving dipole–dipole coupling between a Tb^{3+} donor and two Yb^{3+} acceptors.[142] We compare the result of this previously used Monte-Carlo model to our results on YPO_4:Tb^{3+},Yb^{3+} NCs (dashed lines in Figure 5.2b–e). It is immediately evident that the model does not capture the physics of ET in NCs, as the predicted decay is much faster than the experimental observations. More specifically, the decay dynamics of our NCs feature a range of donor environments with a rate of ET that is slower than predicted. These donor environments must thus have fewer Yb^{3+} acceptors, as expected for donor ions close to the surface of a NC.

We make an extension to the Monte-Carlo model of Vergeer et al.[142] to account for finite-size effects experienced by donor ions in NCs. As microcrystalline YPO_4 is known to crystallize into oblate octahedra,[159,160] we assume that our NCs (Figure 5.1a) have a similar geometry. We model our NCs as oblate octahedra with a short half-axis of 2.5 nm and two long half-axes of 4 nm (see Methods, Figure 5.7). We take note that donor ions positioned close to the NC surface have fewer cation sites in their local environment available for Yb^{3+} acceptors (Figure 5.3). Our extended Monte-Carlo algorithm picks random positions for donor ions in the NC, accounts for the number of available cation sites around the donor, and then generates a random distribution of acceptor ions on these sites. As atomic details of surface faceting will

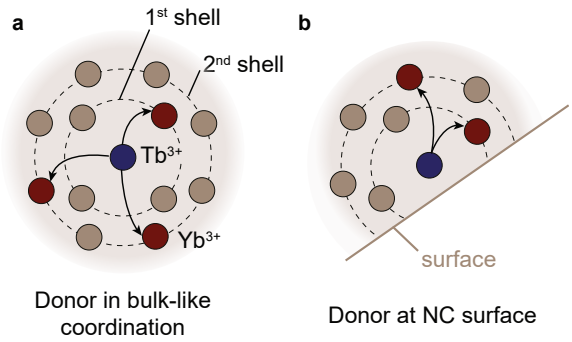

Figure 5.3 | Energy transfer in bulk and nanocrystalline YPO_4:Tb^{3+},Yb^{3+}. (**a**) A Tb^{3+} donor ion (blue) is surrounded by shells of nearest neighbors, next-nearest neighbors, etc., which consist of optically inactive Y^{3+} ions and Yb^{3+} acceptor ions. The exact distribution of Y^{3+} and Yb^{3+} ions is governed by the doping concentration. (**b**) Donor ions close to the NC surface have incomplete shells and accordingly can transfer their energy to fewer acceptor ions.

vary between NCs in the experimental sample, we only take into account the discreteness of donor–acceptor distances but not the discreteness of donor positions within the NC. The Monte-Carlo algorithm is further illustrated in Figure 5.8).

The solid lines in Figure 5.2 are simulated with our extended Monte-Carlo algorithm. The decay curves predicted by our model for NCs have contributions of low ET rates and are in good quantitative agreement with experimental observations. Minor deviations may be explained in terms of slight deviations in size and/or shape of the NCs in the experiments.

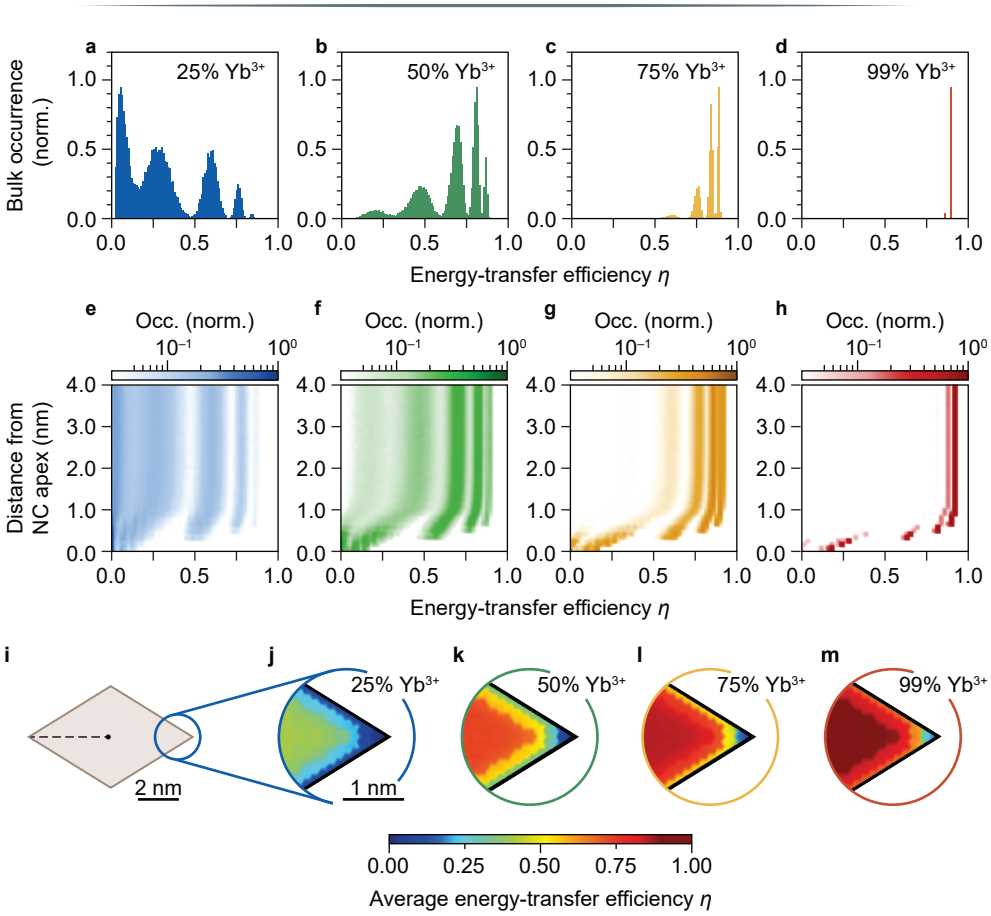

Figure 5.4 | Results of Monte-Carlo simulations of the energy transfer in YPO_4:Tb^{3+},Yb^{3+}. (**a**–**d**) Distribution of energy-transfer efficiencies η in bulk YPO_4:Tb^{3+},Yb^{3+} with Yb^{3+} doping percentages of 25, 50, 75 and 99%. (**e**–**h**) Distribution of energy-transfer efficiencies in nanocrystalline YPO_4:Tb^{3+},Yb^{3+} of octahedral shape, with different distances of the Tb^{3+} donor from the apex of the octahedron (the spatial coordinate on the vertical axis runs along the dashed line in panel **k**, which shows a two-dimensional cross-cut of the octahedral nanocrystal). (**j**–**m**) Two-dimensional zoom-in views of panel **i**, depicting in color-scale how the distribution-averaged energy-transfer efficiency is governed by the position of the donor within the NC. In the above calculations, the surrounding medium is toluene.

The parameter that quantifies the quantum-cutting performance of our NCs is the ET efficiency. A high ET efficiency implies that incident blue photons are effectively converted into near-infrared excitations on Yb^{3+}, while direct photon emission from Tb^{3+} in the visible window is minimal. The ET efficiency can be calculated from the decay dynamics using

$$\eta = 1 - \frac{\int R(t)T(t)\mathrm{d}t}{\int R(t)\mathrm{d}t} \tag{5.3}$$

Importantly, an ensemble of NCs is host to many different donor environments that each may have a different rate of ET and, as such, a different ET efficiency. The distributions of ET efficiencies for Tb donors in a bulk-like (thus, not accounting for finite-size effects) configuration are shown in Figure 5.4a–d for different concentrations of Yb^{3+} acceptors. The wide distributions in ET efficiency are due to the varying occupations of the neighbor shells in proximity of donors. The dominant factor determining the ET efficiency of a Tb^{3+} donor is the Yb^{3+} occupation number of the nearest-neighbor shell, which can have values of 0, 1, 2, 3, or 4 as is evident from the five peaks that are particularly clear in Figure 5.4b.

An important question is how exactly the ET efficiency of donors depends on their vicinity to the NC surface. To this end, we simulated the distribution of efficiencies for donors in the center of the NC (with a bulk-like environment) and those for donor sites closer to the surface. Distributions of the ET efficiency as a function of the distance from the apex of the octahedron (indicated by the dashed line in Figure 5.4i) are shown in the 2-dimensional histograms in Figure 5.4e–h. While for donors in the center of a NC the distribution of ET efficiencies is similar to the distribution in bulk YPO_4:Tb^{3+},Yb^{3+}, a shift to lower efficiencies is apparent for donor sites located within approximately 1 nm of the NC surface. Evidently, finite-size effects impose restrictions on the number of lattice sites close to a donor, which limits the acceptor occupancy and thereby the rate and efficiency of ET. Ultimately, donor ions confined to the NC apex have a vanishing ET efficiency as even the number of nearest-neighbor sites is restricted by finite-size effects. Maps of the average ET efficiency as a function of the spatial coordinate of the donor environment within the NC are shown in Figure 5.4j–m. The maps illustrate that, indeed, the average ET efficiency is substantially lower for donors close to the NC surface—in particular for those confined to the NC apex.

5.2.2 Photonic effects as a means to tune the ET efficiency

For use in applications, reduced ET efficiencies due to finite-size effects are undesirable as they lead to lower output in the near-infrared. The ET efficiency is governed by a competition between two pathways: (1) direct emission of photons from the Tb^{3+} donor and (2) ET to Yb^{3+} acceptors. Previous work has shown that the ET rates depend solely on the distribution of acceptor ions around a central donor ion.[156] Therefore, it is impossible to accelerate ET between Tb^{3+} and Yb^{3+} using external factors. However, interestingly, the radiative decay rate of the Tb^{3+} donor is tunable by changing the photonic environment of the NCs: the radiative rate is accelerated when NCs are embedded in media with a high refractive index, while low-index media slow down radiative decay.[156,157,165] Therefore, using photonic effects, it should be possible to control the competition between undesired radiative decay of Tb^{3+} and desired cooperative ET.

To test this effect, we systematically measured the PL decay dynamics of YPO_4:Tb^{3+},Yb^{3+} NCs dispersed in a range of solvents with different refractive indices. Figure 5.5a shows the PL decay dynamics for NCs doped only with Tb^{3+}. The single-exponential decay of the $^5D_4$ level becomes faster upon changing the solvent from hexane to toluene and carbon disulfide, that is, increasing the refractive index n from 1.38 to 1.50 and 1.62 (Refs. 166,167), respectively

(Figure 5.4b). The decay rate measured previously on bulk YPO_4:Tb^{3+} (n = 1.75, Ref. 168) is even faster.[142] Assuming a unity quantum yield (QY) for bulk YPO_4:Tb^{3+} and allowing for a contribution of non-radiative decay in our NCs with a rate of 0.03 ms^{-1}, we find that our experimentally measured decay rates are in excellent agreement with the NC-cavity model for ellipsoidal NCs (Refs. 157, 169, see Methods). Such a contribution of non-radiative decay present only in NCs is likely due to some quenching of Tb^{3+} by surface defects or ligands and has been reported previously.[157]

Figure 5.4c shows ET efficiencies as obtained using Eq. 5.3. The functions $R(t)$ are extracted from experimental results, and $T(t)$ are either obtained from experimental results or calculated with our Monte-Carlo model. The results for bulk YPO_4:Tb^{3+},Yb^{3+} are based on the experimental data obtained by Vergeer et al.[142] (solid lines). The experimental efficiencies are slightly lower than those predicted by the Monte-Carlo model (dashed lines), possibly due to a contribution of non-radiative relaxation. Filled bars indicate the ET efficiencies measured for NCs embedded in different solvents while the open bars are the results of our Monte-Carlo simulations including finite-size effects. Again, the experimental efficiencies are somewhat lower than those predicted by the model, likely due to non-radiative relaxation pathways. Nevertheless, our experiments and model both show that the ET efficiency is highest when the NCs are dispersed in low-index solvents, such as hexane.

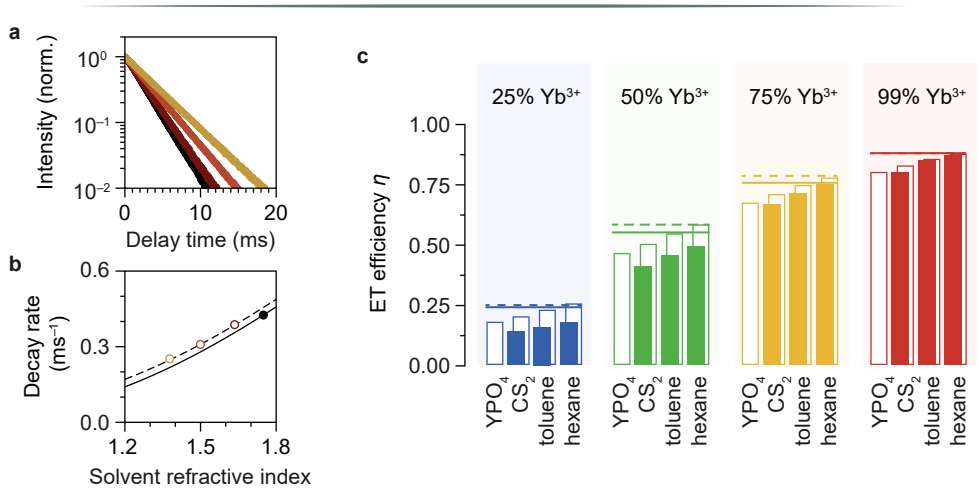

Figure 5.5 | Photonic effects on the radiative decay rate of the donor impact the energy-transfer efficiency. (**a**) PL decay curves of the $^5D_4$ level of Tb^{3+} for NCs dispersed in hexane, toluene, CS_2 and bulk YPO_4:Tb^{3+}(1%) (refractive indices n = 1.38, 1.50, 1.62 and 1.75, respectively; increasingly dark colors). (**b**) Dependence of the $^5D_4$ radiative rate on the refractive index of the medium (open circles: NCs dispersed in different solvents; filled circle: bulk YPO_4:Tb^{3+} (Ref. 157). The solid line is the prediction of the NC-cavity model for ellipsoidal NCs with a QY of 1.0, while the dashed line contains a contribution of non-radiative decay rate of 0.3 ms^{-1}. (**c**) ET efficiencies of NCs dispersed in different environments. Filled bars are the ET efficiencies measured experimentally. Open bars are Monte-Carlo calculations for NCs in media with different refractive indices (YPO_4 denotes an YPO_4:Tb^{3+},Yb^{3+} NC, including finite-size effects on ET, surrounded by a region of undoped YPO_4). Solid lines are the ET efficiencies of bulk YPO_4:Tb^{3+}(1%),Yb^{3+}(x%) obtained experimentally (Ref. 142) and dashed lines are Monte-Carlo calculations.

It is instructive to compare the result of our Monte-Carlo calculations for bulk YPO_4:Tb^{3+}, Yb^{3+} (dashed lines) to those for NCs embedded in an environment with refractive index n = 1.75, similar to that of the YPO_4 host material (leftmost open bars). This comparison highlights the finite-size effects on the ET efficiency without any photonic influences. The ET efficiency for NCs in an environment n = 1.75 is lower than that of bulk YPO_4:Tb^{3+},Yb^{3+} by 10–30% relative, with the biggest decrease for low Yb^{3+} acceptor concentrations. Interestingly, however, this negative effect can be compensated for when the NCs are embedded in solvents with low refractive indices. We thus demonstrate that, by controlling the photonic environment of our NCs, we can control the balance between ET from the donor and direct emission from the donor level.

5.2.3 At what dimensions do finite-size effects play a role?

In the following we will investigate, using theory and simulations, at what NC sizes one should consider finite-size effects on the efficiency of ET between dopants. While our foregoing discussion focused on cooperative ET between a Tb^{3+} donor and two Yb^{3+} acceptors, we here broaden the scope and also consider the most common ET mechanism: first-order ET of the Förster type, i.e. dipole–dipole coupling between a single donor and a single acceptor. We note that other mechanisms of ET with different distance dependencies may occur in some phosphors,[144,170] but we limit our discussion on finite-size effects to ET via the mechanism of dipole–dipole coupling. As examples, we use experimentally determined rate constants for cooperative ET between Tb^{3+} and Yb^{3+} in YPO_4 (k_{rad} = 1/(2.3 ms), $C_{coop} = 2.0 \times 10^{-6}$ nm^{12} ms^{-1}; Ref. 142) and the first-order (cross-relaxation) ET process between Pr^{3+} and Yb^{3+} in $LiYF_4$ (k_{rad} = 1/(35 µs), $C_{et} = 2 \times 10^{-3}$ nm^6 μs^{-1}; Ref. 143). We apply our Monte-Carlo algorithm to calculate the average ET efficiency η in simple spherical NCs as a function of the NC radius. Figure 5.6a,c shows the resulting efficiencies normalized to the bulk ET efficiency η^{bulk}. We see that the ET efficiencies drop by 10% compared to η^{bulk} at a NC radius of 2–6 nm, depending on the doping concentration, for cooperative as well as first-order ET. These significant finite-size effects are consistent with the observation of a 10–30% finite-size effect on cooperative ET in anisotropic YPO_4:Tb^{3+},Yb^{3+} NCs of approximately 8 by 5 nm (full length). We find that finite-size effects in NCs are more pronounced when the corresponding bulk phosphor has a low ET efficiency (that is, the ET efficiency drops more rapidly with decreasing NC radius). This is also evident from Figure 5.4 and we can understand this because phosphors with low bulk ET efficiencies rely more strongly on long-range interactions and are thus more strongly affected by finite-size effects.

To quantify at what length scale finite-size effects become non-negligible, we define the critical NC radius r^*_{NC} where the ET efficiency has dropped by 10% relative to that of the bulk phosphor with the same concentrations of acceptor ions. We calculated the critical radii for cooperative ET between Tb^{3+} and Yb^{3+}, and first-order ET between Pr^{3+} and Yb^{3+}. To investigate a possible effect of the nature of the host crystal, we place these ions in different crystalline environments by substitutional doping, while keeping k_{rad}, C_{coop}, and C_{et} the same. We consider YPO_4, $LaPO_4$, β-$NaYF_4$ and BaF_2, that are different in terms of crystal symmetry, density of lattice sites at which the acceptor ions can substitute, number of nearest-neighbor sites, and the nearest-neighbor distance. More precisely, these four crystals have rare-earth site densities of ρ = 14.0 nm^{-3}, 13.0 nm^{-3}, 13.8 nm^{-3} and 16.8 nm^{-3}, number of nearest-neighbor sites N = 4, 2, 2 and 12, and nearest-neighbor distances of 0.38 nm, 0.41 nm, 0.35 nm and 0.44 nm, respectively.[164,171–173] Figure 5.6b,d show the critical radii for the Tb^{3+}–Yb^{3+} and Pr^{3+}–Yb^{3+} pairs in the different crystalline environments and with different concentrations of acceptors ions. Surprisingly, the impact of the crystal structure of the host material is only marginal (note that all data points of the same color are close together in Figure 5.6b,d), even though this strongly impacts the arrangement of acceptor ions around a donor ion. Instead, the

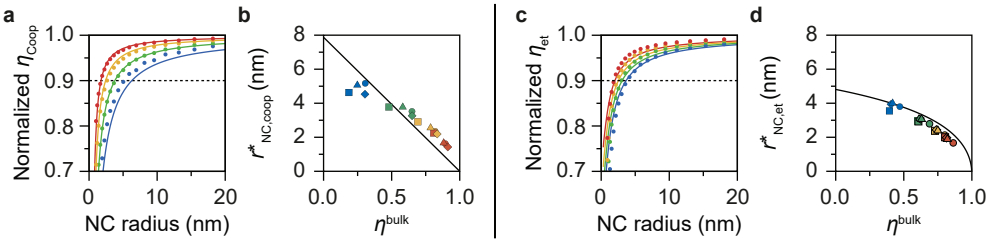

Figure 5.6 | Finite-size effects on the ET efficiency of nanocrystalline phosphors. (**a**) Cooperative ET efficiencies in spherical NCs normalized to the efficiencies of their bulk counterparts, for the Tb^{3+}–Yb^{3+} couple in YPO_4 with Yb^{3+} concentrations of 25, 50, 75 and 99% (blue, green, yellow and red). Solid lines are the predictions of our simplified analytical model (see Methods, Eq. 5.12) and full circles are the results of Monte-Carlo calculations. (**b**) Critical NC radii as a function of the bulk ET efficiency for cooperative ET in the lattices of $LaPO_4$, YPO_4, β-$NaYF_4$, and BaF_2 (squares, triangles, diamonds and circles). We use the rate parameters k_{rad} = 1/(2.3 ms) and C_{coop} = 2.0×10^{-6} $nm^{12}\,ms^{-1}$ that were determined experimentally for YPO_4:Tb^{3+},Yb^{3+}. The black solid line is the result of Eq. 5.4. (**c**,**d**) Same as **a**,**b**, but for first-order ET, using the rate parameters k_{rad} = 1/(35 μs), C_{et} = 2×10^{-3} $nm^6\,\mu s^{-1}$ of the Pr^{3+}–Yb^{3+} couple in $LiYF_4$. In **c** we consider YPO_4:Pr^{3+} with Yb^{3+} acceptor concentrations of 2.5, 5.0, 7.5 and 10% (blue, green, yellow and red). The black solid line in **d** is the result of Eq. 5.5.

critical radius of nanocrystalline phosphors appears to be governed by the ET efficiency of the corresponding bulk phosphor.

While our Monte-Carlo model captures the most important features of ET in nanocrystalline phosphors, it is computationally expensive and complex to implement. It is therefore desirable to have a simpler model that nonetheless provides a good estimate of the critical NC radius. We introduce simple analytical models for first-order ET and cooperative ET (see Methods) that assume a homogeneous distribution of acceptor ions over the volume of the NC and neglects the discreteness of donor–acceptor spacings in a crystalline environment. Despite these simplifications, the resulting analytical expressions are a good prediction for finite-size effects (Figure 5.6a,c). Moreover, the models provide simple and general expressions for the critical NC radius. For cooperative ET the critical NC radius is given by

$$r^*_{NC,coop} = \frac{5}{2} r_{min} \left(1 - \eta^{bulk}_{coop}\right), \tag{5.4}$$

with r_{min} the minimum distance between donors and acceptors in the analytical model (approximately equal to the nearest-neighbor distance in the crystal, with typical values of 0.35–0.4 nm). For first-order ET the expression for the critical NC radius is

$$r^*_{NC,et} = -\frac{20}{3} \frac{\sqrt{1-\eta^{bulk}_{et}} + \left(1-\eta^{bulk}_{et}\right)\left[\frac{1}{2}\ln\left(1-\eta^{bulk}_{et}\right) - 1\right]}{\eta^{bulk}_{et}\ln\left(1-\eta^{bulk}_{et}\right)} R_0, \tag{5.5}$$

with R_0 the Förster radius, which is defined as $R_0 = (C_{et} / k_{rad})^{1/6}$ (Eq. 2.16). The results of Eq. 5.4 and 5.6 are shown as solid lines in Figure 5.6b,d. Interestingly, the critical NC radius depends on the optical properties of the donor–acceptor pair or the acceptor concentration only indirectly through the bulk ET efficiency η^{bulk}. It is clear that, although finite-size effects may be small for phosphors with a high η^{bulk}, critical radii are as big as 6 nm for low values of η^{bulk}.

This suggests that finite-size effects may pose a challenge in the development of various applications that rely on ET and where small NCs are a requirement. For instance, quantum-cutting phosphors most effectively enhance the efficiency of photovoltaic energy conversion when scattering losses are minimized, thus necessitating small particles. Alternatively, small sizes may be essential to use lanthanide-doped NCs as fluorescent probes for high-resolution (in vivo) imaging or sensing.[10,15,151] Furthermore, many phosphor materials are synthesized with dimensions in the critical size regime even though there is no stringent requirement for small NC sizes.[174,175] The significant finite-size effects on ET experimentally demonstrated in Figure 5.4 and calculated in Figure 5.6 are thus important for many nanocrystalline phosphor materials and may occur for any donor–acceptor combination and in any host crystal.

5.3 | Conclusions

We have presented a study on the excited-state decay dynamics of the Tb^{3+} $^5D_4$ donor level in bulk and nanocrystalline YPO_4:Tb^{3+},Yb^{3+} quantum-cutting phosphors to provide insight in the role of finite-size effects on the ET efficiency in nanocrystals. The decay dynamics result from a competition between direct emission of photons in the visible window on the one hand, and ET to Yb^{3+} acceptors on the other hand. We analyzed the dynamics of ET by systematic measurements for different concentrations of acceptor ions and found that, compared to bulk, the ET dynamics are markedly slower in nanocrystalline phosphors. We presented a simple Monte-Carlo model, that randomly simulates many possible environments of a central Tb^{3+}donor ion—both in terms of the distribution of Yb^{3+} acceptors and in terms of the position within the nanocrystal. The model explains the reduced ET rate in NCs as a result of finite-size effects: Tb^{3+} donors located close to the NC surface have on average fewer Yb3+ acceptors in proximity and thus a lower ET efficiency. Although it is not possible to accelerate ET by external factors, the competing pathway of photon emission from the Tb^{3+}donor level can be suppressed. Tuning the photonic environment of the NCs by embedding them in an environment with low refractive index, slows down radiative decay of Tb^{3+}. Using this method, we are able to compensate for the negative impact of finite-size effects on the ET efficiency and, in fact, achieve ET efficiencies in nanocrystalline YPO_4:Tb^{3+},Yb^{3+} that are as high as those of the bulk material. We provide general rules for the critical length scale at which finite-size effects reduce ET efficiencies in NCs. Importantly, while the performance of ultrasmall nanocrystalline phosphors may be improved by controlling undesirable quenching mechanisms related to chemical species at the NC surface, finite-size effects on ET between dopants pose a fundamental limitation that can only be opposed by tuning the photonic environment.

5.4 | Contributions

Jeffrey Zom synthesized the YPO_4 NCs. Mark J. J. Mangnus supervised Jeffrey Zom, and performed optical spectroscopy on the NCs. Mark J.J. Mangnus analyzed and modelled the data. Tom. A.J. Welling performed finite-element simulations of the local field factor. Mark J.J. Mangnus, Andries Meijerink and Freddy T. Rabouw discussed and interpreted the data.

5.5 | Methods

Synthesis and characterization of doped YPO_4 NCs

Chemicals: Yttrium chloride (99.99%, Sigma-Aldrich), terbium chloride (99.99%, Sigma-Aldrich), ytterbium chloride (99.99%, Sigma-Aldrich), methanol (99.6%, Sigma-Aldrich), tributyl phosphate (≥99%, Sigma-Aldrich), diphenyl ether (≥98%, Sigma-Aldrich), tributyl amine (≥98.5%, Sigma-Aldrich), phosphoric acid (≥99%, Sigma-Aldrich), dihexyl ether (97%, Sigma-Aldrich), dodecylamine (98%, Sigma-Aldrich), toluene (99.9%, Sigma-Aldrich), hexane (99%, Sigma-Aldrich), carbon disulfide (≥99%, Sigma-Aldrich). All chemicals were used without further purification, unless specified otherwise.

NCs were synthesized using the method of Oertel et al.[158] Briefly, a clear solution of 10 mmol of rare-earth chlorides (Y, Yb, Tb) in 10 mL of methanol was mixed with 11 mL of tributyl phosphate. Methanol was evaporated under vacuum at room temperature, after which 30 ml of diphenyl ether was added. Following the removal of water under vacuum at 105 °C, 40 mmol of tributylamine and 7 mL of a 2 M solution of phosphoric acid in dihexyl ether was added. Subsequently, the reaction mixture was kept overnight under nitrogen at 200 °C, during which the NCs were formed. Ligand exchange was performed by addition of 50 mL dodecylamine. After an additional 3 hours at 200 °C and cooling down to room temperature, the supernatant was discarded following centrifugation (10 minutes at 800 g) and the residue was redispersed in 10 mL toluene, washed with 15 mL methanol and centrifuged again. The residue was dried under vacuum. NCs were dispersed in hexane, toluene or carbon disulfide for different measurements.

Assuming that our octahedron-shaped NCs are {111}-terminated,[159] the lattice parameters of tetragonal YPO_4 ($a = b = 6.882$ Å) dictate that the octahedra are oblate and have two long axes with length l and one short axis with length w. The ratio $w:l$ equals $\sqrt{c^2/(a^2+b^2)}$ or 0.63:1.

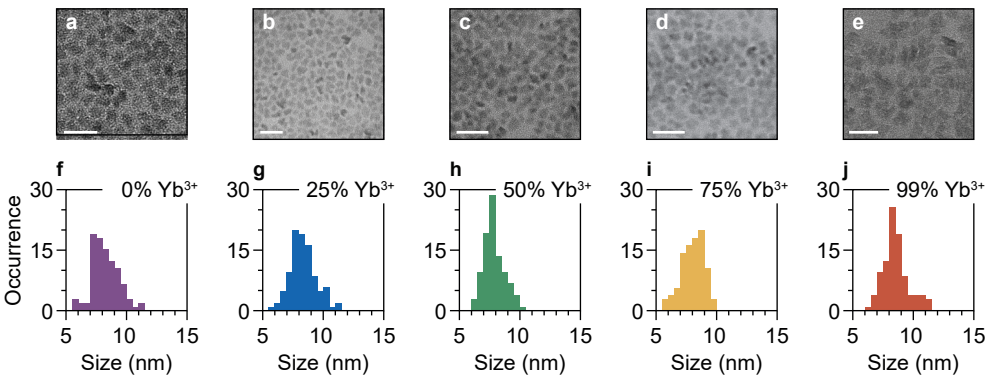

Figure 5.7 | Characterization of NC dimensions. (**a**–**e**) Transmission electron micrographs (TEM) of the YPO_4:Tb^{3+},Yb^{3+} nanocrystals with different concentrations of Yb^{3+} and corresponding size histograms of the long axis (**f**–**j**). Scale bars in **a**–**e** are 20 nm.

Photoluminescence measurements

PL spectra were measured using an Edinburgh Instruments FLS920 fluorescence spectrometer equipped with a Hamamatsu R928 photomultiplier tube for the visible range and a liquid nitrogen-cooled Hamamatsu R5509 photomultiplier tube for the near-infrared range. Tb^{3+} ions were excited using the third harmonic of a Nd:YAG laser at 355 nm with a repetition rate of 20 Hz. The PL decay curve of the 5D4 level was obtained by pulsed excitation with an Ekspla NT342B laser at 488.8 nm, at a repetition rate of 10 Hz. The emission at 545 nm was detected using a Triax 550 monochromator and Hamamatsu H7422-02 photomultiplier tube, coupled to a PicoQuant TimeHarp 260 photon counting module.

Monte-Carlo algorithm

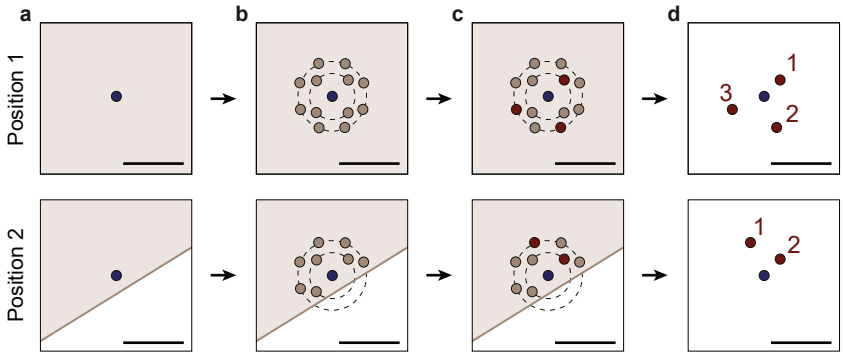

Figure 5.8 | The Monte-Carlo algorithm (**a**) The algorithm picks a random position for the Tb^{3+} donor (blue) within the NC (this is a continuous distribution of positions in three dimensions). The top panel shows a position in the center of the NC, while the bottom panel shows a donor ion positioned close to the surface. (**b**) Based on the position within the NC, the available number of cation sites per shell of nearest neighbors is calculated. This is done by calculating the fraction *f* of every neighbor shell that lies within the NC and using this as a correction factor for the available cation sites. The number of available cation sites is rounded to the closest integer value. For octahedral NCs, we sampled 50 uniformly distributed points on a spherical shell centered on the location of the donor ion, with radius r_i (corresponding to the distance between the central donor ion and the relevant neighbor shell *i*). *f* is calculated by evaluating the fraction of points that lies within the NC. For spherical NCs, a simple analytical solution exists (see Eq. 5.16). In this schematic, only the nearest- and next-nearest neighbor shells are drawn. (c) A random arrangement of Yb^{3+} acceptor ions (red) over the available cation sites (brown) is simulated. The probability for a cation site to be occupied with an acceptor is given by the concentration of Yb^{3+} ions and the acceptor occupancy of every neighbor shell follows a binomial distribution. (d) Every pair of acceptors contributes to the ET rate of the donor. The ET rate contributed by a pair of donors depends on the distances of each acceptor to the donor, as described in Ref. 161.

Nanocrystal-cavity model

The so-called NC-cavity model can be used to describe the dependence of the radiative rate of dopant ions in NCs on the photonic environment.[157] The rate of photon emission depends on the refractive index of the solvent as

$$\Gamma_{\mathrm{rad}}(n) = \Gamma_0 n \chi^2, \tag{5.6}$$

where Γ_0 is the radiative rate of the emitter in vacuum, n is the solvent refractive index and χ is the local-field factor, which accounts for the fact that the local electric field amplitude of photon states at the position of the emitter is different from that of the macroscopic electric field. For spherical NCs, χ^2 is given by

$$\chi^2_{\mathrm{sph}} = \left(\frac{3n^2}{2n^2 + n^2_{\mathrm{NC}}} \right)^2, \tag{5.7}$$

where n_{NC} is the refractive index of the NC. The generalization of χ^2 for dopant ions in ellipsoidal NCs is:[157,169]

$$\chi^2_{\mathrm{ell}} = \left[\frac{1}{3} \frac{n^2}{(1-L_x)\, n^2 + L_x\, n^2_{\mathrm{NC}}} + \frac{1}{3} \frac{n^2}{(1-L_y)\, n^2 + L_y\, n^2_{\mathrm{NC}}} + \frac{1}{3} \frac{n^2}{(1-L_z)\, n^2 + L_z\, n^2_{\mathrm{NC}}} \right]^2, \tag{5.8}$$

where the parameters L_x, L_y and L_z are given by

$$L_x = \int_0^\infty \frac{a_x a_y a_z}{2\sqrt{(s + a_x^2)^3 (s + a_y^2)(s + a_z^2)}} \mathrm{d}s, \tag{5.9}$$

with a_x, a_y and a_z the semiaxes of the ellipsoid.

Analytical models of finite-size effects

To obtain general rules for the NC size range at which one can expect finite-size effects on the ET efficiency, we constructed two simplified analytical models. In contrast to the shell model used in most of the analysis in the main text, these models neglect the discreteness of inter-dopant distances possible in a crystalline host lattice. Cooperative ET is typically relatively weak, meaning that ET does not outpace radiative decay even for a donor ion with two nearest-neighbor acceptors. Consequently, a significant cooperative ET efficiency requires the vicinity of a large number ($\gg 2$) of acceptors near a donor ion. First-order ET, on the other hand, is often so strong that the ET rate between a nearest-neighbor pair is over an order of magnitude higher than the radiative decay rate of the donor ion. A single acceptor close to a donor ion suffices to achieve a considerable ET efficiency. Our two models account for these two fundamentally different dependencies of the ET efficiency on the vicinity of a donor ion. Both lead to simple analytical estimates for the critical NC size below which finite-size effects on the ET efficiency are expected.

First-order energy transfer

In our simplified model of the first-order ET we consider that a donor ion can have an ET efficiency of 0 or 1 depending on whether the donor does or does not have at least one nearby acceptor ion within a distance equal to the Förster radius $R_0 = (C_{\mathrm{et}} / k_{\mathrm{rad}})^{1/6}$. Neglecting the discrete donor–acceptor distances in a crystalline host lattice, the number of rare-earth lattice sites in a sphere of radius R_0 is $N = 4\pi\bar{\rho}R_0^3/3$ (where $\bar{\rho}$ is the lattice site density) if the donor ion is located sufficiently far from the NC surface. If the radial position r_{D} approaches the NC surface at r_{NC}, we use the simplified expression

$$N(r_{\mathrm{D}}) = \bar{\rho} \frac{4\pi}{3} R_0^3 \begin{cases} 1 & ; \quad r_{\mathrm{D}} < r_{\mathrm{NC}} - R_0 \\ 1 - \dfrac{r_{\mathrm{D}} - r_{\mathrm{NC}} + R_0}{2R_0} & ; \quad r_{\mathrm{D}} > r_{\mathrm{NC}} - R_0 \end{cases} \tag{5.10}$$

for the corresponding decrease of $N(r_{\mathrm{D}})$.

Using our simplification that the ET efficiency of a donor ion is either 0 or 1, the average ET efficiency $\eta_{\mathrm{et}}(r_{\mathrm{D}})$ of donor ions located at radial coordinate r_{D} equals the probability that at least one of the $N(r_{\mathrm{D}})$ lattice sites is occupied by an acceptor ion:

$$\eta_{\mathrm{et}}(r_{\mathrm{D}}) = 1 - (1 - \phi)^{N(r_{\mathrm{D}})}, \tag{5.11}$$

where ϕ is the acceptor doping concentration. Averaging Eq. 5.11 over the NC volume yields the average ET efficiency of all donor ions:

$$\langle \eta_{et} \rangle = \frac{3}{4\pi r_{NC}^3} \int_0^{r_{NC}} \eta_{et}(r_D) 4\pi r_D^2 dr_D. \tag{5.12}$$

Evaluating Eq. 5.12 results in a long but analytical expression. We can Taylor expand this expression to first order in R_0/r_{NC} to obtain

$$\langle \eta_{et} \rangle \approx \eta_{et}^{bulk} + 6 \frac{\sqrt{1-\eta_{et}^{bulk}} + (1-\eta_{et}^{bulk})\left[\frac{1}{2}\ln(1-\eta_{et}^{bulk}) - 1\right]}{\ln(1-\eta_{et}^{bulk})} \frac{R_0}{r_{NC}}, \tag{5.13}$$

where the ET efficiency of the bulk material (Eq. 5.11 with N the same for all donor ions) is η_{et}^{bulk}. Note that the second term in Eq. 5.13 is negative for all bulk ET efficiencies between 0 and 1.

We define the critical NC radius as the NC radius for which the average ET efficiency has dropped to $(1-x)\eta_{et}^{bulk}$ with $x = 0.1$. This definition yields the expression for $r_{NC,et}^*$ in Eq. 5.5.

Cooperative energy transfer

We assume a homogeneous density $\bar{\rho}\phi$ of acceptor ions in a spherical NC (where $\bar{\rho}$ is the density of rare-earth lattice sites in the material and ϕ is the acceptor doping concentration), except for a small volume within a distance of r_{min} from each donor ion that contains no acceptors. This excluded volume is necessary to ensure that the average ET rates remain finite and reflects that the donor–acceptor distance r_{DA} in a crystalline host material can never be smaller than the nearest-neighbor distance. To match the calculated ET efficiency (see below) with the one obtained from the shell model, r_{min} should be chosen to be approximately equal to the nearest-neighbor distance in the crystal, which for many materials is on the order of 0.3–0.4 nm.

The function

$$f(r_{DA}, r_D) = \begin{cases} 1 & ; \quad r_D < r_{NC} - r_{DA} \\ 0 & ; \quad r_D < r_{DA} - r_{NC} \\ h(r_{DA}, r_D) & ; \quad \text{otherwise} \end{cases} \tag{5.14}$$

with

$$g(r_{DA}, r_D) = \frac{(r_{NC} + r_D - r_{DA})(r_{NC} - r_D + r_{DA})}{4 r_D r_{DA}}, \tag{5.15}$$

describes what fraction of a spherical shell of radius r_{DA} centered at a donor ion with radial coordinate r_D falls within a spherical NC of radius r_{NC}. Averaging this over all possible donor positions in the NC and accounting for the empty volume V_{min} yields the average density of acceptor ions as a function of the distance r_{DA} from a donor ion:

$$\rho(r_{DA}) = \begin{cases} 0 & ; \quad 0 < r_{DA} < r_{min} \\ \bar{\rho}\phi \dfrac{(r_{DA} - 2r_{NC})^2 (r_{DA} + 4r_{NC})}{16 r_{NC}^3} & ; \quad r_{min} < r_{DA} < 2r_{NC} \\ 0 & ; \quad r_{DA} > 2r_{NC} \end{cases} \tag{5.16}$$

We calculate the average ET rate from a donor ion by integrating the double inverse-sixth-power distance dependence or over the density distribution $\rho(r_{DA})$:

$$\langle \Gamma_{coop} \rangle = C_{coop} \left[\int_{r_{min}}^{2r_{NC}} \rho(r_{DA}) \frac{1}{r_{DA}^6} 4\pi r_{DA}^2 dr_{DA} \right]^2, \tag{5.17}$$

where C_{coop} is the prefactor for the ET strength. Evaluating Eq. 5.17 yields

$$\langle \Gamma_{coop} \rangle = C_{coop} \bar{\rho}^2 \phi^2 \left[\frac{5\pi r_{min}^3 - 36\pi r_{min} r_{NC}^2 + 32\pi r_{NC}^3 + 6 r_{min}^3 \log(2r_{NC}/r_{min})}{24 r_{min}^3 r_{NC}^3} \right]^2. \tag{5.18}$$

We use the average ET rate to calculate the approximate average ET efficiency:

$$\langle \eta_{coop} \rangle = \frac{\langle \Gamma_{coop} \rangle}{\langle \Gamma_{coop} \rangle + k_{rad}}, \tag{5.19}$$

where k_{rad} is the radiative decay rate of a donor ion. Taylor expanding Eq. 5.19 in terms of r_{min}/r up to first order yields

$$\langle \eta_{coop} \rangle \approx \frac{\Gamma_{coop}^{bulk}}{\Gamma_{coop}^{bulk} + k_{rad}} - \frac{9}{4} \frac{k_{rad}\Gamma_{coop}^{bulk}}{(\Gamma_{coop}^{bulk} + k_{rad})^2} \frac{r_{min}}{r_{NC}}, \tag{5.20}$$

where $\Gamma_{coop}^{bulk} = V_{min}^2 \rho^2 C_{coop}/r_{min}^{12}$ is the ET rate in a bulk material (Eq. 5.18 with $r_{NC} \to \infty$). Figure 5.9 shows that the first-order expansion of Eq. 5.20 match the full expressions of Eq. 5.18 well for large NCs with $r_{NC} \gg r_{min}$.

We define the critical NC radius $r_{NC,coop}^{*}$ as the NC radius for which the average ET efficiency has dropped to $(1 - x)$ η_{coop}^{bulk} with $x = 0.1$. This definition yields the expression for $r_{NC,coop}^{*}$ in Eq. 5.4.

Conclusions

We see that both $r_{NC,et}^{*}$ and $r_{NC,coop}^{*}$ depend on the optical properties of the donor–acceptor pair, k_{rad} and $C_{et,coop}$, or on the acceptor doping concentration ϕ only indirectly through the bulk ET efficiency η^{bulk}. Eqs. 5.13, 5.20 as well as Eqs. 5.4, 5.5 thus provide very simple but general expressions for finite-size effects on ET in NCs. All expressions contain a parameter that sets the length scale. For first-order ET this is the Förster radius R_0, which has typical values of 0.5–0.8 nm for ET between lanthanide dopants but can be calculated more precisely if k_{rad} and C_{et} are known. For cooperative ET this is the minimum donor–acceptor distance r_{DA}, which should be taken approximately equal to the nearest-neighbor distance in the crystal and has typical values of 0.35–0.4 nm. Figure 5.6 confirms the validity of the simple analytical models by comparison with more detailed Monte Carlo simulations of ET in NCs.

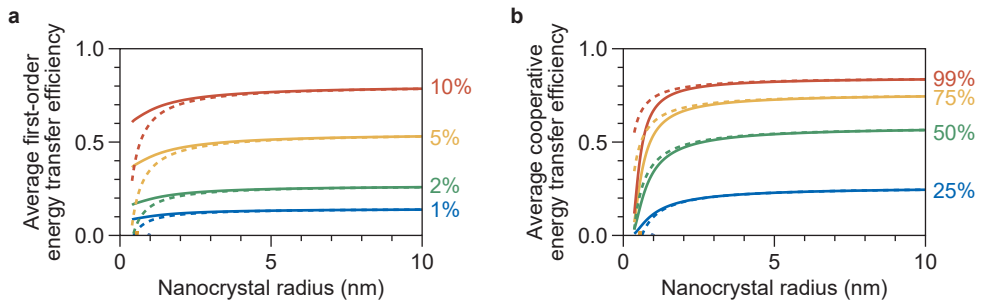

Figure 5.9 | Finite-size effects on the average energy transfer efficiency in a nanocrystal. (**a**) The efficiency of first-order energy transfer calculated using the full expression of Eq. 5.12 (solid lines) and the first-order Taylor expansion of Eq. 5.13 (dashed lines). We used $\bar{\rho} = 14.0$ nm^{-3} as for YPO_4, different Yb^{3+} dopant concentrations ϕ shown in different colors, and rate constants previously measured for Pr^{3+}-to-Yb^{3+} cross-relaxation[143]: $k_{rad} = 1/(35\ \mu s)$ and $C_{et} = 2 \times 10^{-3}$ nm^6 μs^{-1}. (**b**) The efficiency of cooperative energy transfer calculated using the full expression of Eq. 5.19 (solid lines) and the first-order Taylor expansion of Eq. 5.20 (dashed lines). We used parameters of YPO_4: Tb^{3+},Yb^{3+} as input:[142] $k_{rad} = 1/(2.3$ ms), $C_{coop} = 1.99 \times 10^{-6}$ nm^{12} ms^{-1}, $r_{min} = 0.37$ nm is the nearest-neighbor distance, $\bar{\rho} = 14.0$ nm^{-3}, and different Yb^{3+} dopant concentrations ϕ shown in different colors.

Chapter 6

Probing nearby molecular vibrations with lanthanide-doped nanocrystals

This chapter is based on:

Probing nearby molecular vibrations with lanthanide-doped nanocrystals. *Nanoscale,* **2023**, *15*, 16601–16611

Mangnus, M.J.J.; Benning, V.R.M.; Baumgartner, B.; Prins, P.T.; van Swieten, T.P.; Dekker, A.J.H.; van Blaaderen, A.; Weckhuysen, B.M.; Meijerink, A.; Rabouw, F.T.

The photoluminescence (PL) of lanthanide-doped nanocrystals can be quenched by energy transfer to vibrations of molecules located within a few nanometers from the dopants. Such short-range electronic-to-vibrational energy transfer (EVET) is often undesired as it reduces the photoluminescence efficiency. On the other hand, EVET may be exploited to extract information about molecular vibrations in the local environment of the nanocrystals. Here, we investigate the influence of solvent and gas environments on the PL properties of $NaYF_4$:Er^{3+},Yb^{3+} upconversion nanocrystals. We relate changes in the PL spectrum and excited-state lifetimes in different solvents and their deuterated analogues to quenching of specific lanthanide levels by EVET to molecular vibrations. Similar but weaker changes are induced when we expose a film of nanocrystals to a gas environment with different amounts of H_2O or D_2O vapor. Quenching of green- and red-emitting levels of Er^{3+} can be explained in terms of EVET-mediated quenching that involves molecular vibrations with energies resonant with the gap between the energy levels of the lanthanide. Quenching of the near-infrared-emitting level is more complex and may involve EVET to combination-vibrations or defect-mediated quenching. EVET-mediated quenching holds promise as a mechanism to identify the local chemical environment—both for nanocrystals dispersed in a liquid and for nanocrystals exposed to gaseous molecules that adsorb onto the nanocrystal surface.

6.1 | Introduction

Photoluminescence (PL) from lanthanide dopants in nanocrystals (NCs) is often less efficient than from dopants in bulk analogs.[148–150,152,176] Energy transfer from an electronically excited lanthanide ion to high-energy vibrational modes of molecules at the NC surface or in the immediate environment competes with photon emission and therefore lowers the PL quantum yield (QY).[12,150–155,177–179] This electronic-to-vibrational energy transfer (EVET) is a type of Förster resonance energy transfer, which is short-ranged (order of nanometers) and requires that the energy gap between emitting levels of the donor excited state matches the acceptor mode energy of a nearby molecular vibration.[154,177,180–182] EVET is undesired for most applications but can be prevented by growing a protective shell of undoped material around the doped core.[148,151–155,179,183,184] Alternatively, control over EVET rates from different excited states of the lanthanide means control over their respective QYs, which is an interesting strategy to tune the spectral distribution of the PL.[153]

Previous works have shown that the rate of EVET varies strongly for lanthanide-doped NCs dispersed in media with different vibrational energies, such as H_2O and D_2O (with vibrational energies $\hbar\omega$ of ~3600 cm^{-1} and ~2600 cm^{-1}, for the O–H and O–D stretching vibrations),[177,181,182] or aliphatic and aromatic hydrocarbons ($\hbar\omega$ of ~2900 cm^{-1} and 3050 cm^{-1}).[154] Interestingly, as the vibrational energies of molecules are fingerprints of their chemical identity, the rate of EVET should provide information about the local chemical environment of lanthanide-doped NCs.

Here, we investigate the potential of lanthanide-doped NCs to probe nearby molecules with different molecular vibrations. We show that the PL spectrum of lanthanide-doped NCs changes when the NCs are dispersed in different solvents and their deuterated analogues. The PL lifetime exhibits a similar sensitivity, which in some cases can be understood in terms of a simple EVET resonance, while a combination of molecule vibrations is likely responsible in other cases. A second set of experiments with a dry NC film shows sensitivity to gas-phase molecules: EVET to surface-adsorbed gas molecules is sufficiently strong to produce a clear response of the NC emission spectrum. Our experiments highlight that lanthanide-doped NCs can indirectly probe molecular vibrations with fingerprints in the mid-infrared region by giving a response in the visible, in the form of a change in the lanthanide PL spectrum

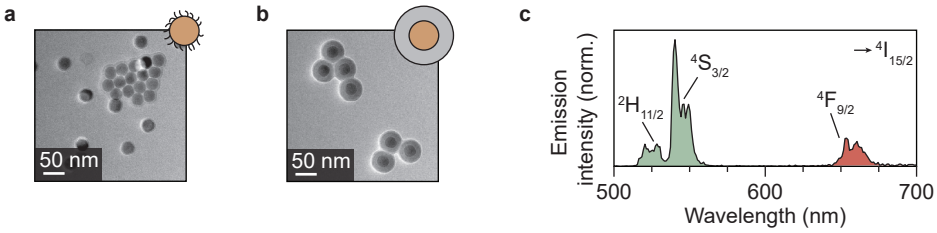

Figure 6.1 | (**a**) Transmission electron microscopy images of the oleic-acid-coated $NaYF_4$:Er^{3+}(2%),Yb^{3+}(18%) NCs. (**b**) Same, but for the silica-coated NCs. The cores are the regions with highest contrast. (**c**) Upconversion emission spectrum of the oleic-acid-coated $NaYF_4$:Er^{3+}(2%),Yb^{3+}(18%) NCs, dispersed in cyclohexane.

and lifetimes. Our findings pave the way for applications in the fields of e.g. catalysis[14] and biosensing[8,11,13], where the PL spectrum of lanthanide-doped NCs can respond to both temperature[15,185,186] and the diffusion, formation, or conversion of molecules in the NC's local environment.

6.2 | Results and discussion

6.2.1 Photoluminescence of upconversion nanocrystals in different chemical environments

We synthesized spherical core-only β-$NaYF_4$:Er^{3+}(2%),Yb^{3+}(18%) NCs with a diameter of 28.5 ± 1.8 nm (Figure 6.1a). The NCs are capped with oleic acid ligands and can be readily dispersed in non-polar media. We used these cores to also synthesize silica-coated $NaYF_4$ particles, with a shell thickness of 14.2 ± 1.2 nm (Figure 6.1b), which are dispersible in polar solvents. Er^{3+}–Yb^{3+} co-doped NCs exhibit near-infrared-to-visible photon upconversion: Yb^{3+} sensitizer ions absorb light at approximately 980 nm and transfer multiple excitations to Er^{3+} to populate visible-emitting energy levels (Figure 6.2a).[181,187–189] As an example, the upconversion emission spectrum of oleic-acid-coated NCs dispersed in cyclohexane (Figure 6.1c) shows the resulting green and red emission lines originating from the $^2H_{11/2}$ / $^4S_{3/2}$ and $^4F_{9/2}$ levels, respectively.

To investigate the impact of solvent molecules on the upconversion PL, we transferred the oleic-acid-coated and silica-coated NCs to a range of solvents, as well as to deuterium-substituted isotopologues of these solvents: H_2O, D_2O, CH_3CH_2OH, CH_3CH_2OD, CD_3CD_2OD, C_6H_{12}, C_6D_{12}, $C_6H_5CH_3$, and $C_6D_5CD_3$. Substitution of hydrogen atoms by the heavier deuterium isotope reduces the vibrational energies of the solvent molecules approximately by a factor $\sqrt{2}$. We measured the upconversion PL of the different samples upon excitation with a 980 nm laser operated at a constant estimated power of 10^{-1}–10^{0} W cm^{-2} to exclude a power-dependent effect.[178,189,190] The relative contributions of green and red PL to the total upconversion PL differs substantially for NCs in deuterated and non-deuterated solvents (Figure 6.1d; see also Figure 6.9). Differences in the relative contributions of the green and red upconversion PL are thus likely a consequence of different rates of EVET due to the shifted vibrational energies of the deuterated solvents. It may be counterintuitive that EVET-mediated PL quenching occurs at all for NCs with a silica shell, which spatially isolates the luminescent core from the surrounding medium. However, silica shells grown via micro-emulsion methods are typically (micro-)porous,[177,191–193] so that small molecules or ions can penetrate and reach sites close to the luminescent core where they are efficient acceptors for EVET.

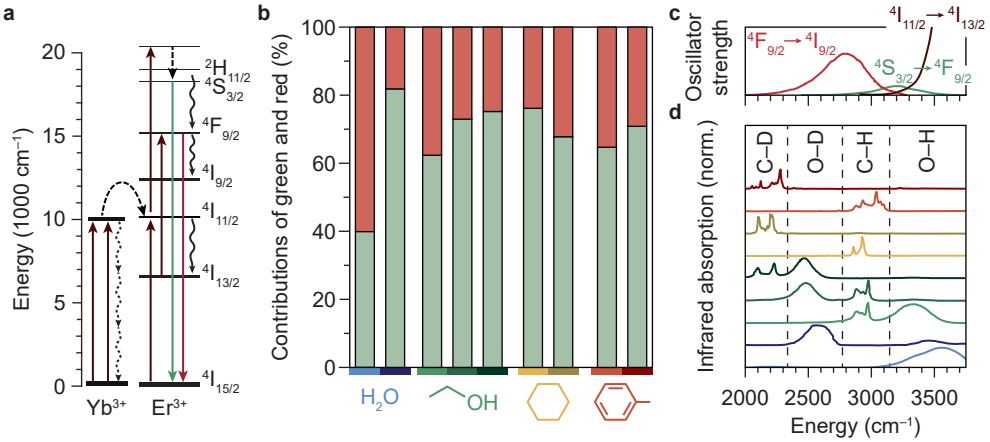

Figure 6.2 | Upconversion luminescence from lanthanide-doped nanocrystals in different chemical environments. (**a**) Upconversion in Yb^{3+}–Er^{3+} co-doped NCs proceeds by excitation of Yb^{3+} sensitizers and subsequent multi-step energy transfer to Er^{3+} ions, which emit in the green and red. Important quenching processes are indicated by black curvy arrows. (**b**) Relative contributions of the green and red PL in different solvents. Measurements are done in H_2O, ethanol, cyclohexane, and toluene under continuous-wave illumination at 10^{-1}–10^{0} W cm^{-2}. Light shades of blue, green, yellow, and red represent the normal solvents; darker shades represent the deuterated isotopologues D_2O, ethanol-d1 (CH_3CH_2OD), ethanol-d6 (CD_3CD_2OD), cyclohexane-d12, and toluene-d8. (**c**) Spectra of the electronic transitions in Er^{3+} that can act as EVET donors (see Methods, Figure 6.8). (**d**) Infrared absorption spectra of solvents molecules, reproduced from Refs.[194,195]. Characteristic vibrational energies of relevant functional groups are highlighted within the dashed regions. Colors are the same as in panel **b**.

Figures 6.2a,c show the energies of some relevant transitions in Er^{3+} that can be bridged by EVET (Figure 6.8), and how they match the vibrational absorption spectrum of the various normal and deuterated solvents used (Figure 6.2d). Different solvents clearly offer different resonances between vibrational modes and Er^{3+} transitions, and the resulting EVET-mediated quenching affects the spectral distribution of the upconversion PL (Figure 6.2b) among the red and green emissions. For example, the green contribution of the PL is low in OH-containing solvents H_2O and ethanol compared to their deuterated analogs. The underlying mechanism could be twofold: EVET from the green-emitting levels ($^4S_{3/2}$ and $^2H_{11/2}$) to OH-vibrations quenches the green PL directly, or EVET from the intermediate near-infrared-emitting $^4I_{11/2}$ level could quench the green PL indirectly. The latter effect establishes a population of Er^{3+} ions in the $^4I_{13/2}$ state from which energy-transfer upconversion to the red-emitting $^4F_{9/2}$ level occurs. As upconversion is a complex higher-order process, pinpointing the exact contributions of the different EVET donor transitions (Figure 6.2c) and vibrational acceptors (Figure 6.2d) to the observed changes in the PL spectrum is challenging. To identify the dominant EVET-mediated quenching pathways, it is important to compare the excited-state dynamics of different energy levels when excited resonantly.

Figure 6.3a–d shows the experimentally obtained decay curves of the green-emitting levels of our Er^{3+}–Yb^{3+} co-doped NCs upon resonant excitation. We used the silica-coated NCs to measure the decay dynamics in the polar solvents water and ethanol, and the oleic-acid-

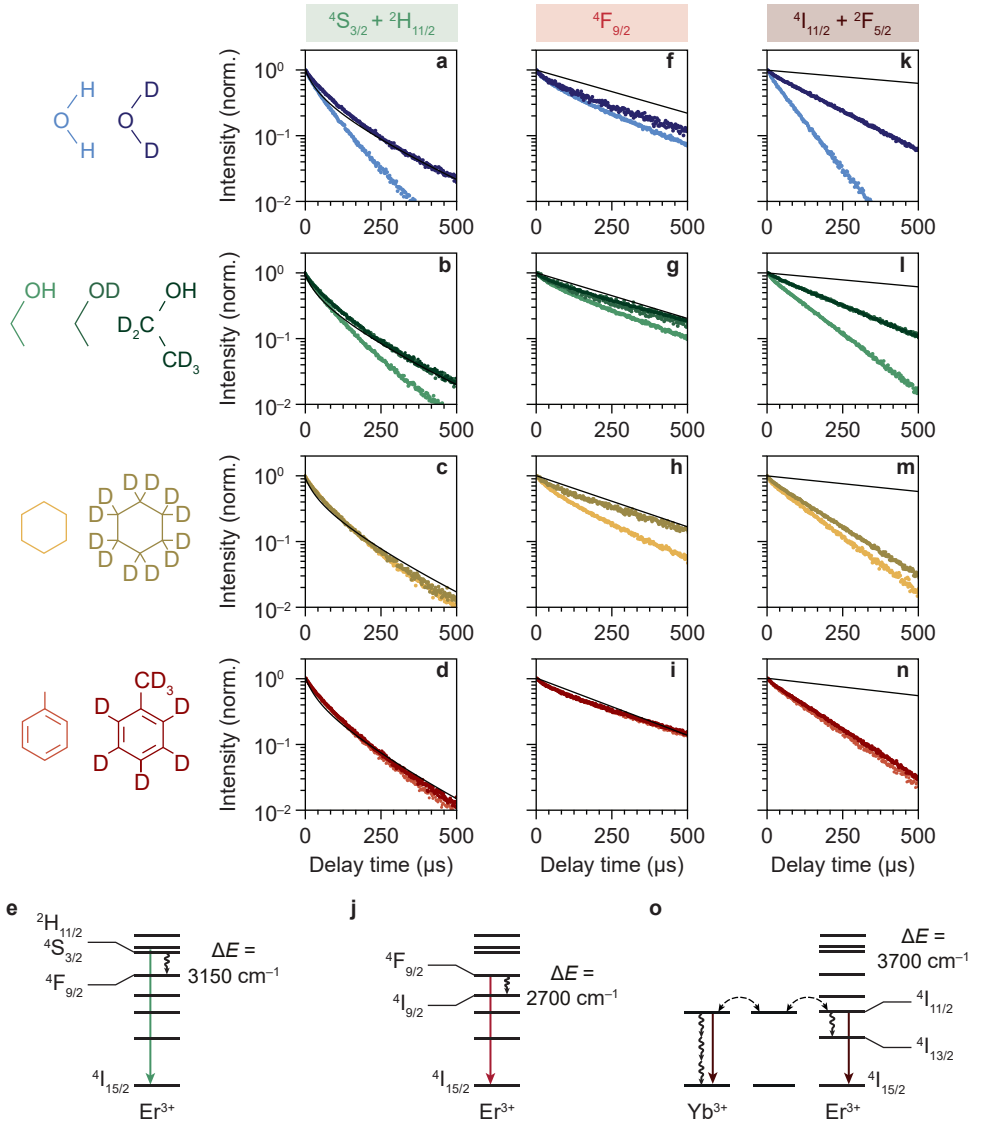

Figure 6.3 | Quenching of erbium levels in different chemical environments. (**a**–**d**) PL decay curves of the green-emitting levels in water, ethanol, cyclohexane and toluene are shown in light shades of blue, green, yellow and red. Decay curves measured in deuterated isotopologues are shown in darker shades of the corresponding colors. Theoretical predictions for decay in the absence of EVET are shown as black lines. (**e**) Schematic of EVET quenching of the green-emitting donor level. (**f**–**j**) Same as **a**–**e**, but for the red-emitting energy levels. (**k**–**o**) Same as **a**–**e**, but for the near-infrared-emitting energy levels.

coated NCs for measurements in cyclohexane and toluene. For comparison, we also show theoretical predictions of the decay dynamics in the absence of EVET-mediated quenching (see Methods; Eqs. 6.3–6.5), based on the NC-cavity model for radiative decay rates[157] and a shell model for ion-to-ion energy transfer that predicts the rate of cross relaxation.[143,144,154,156] Almost all experimental decay curves of the green-emitting levels closely follow the decay dynamics predicted without EVET, including the measurements with NCs dispersed in D_2O, ethanol-d1, and ethanol-d6, but not in H_2O and ethanol (Figure 6.3a–d). This implies that EVET is efficient to acceptors with OH-groups but not to their deuterated counterparts, which have a lower vibrational energy. This is consistent with the observation that the $^4S_{3/2} \rightarrow {}^4F_{9/2}$ donor transition (3000–3400 cm^{-1}), which quenches the green PL, has good overlap with the absorption band of O–H stretching vibrations (3100–3700 cm^{-1}) but not with the deuterated analog (2300–2700 cm^{-1}; Figure 6.2c,d).

For the red-emitting $^4F_{9/2}$ level, cross-relaxation plays no significant role because energy transfer to neighbouring erbium ions in the 4I15/2 ground-state level is prevented by a large energetic mismatch. The theoretical decay curves based on radiative decay closely follow most experimentally obtained decay dynamics (Figure 6.3f–i). However, faster decay rates are exhibited by NCs dispersed in H_2O, D_2O, ethanol, and in particular cyclohexane. This may be explained in terms of spectral overlap of the $^4F_{9/2} \rightarrow {}^4I_{9/2}$ transition (2600–3000 cm^{-1}; Figure 6.2c), which quenches the red PL, and the vibrational energies of the medium around the NCs. Aliphatic C–H stretching vibrations of cyclohexane (2800–3000 cm^{-1}) are resonant with the quenching transition and therefore strong EVET acceptors, while C–D vibrations (2100–2300 cm^{-1}) and aromatic C–H vibrations (3000–3100 cm^{-1} are not.[154] This stresses the importance of resonance as a criterion for EVET to occur. Significant EVET from the $^4F_{9/2} \rightarrow {}^4I_{9/2}$ transition to O–H stretching vibrations is not expected a priori, as the (broad) infrared absorption band measured in liquid phase lies at higher energies (Figure 6.2d). However, O–H and O–D stretching vibrations inside or around the silica matrix have mode energies shifted to ~2750–3500 cm^{-1} and ~2000–2700 cm^{-1}, respectively, as we will demonstrate later (see Figure 6.7). This could facilitate EVET-mediated quenching of the red-emitting level by both O–H and O–D vibrations depending on the molecule. For now, we conclude that the $^4F_{9/2} \rightarrow {}^4I_{9/2}$ EVET donor transition can couple to acceptors with aliphatic C–H vibrations, O–H vibrations, and O–D stretching vibrations.

Our upconversion NCs also emit in the near-infrared PL, but the origin is complex due to energy migration between the Yb^{3+} $^2F_{5/2}$ and Er^{3+} $^4I_{11/2}$ levels, which both emit around 1000 nm and both contribute to the decay curve. Surprisingly, all decay curves of the near-infrared-emitting levels show dynamics that are substantially faster than the radiative decay (Figure 6.3k–n). The strongest quenching is observed for NCs dispersed in H_2O and ethanol, which is consistent with the spectral overlap between the $^4I_{11/2} \rightarrow {}^4I_{13/2}$ donor transition of Er^{3+} (at 3500–3800 cm^{-1}) and the O–H stretching vibration (see Figure 6.2c,d). An important contribution may however be EVET from the $^2F_{5/2} \rightarrow {}^2F_{7/2}$ donor transition of Yb^{3+} (at ~10200 cm^{-1}) to combination-vibrations ($2\nu_1 + \nu_3$; Ref. 196) of hydroxyl groups, as proposed previously by other groups.[177,197] The EVET rate from the near-infrared-emitting levels is effectively enhanced by fast energy migration among and between Er^{3+} and Yb^{3+} ions, facilitating transfer of energy to the NC surface followed by quenching. In contrast, energy migration of green- and red-emitting levels can only proceed via the sparse sublattice of Er^{3+} dopants, which explains why its EVET-mediated quenching of visible emissions is much weaker. Strong quenching by OH vibrations is also understandable in view of the high oscillator strength of the O–H stretch vibration.

Another aspect that influences the efficiency of EVET is the density of acceptor vibrations in the NC's immediate environment. At higher acceptor densities, donors can transfer their energy

to different acceptors, which favors EVET over radiative decay. This consideration explains the difference between strong near-infrared-quenching by water and weaker quenching by ethanol (Fig. 6.3k,l): water has a higher density of OH-vibrations than ethanol in the bulk liquid and may furthermore penetrate the silica shell more effectively. Similarly, the relatively weak quenching observed for silica-coated NCs in deuterated ethanol-d1 and ethanol-d6 (Fig. 6.3l) compared to oleic-acid coated NCs in toluene and cyclohexane (Fig. 6.3m,n) may be attributed to different local densities of CH-vibrations, which are affected by limited penetration of ethanol into silica shell. Note that this density refers to the number of vibrations per unit volume, rather than the number of molecules.

Using the insights into the PL decay dynamics, we can now explain the observed trends of the upconversion PL spectrum in different solvents (Figure 6.2d). Hydroxyl groups quench the green-emitting levels but not the red-emitting levels. In addition, they quench the near-infrared-emitting $^4I_{11/2}$ level of Er^{3+}, transferring population to the $^4I_{13/2}$ level from which energy-transfer upconversion populates the red-emitting $^4F_{9/2}$ level. Hence, quenching by OH groups changes the upconversion pathways through which the red-emitting $^4F_{9/2}$ level is populated, but does not necessarily reduce the $^4F_{9/2}$ population. Both effects result in a lower relative contribution of green upconversion PL for NCs in media with OH groups (e.g. normal water and ethanol). Another important observation is the predominant green upconversion PL in normal cyclohexane compared to the lower green contribution in other organic solvents. This difference can be attributed to the aliphatic C–H EVET acceptor, which strongly quenches the red-emitting level.

Although we can explain many trends in the PL spectrum and lifetimes (Figure 6.2,6.3) in terms of EVET involving a single fundamental molecular vibration that acts as an acceptor, quenching of the near-infrared-emitting $^4I_{11/2}$ level of Er^{3+} by deuterated water and ethanol, or in both isotopologues of cyclohexane and toluene (Figure 6.3k–n) remains complex. Native high-energy C–H or O–H vibrations of oleic acid or silica (silanol groups), or native high-energy lattice vibrations,[198,199] which we ignored in our discussion so far, may play a significant role as EVET acceptors. Alternatively, complex EVET mechanisms involving combination-vibrations of the acceptor may be responsible for quenching in these environments.[177,197] Beyond Er^{3+}, experiments on $NaYF_4$:Ho^{3+} NCs (Fig. 6.10) show a complex interplay between EVET and intrinsic decay dynamics, i.e. radiative decay and cross-relaxation. It is thus difficult to predict a priori which transitions will experience substantial EVET-mediated quenching.

6.2.2 Photoluminescence quenching by molecules from a vapor phase

So far, we have demonstrated that the PL from lanthanide dopants is affected by the solvent in which NCs are dispersed. Now we extend our study by investigating if PL quenching also occurs for EVET acceptors in a gas phase. We measured the upconversion PL of a layer of oleic-acid-coated $NaYF_4$:Er^{3+}(2%),Yb^{3+}(18%) NCs, exposed to a flow of nitrogen gas with controllable amount of water vapor (see Figure 6.4) and excited at excitation powers of approximately 10 W cm^{-2}. At these powers, the green PL contributes between 70 and 74% of the total visible upconversion PL, depending on the gas flow (Figure 6.11, 6.12). Figure 6.5a shows the changes in the green and red PL intensities of the NCs during a prolonged experiment in which we switch between dry nitrogen flow (yellow shaded areas) and flows containing D_2O (purple) or H_2O vapor (blue). The upconversion PL intensity and spectrum of the NCs are unaffected by D_2O vapor. However, introducing H_2O causes a rapid drop of both the red and green upconversion PL, by 20–30%. The PL recovers to ~90% of the initial intensity within 10 minutes upon switching back to dry nitrogen. After 10 min the PL intensity has not yet reached a steady state, implying that further recovery is possible would require more time

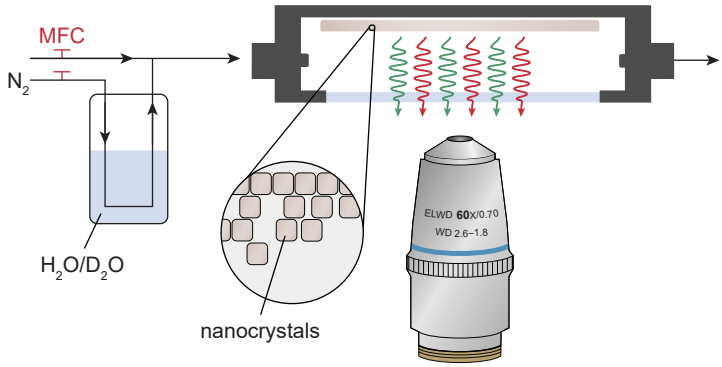

Figure 6.4 | Setup for detection of water vapor with lanthanide-doped upconversion NCs. A drop-casted layer of upconversion NCs is exposed to a constant flow of dry nitrogen carrier gas with controllable amounts of water vapor, using mass-flow controllers (MFCs). The sample is excited in the infrared and emission in the visible is collected using a microscope objective.

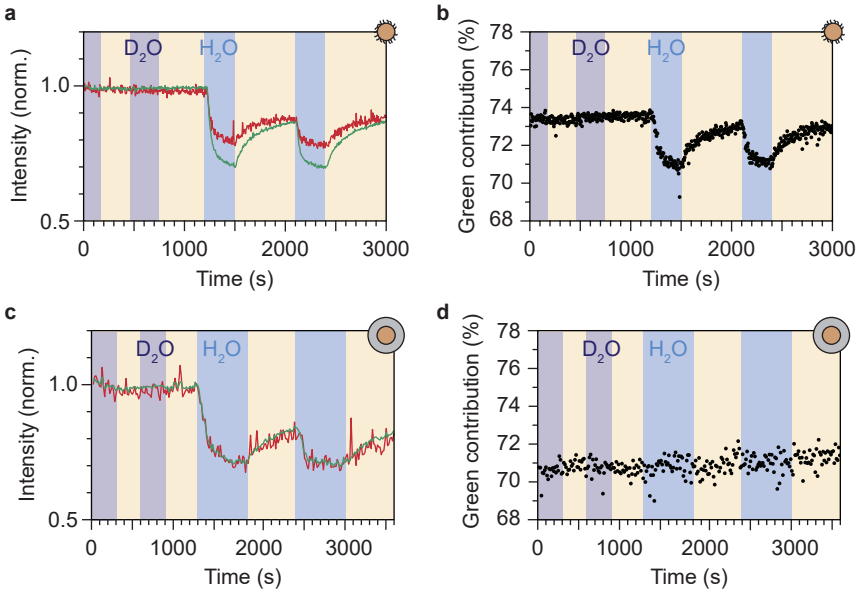

Figure 6.5 | Photoluminescence response of lanthanide-doped upconversion NCs to water vapor. (**a**) Normalized green and red emission intensities of oleic-acid-coated $NaYF_4$:Er^{3+}(2%),Yb^{3+}(18%) NCs, measured under dry nitrogen flow (yellow-shaded areas) or in the presence of water vapor at a relative humidity p/p_0 = 0.17. Blue and purple-shaded areas correspond to a flow of H_2O and D_2O, respectively. (**b**) Same as **a**, but for the contribution of green emission to the upconversion PL. (**c**–**d**) Same as **a**–**b**, but for SiO_2-coated NCs.

(not tested experimentally). Besides a drop in intensity, the relative contributions of green and red upconversion PL change by approximately 4–5% upon introducing water vapor to the gas flow (Figure 6.5b). This effect is approximately 10 times weaker than the difference of 40% observed between the experiments with NCs dispersed in liquid H_2O and D_2O (Figure 6.2b). The amplitude of the decay curves of the green and red PL drops by 31 and 26%, while the apparent decay rates remain approximately unchanged (see Figure 6.6).

We ascribe the drop of the upconversion PL intensity to EVET dominated by quenching of the intermediate near-infrared-emitting $^4I_{11/2}$ level. This is consistent with a simple rate-equation model (Eqs. 6.6–6.8) that describes upconversion as a three-level system (near-infrared, red and green), ignoring the effects of cross-relaxation or energy migration. The model predicts that the steady-state amplitude of the decay curve depends quadratically on the decay rate of the near-infrared-emitting level, and linearly on the red- and green-emitting levels. In this framework, quenching of the Yb^{3+} $^2F_{5/2}$ and the Er^{3+} $^4I_{11/2}$ near-infrared-emitting levels by ~10% causes the 20–30% quenching of visible upconversion PL.

Although quenching of the near-infrared-emitting level by water adsorbates is approximately 10 times weaker than quenching by liquid water (Fig. 2k), the effect is much stronger than expected based on the density of molecules that differs by 4–5 orders of magnitude. Assuming that the rate of EVET scales linearly with the local density of OH-acceptors, this implies that water molecules from the gas flow accumulate in a small volume around the NC—i.e. significant room-temperature adsorption of water molecules on the NC surface causes the observed EVET-mediated quenching of upconversion PL. The (partial) recovery of the PL upon purging with dry nitrogen implies that room-temperature desorption of adsorbates also occurs readily.

The PL from the silica-coated NCs is also quenched upon exposure to a gas flow containing water vapor and recovers partially upon switching back to dry nitrogen flow (Figure 6.5c,d). The time scale of PL recovery is, however, slower than observed for the oleic-acid-coated NCs. This can be attributed to hampered desorption of water molecules due to stabilization of adsorbates in the microporous silica structure. Moreover, the silica-coated NCs exhibit constant relative contributions of the green and red upconversion PL, in contrast to the oleic-acid-coated NCs (compare Figure 6.5b,d). The difference may be a result of different "background quenching" induced by the oleic acid ligands and the silica matrix, which may influence the contributions of different upconversion pathways and the relative importance of any potential water-induced effects. This is reflected by the green contribution to the total upconversion PL, which is higher for oleic-acid-coated NCs (73–74% under dry nitrogen

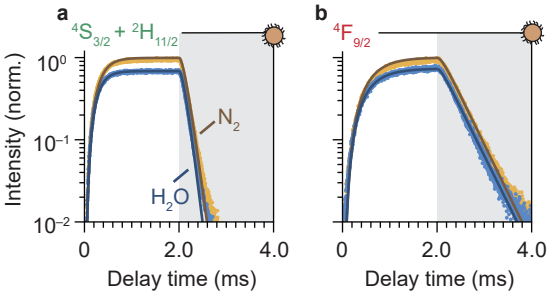

Figure 6.6 | Photoluminescence decay curves of lanthanide-doped upconversion in different gas flows. (**a–b**) PL traces of the green and red emissions excited at 980 nm under dry nitrogen flow (yellow) and in the presence of water vapor (blue). The laser was operated in block-pulsed mode, where it was on for the first 2 ms (unshaded area) and off for the last 2 ms (shaded area). Solid lines are fits to the rate-equation model (Eqs. 6.4–6.6)

flow) compared to silica-coated NCs (70–71%).

We have shown that our NCs respond to water vapor in the atmosphere by a reversible spectral response in the form of a change in intensity and the relative contribution of green to the upconversion PL. This implies that our NCs can be used and re-used to probe vibrations of gaseous EVET acceptors that adsorb and desorb to and from the surface. For a direct proof of water adsorption/desorption, we performed attenuated total reflection Fourier-transform infrared spectroscopy (ATR-FTIR) on films of NCs under the applied gas flows. The infrared absorption spectrum of a layer of oleic-acid-coated NCs features a strong signal around 2900 cm^{-1} due to C–H vibrations of the oleic acid capping ligands (Figure 6.7a). Introducing (deuterated) water vapor to the flow induces an increasing absorption band corresponding to the O–H (O–D) stretching vibration around 2750–3600 cm^{-1} (2000–2700 cm^{-1}), as is clear from the differential absorption spectrum (Figure 6.7b). Increasing the concentration of water vapor leads to an upcoming differential absorption signal of the O–H band (Figure 6.7c), confirming that water adsorbs onto the surface of the NCs. The approximately linear adsorption isotherm (Figure 6.14) is characteristic for nonpolar surfaces with weak water–surface interactions (type III or V according to the IUPAC classification[200]) and implies that water adsorbates cluster around a few favorable adsorption sites rather than forming a monolayer. The absorbance decreases again upon lowering the water concentration in the flow, but adsorption/desorption of H_2O is not fully reversible. The same behavior is observed for D_2O adsorption/desorption. Figure 6.7d shows the dynamics of H_2O adsorption and desorption: upon introducing water vapor, the absorbance signal quickly increases on the time scale of minutes. Removing water vapor from the flow again results in a drop of the signal on time scales of ~10 minutes, but recovery is far from complete. This indicates that a large fraction of water molecules remains in the film of NCs. While the behavior observed in Figure 6.7d is qualitatively similar to that in Figure 6.5a, the near-complete recovery of the upconversion PL seems inconsistent with the far-from-complete recovery of the infrared absorbance. Hampered desorption from the film of the oleic-acid-coated NCs may be explained in terms of strong interaction of water molecules with oleic acid ligands, possibly forming structures in which water is stabilized.[201–203] Such a strong interaction is implied by the shift of C–H stretching absorption lines in the 2800–3000 cm^{-1} range (Figure 6.7b). It is therefore possible that remaining water molecules detected by ATR-FTIR reside in oleic-acid-stabilized structures and are not localized at the NC surface, rendering them inefficient EVET acceptors that do not cause (significant) PL quenching.

The silica-coated NCs feature an absorption band in the 2750–3500 cm^{-1} range due to native silanol Si–O–H vibrations (Figure 6.7e). An absorption band of condensed O–H vibrations appears when flowing water vapor over the layer of NCs (see Figure 6.7f). The isotherm obtained from the O-H stretching band as a function of applied humidity (Figure 6.7g and Figure 6.14) is qualitatively different from the isotherm measured for the hydrophobic oleic-acid-coated NCs (Figure 6.7c). The most important difference is that the silica shell facilitates significant adsorption of water already at a low relative humidity, typical for hydrophilic microporous materials (compare Fig. 6.7c,g and Fig. 6.14). This results in a type I-b adsorption isotherm according to the IUPAC classification[200]. The rapid initial adsorption of water at low pressure corresponds to the filling of the micropores of the hydrophilic porous network of the silica shell with water. Desorption of water adsorbates is incomplete, but more substantial than for the oleic-acid-coated NCs (compare Figure 6.7h with Figure 6.7d). This more substantial release of water adsorbates, however, does not lead to a larger recovery of the upconversion PL (compare Figure 6.5a,c). We propose that, despite desorption of most water molecules from the silica shell, a significant fraction of water adsorbates remains close to the surface of the luminescent cores, possibly kinetically stabilized by slow diffusion through the silica pores. These remaining adsorbates likely reside deep within the silica shell—close to

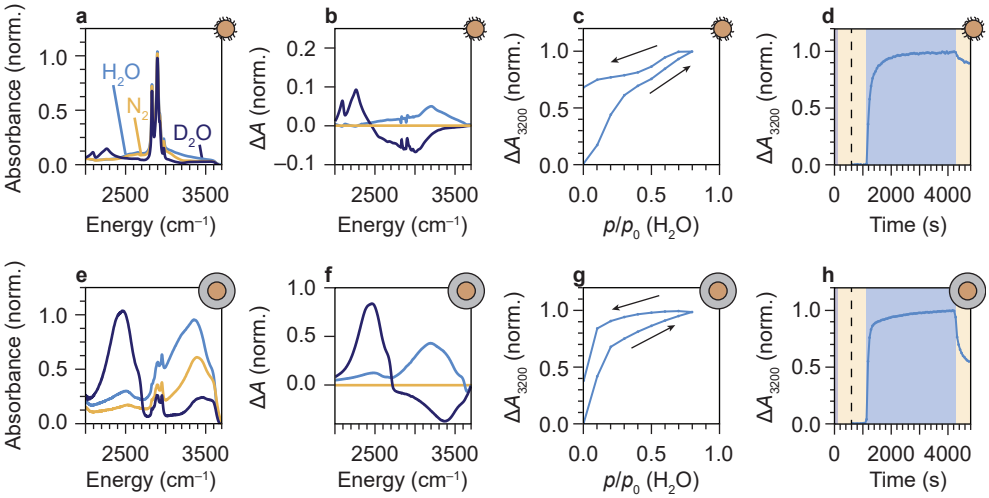

Figure 6.7 | Monitoring the adsorption of water vapor with ATR-FTIR spectroscopy. (**a**) Infrared absorption spectra of a layer of oleic-acid-coated $NaYF_4$:Er^{3+}(2%),Yb^{3+}(18%) NCs, under dry N_2 flow (yellow), and under flows of p/p_0 = 0.20 H_2O (blue) and D_2O (purple). (**b**) Differential infrared absorption spectra, relative to the absorption under dry N_2 flow. (**c**) Differential absorbance at 3200 cm^{-1} as a function of the relative water pressure p/p_0 (H_2O). Arrows indicate the adsorption and desorption isotherms. (**d**) Normalized differential absorbance at 3200 cm^{-1}, measured under dry nitrogen flow (yellow-shaded areas) or in the presence of water vapor (p/p_0 = 0.17; blue-shaded area). The sample was purged with D_2O vapor before starting the experiment. (**e**–**h**) Same as **a**–**d**, but for SiO_2-coated NCs.

the luminescent NC core—and are thus important quenchers. Instead of purging with dry nitrogen gas, a faster method to remove these quenchers for recovery of the upconversion PL is to exchange O–H groups with O–D groups, which happens rapidly upon flushing with D_2O vapor (Figure 6.7f, 6.14).

Optical spectroscopy (Figure 6.4–6.6) and ATR-FTIR spectroscopy (Figure 6.7) are thus both capable of tracking adsorption of molecules on the surface of lanthanide-doped NCs. However, while the PL of the NCs is affected predominantly by short-range (up to several nm) EVET-mediated quenching, ATR-IR spectroscopy also probes vibrations of molecules adsorbed in a larger volume, including interparticle voids. When combined, these two complementary techniques provide information about quenching induced by surface adsorbates.

6.3 | Discussion

Our experiments are a proof of concept, demonstrating that sensing of molecular vibrations based on EVET-mediated quenching of the PL from lanthanide-doped NCs is possible both in a liquid phase and in a gas phase. Important parameters that govern the efficiency of EVET are (a) the match of the energy gap between the emitting levels of the lanthanide ion and the vibrational energy of the EVET acceptor, (b) the oscillator strengths of the electronic donor

transition of the lanthanide ion and of the vibrational mode that acts as an acceptor, and (c) the density of EVET acceptors in the volume that extends several nanometers from the NC surface. While we can describe some EVET-mediated quenching processes in terms of these three considerations, (the degree of) quenching by other EVET acceptors remains difficult to understand. A reason for this might be that combinations of different vibrations may act as EVET acceptors and thereby quench lanthanide levels, as we proposed for quenching of the near-infrared-emitting level of Er^{3+}.

Despite these difficulties, we envision that detection and identification of different molecules with a variety of functional groups may be possible using NCs doped with different lanthanide ions. There is much room for exploration when taking advantage of the wide choice of available lanthanide ions, which all feature different energy separations that could match the vibrational energy of various molecules with different functional groups. For example, Eu^{3+} may be a promising candidate for detection of carbonyl moieties as the $^5D_1 \rightarrow {}^5D_0$ relaxation transition may couple to the C=O vibration with a mode energy of 1700–1800 cm^{-1}. Another example is Ho^{3+}, where EVET from the $^5F_3 \rightarrow {}^5S_2$ transition to C–D vibrations (~2000 cm^{-1}) may alter the shape of the PL spectrum. The sensitivity of lanthanide-doped NCs for the detection of molecules can likely be enhanced by using new oleate-based synthesis procedures that avoid the incorporation of hydroxide ions in the NC host lattice.[204]

We foresee that a molecule-specific response may become possible when exploiting the rich surface chemistry and tunable microporosity[205–207] of a (functionalized) silica shell that acts as a molecular sieve with adjustable sieving and adsorption properties. This would improve the selectivity of EVET-based sensing. Molecule-specific sensing is otherwise challenging, as different molecules can have the same functional groups (compare H_2O and ethanol; Figure 6.3) and the spectrally broad lanthanide transitions often overlap with multiple molecular vibrations (compare Figures 6.2c,d). Alternatively, combining different lanthanide probes with partially overlapping transitions could improve the molecule-specific response.

Our experiments also shed light on the ongoing debate about the peculiar observation of reversible thermal enhancement of upconversion PL in lanthanide-doped NCs.[208–210] While complex quenching mechanisms have been proposed,[208,211,212] our results are consistent with the simple explanation that thermal enhancement stems from temperature-induced removal of water adsorbates that act as EVET acceptors.[182,213–215]

6.4 | Conclusions

We have shown that the PL of lanthanide-doped (upconversion) NCs is sensitive to short-range EVET-mediated quenching by nearby molecular vibrations. The energy level-structure of lanthanide ions contributes to a unique PL spectrum, which is altered when different energy levels are quenched at different rates. We have demonstrated this effect for NCs in solution by measuring the PL decay dynamics in isotopologues of water, ethanol, cyclohexane, and toluene. The comparison of isotopologues highlights the sensitivity of the lanthanide PL to the vibrational spectrum of the surrounding solvents. In many cases, the quenching strength can be rationalized based on the energetic (mis)match of the lanthanide EVET donor and the EVET acceptor mode. We have shown that efficient quenching of the PL does not necessarily require the NCs to be completely surrounded by a medium of quenching molecules. Instead, quenching can already be induced by EVET to molecules adsorbed at the NC surface, such as water. Using the concept of EVET, lanthanide-doped NCs have potential as nanosensors, detecting vibrational modes in their local environment by giving a response in the form of a change in the PL spectrum and lifetimes.

6.5 | Contributions

Thomas P. van Swieten and Ayla J.H. Dekker synthesized the $NaYF_4$ NCs. Mark Mangnus and Thomas P. van Swieten supervised Ayla J.H. Dekker. Bettina Baumgartner performed ATR-FTIR experiments. Ayla J.H. Dekker and Mark J.J. Mangnus performed initial optical spectroscopy experiments with NCs in different solvents. Vincent R.M. Benning carried out the final optical experiments with solvent-dispersed NCs. Mark J.J. Mangnus performed optical spectroscopy with NC-films under different gas flows. P. Tim Prins assisted in the design and construction of the gas-flow cell. Mark J.J. Mangnus performed the data analysis. All co-authors contributed to the interpretation of the data. Freddy T. Rabouw supervised the project.

6.6 | Methods

Synthesis of oleic-acid-coated $NaYF_4$:Er^{3+},Yb^{3+} NCs

Spherical oleic-acid-coated $NaYF_4$:Er^{3+}(2%),Yb^{3+}(18%) core-only NCs were synthesized using the procedure reported in Ref. 185. The NCs were stored in cyclohexane. Part of the NCs was transferred to other nonpolar solvents by precipitating with two volume equivalents of ethanol and redispersing in both isotopologues of cyclohexane and toluene. The other part of the NCs was used to synthesize silica-capped NCs. All chemicals were used without further purification.

Synthesis of $NaYF_4$:Er^{3+},Yb^{3+}@SiO_2 nanoparticles

Silica-coated $NaYF_4$:Er^{3+}(2%),Yb^{3+}(18%) nanoparticles were prepared by silica shell growth around the core-only NCs using a micro-emulsion method.[185,192] The NCs were stored in ethanol. The NCs were transferred to other polar solvents by centrifugation and redispersing. All chemicals were used without further purification.

Photoluminescence measurements

Upconversion PL spectra of solution-dispersed nanoparticles were measured using an Edinburgh Instruments FLS920 fluorescence spectrometer equipped with a Hamamatsu R928 photomultiplier tube. Samples were excited using a 980 nm laser operated in CW-mode (Coherent OBIS LX, 150 mW). To filter out excitation light in the detection path, a Thorlabs FESH0900 900-nm short-pass filter was used. For time-resolved PL measurements of dispersed NCs, samples were excited by direct pulsed excitation at 515, 650 or 980 nm with an Ekspla NT342B laser, at a repetition rate of 10 Hz. The PL at 536 and 660 nm was first filtered using a 516- and 654-nm long-pass filter, respectively, followed by detection using a Triax 550 monochromator and Hamamatsu H7422-02 photomultiplier tube, coupled to a PicoQuant TimeHarp 260 photon counting module. The PL at 1000 nm was detected using a Thorlabs FELH1000 long-pass filter and an avalanche photodiode (APD; Micro Photonics Devices PDM).

Layers of NCs were prepared by drop-casting 50 μL of the NC solution onto a glass coverslip, cleaned using a Diener Zepto low-pressure plasma cleaner, operated at 0.2–0.4 mbar and at the maximum power setting. Optical measurements on as-prepared layers of NCs were conducted on a Nikon Ti-U inverted microscope body, on which the sample was placed inside an air-tight cell (a Linkam THMS600 microscopy stage with a home-built glass lid to enable shorter working distances). Samples were purged with dry nitrogen for at least 30 minutes before starting the measurements. The gas flow through the cell was controlled by combining a flow of dry nitrogen gas (250 mL/min) with a flow (0 or 50 mL/min) of dry nitrogen gas bubbled through deionized H_2O or D_2O. Flow rates were controlled using mass flow controllers. The dry nitrogen gas flow was purified from moist and organic impurities using combined SGT-F0205 and SGT-F0103 filter columns. Assuming that the concentration of water vapor in the bubbler is governed by the saturation pressure of water (p_0 = 31.7 mbar at room temperature; Ref. 216), the partial water pressure in the humid water flow with p/p_0 = 0.17 equals 5 mbar.

A 980-nm laser (Coherent OBIS LX, 150 mW), operated in block-pulsed mode with a repetition rate of 250 Hz and a 50% duty cycle using an Aim-TTi TGA1244 waveform generator, was directed to the sample using a 900-nm short-pass dichroic mirror (Thorlabs DMSP900R), and defocused with a microscope objective (Nikon CFI S Plan Fluor ELWD 60XC) to create a spot with a diameter of ~70 μm. The excitation powers were 5–10 W cm^{-2}. Photoluminescence from the sample was collected using the same objective, guided through a 900-nm short-pass filter (Thorlabs FESH0900), and directed toward the detectors. Using a 50/50 beam splitter, 50 percent of the PL was focused onto the entrance slit of a spectrometer (Andor Kymera 193i) equipped with a reflective diffraction grating (150 lines/mm, blazed at 500 nm), coupled to an electron-multiplying CCD-camera (Andor iXon Ultra 888) operated at a

frame rate of 2 Hz. The other 50 percent was divided among two avalanche photodiode detectors (Micro Photonic Devices PDM) that collected the green and red PL using a band-pass filter (Chroma ET535/70m) and a combination of short- and long-pass filters (Thorlabs FESH0700/Thorlabs FELH0600). Time-tagged time-resolved data were obtained using a quTools quTAG time-to-digital converter, which was connected to both APDs and the laser driver and communicated all photon detection events and laser pulses.

ATR-FTIR spectroscopy

The setup used for ATR-FTIR spectroscopy has previously been described in Refs. 217, 218. Attenuated total reflectance (ATR) crystals (20 × 10 × 0.5 mm, 45°) cut from a double side polished Si wafer were used, with a depth of penetration d_p = 0.52 μm ($\tilde{\nu}$ = 1600 cm^{-1}) and effective path length of $d_{e\parallel}$ = 0.64 μm and $d_{e\perp}$ = 0.32 μm for the two polarization directions, yielding a total effective pathlength of $(d_{e\parallel} + d_{e\perp})N/2$ = 9.65 μm with N = 20. ATR-FTIR spectra were recorded using a Spectrum Three FTIR spectrometer (Perkin Elmer) equipped with a N_2-cooled mercury cadmium telluride (MCT) detector. 128 scans (1 spectrum/min) were averaged. The temperature of the cell was kept steady at 20 °C. The preparation of layers of NCs was analogous to the sample preparation for optical spectroscopy, except that a clean silicon ATR crystal was used as a substrate. The coated ATR crystal was placed inside an air-tight cell and the gas flow through the cell was controlled by combining a flow of dry nitrogen gas (Linde, 5.0) with a flow of dry nitrogen gas bubbled through deionized H_2O or D_2O. The total flow was kept constant at 100 mL min^{-1}. Samples were again purged with dry nitrogen for at least 30 minutes before starting the measurements. Water vapor concentrations were determined by transmission IR spectroscopy in a 10 cm transmission cell with ZnSe windows. Concentrations were obtained from the band areas using reference spectra of 1 ppm/m water from the PNNL database.[219] The application sequence started with pure N_2 flushing for 10 min. Subsequently, the partial pressure was increased/decreased and kept for 3 min to reach step to reach equilibrium.

Oscillator strengths of electronic relaxations in lanthanides

Following Ref. 220, the oscillator strength of an electric dipole transition from an initial electronic state with quantum numbers S, L and J, $\langle 4f,SLJ'\rangle$, to a final state with quantum numbers S', L' and J', $\langle 4f,S'L'J'\rangle$, can be calculated using Judd–Ofelt theory:

$$f_{\mathrm{ED}} = C\frac{\xi^*}{2J+1}\frac{\chi}{n}\sum_{\lambda=2,4,6}\Omega_\lambda\left|\langle 4f,SLJ|U^{(\lambda)}|4f,S'L'J'\rangle\right|^2, \tag{6.1}$$

where C is a prefactor (1.1×10^{11} cm^{-1}), ξ^* is the transition barycenter, χ is the local-field factor (see below) and n is the refractive index of the medium. Ω_λ are the three lattice-specific Judd–Ofelt parameters (4.97×10^{-20}, 1.16×10^{-20}, and 2.03×10^{-20} cm^{-2} for Ω_2, Ω_4 and Ω_6 in β-$NaYF_4$; Ref. 220) and $U^{(\lambda)}$ are the electric dipole tensor operators. The matrix elements $\left|\langle 4f,SLJ|U^{(\lambda)}|4f,S'L'J'\rangle\right|^2$ are tabulated in Ref. 27.

We used the absorption spectrum of bulk β-$NaGdF_4$ powder (Figure 6.8a) to estimate the transition energies and widths. First, we determined the energies of the different levels ξ^* (see Figure 6.8b–c) and (ignoring crystal-field splitting of the $^4I_{15/2}$ ground state of erbium) approximated spectra of the oscillator strength T of a transition from initial state i to final state j as

$$T_{i,j}(\xi) = \int A(\nu_i^* - \xi)\,A(\nu_j^*)\,\mathrm{d}\xi, \tag{6.2}$$

where ξ is the energy difference from the transition barycenter. Theoretical spectra in Figure 6.2c are based on the shape $T_{i,j}(\xi)$, combined with the calculated values of f_{ED} as an amplitude.

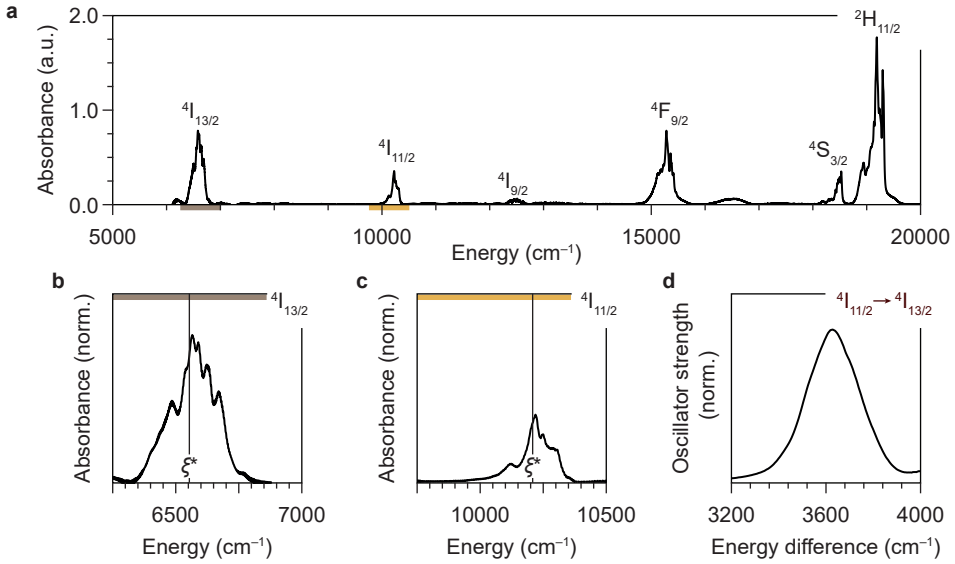

Figure 6.8 | Determining spectra of transition oscillator strengths. (**a**) Absorption spectrum of bulk β-$NaGdF_4$:Er^{3+}(1%) powder. Transitions from the $^4I_{15/2}$ ground state to several excited states are labeled. (**b**) Zoom-in view of a around the $^4I_{15/2} \rightarrow {}^4I_{13/2}$ absorption transition. ξ^* indicates the transition center of gravity. Same as **b**, but for $^4I_{15/2} \rightarrow {}^4I_{11/2}$ absorption transition. (**d**) Spectrum of the oscillator strength of the $^4I_{11/2} \rightarrow {}^4I_{13/2}$ relaxation.

Intrinsic decay dynamics of lanthanide-doped nanocrystals

For lanthanide dopants in NCs with dimensions smaller than the wavelength of light, the radiative decay rate differs depending on the photonic environment according to the NC-cavity model (Eq. 5.6, 5.7, Ref. 157). In Figure 6.3, we used the NC-cavity model (Eq. 6.3, 6.4) and literature values of the radiative decay rates (Ref. 154) to calculate theoretical decay curves of NCs dispersed in different solvents, where the only decay pathway is radiative.

For the green-emitting levels of erbium, cross-relaxation plays an important role in the decay dynamics.[154] The rate of cross-relaxation from a central donor ion depends on its local environment in terms of the number of acceptor ions and the corresponding donor–acceptor distances (with an r^{-6}-dependence). Due to random occupation of rare-earth sites by lanthanide ions, an ensemble of Er-doped NCs features a distribution of cross-relaxation rates. Importantly, donor–acceptor distances are discrete and follow a shell-like structure with nearest neighbors, next-nearest neighbors, etc.[143,144,154,156] The β-$NaYF_4$ unit cell has two different rare-earth sites: the A-site that is 100% available for lanthanide ions, and the B-sites that is 50% occupied by Na ions.[173] For a statistical distribution of lanthanide ions, there is an analytical expression for the (multi-exponential) contribution of cross-relaxation $X(t)$ to the total decay dynamics:[154]

$$X(t) = \frac{2}{3}\left\{\prod_i \left(1-\phi+\phi e^{-C_X t/r_i^6}\right)^{n_i} \times \left(1-\frac{\phi}{2}+\frac{\phi}{2}e^{-C_X t/r_i^{*6}}\right)^{n_i^*}\right\} + \frac{1}{3}\left\{\prod_i \left(1-\frac{\phi}{2}+\frac{\phi}{2}e^{-C_X t/r_i^6}\right)^{n_i} \times \left(1-\phi+\phi e^{-C_X t/r_i^{*6}}\right)^{n_i^*}\right\}. \quad (6.3)$$

The dynamics of cross-relaxation has contributions of erbium donors in A and B sites, with acceptors positioned in shells i, with n_i rare-earth sites at distances r_i and r_i^*. Cross-relaxation becomes faster at higher doping concentrations ϕ. Theoretical decay curves in Figure 6.3a–d contain contributions of radiative decay (Eqs. 6.3–6.4), Er–Er cross-relaxation and Er–Yb cross-relaxation (Eq. 6.5). We used values $C_{Er,Er}$ and $C_{Er,Yb}$ from Ref. 154. Note that the shell model for cross-relaxation does not account for energy migration among lanthanide ions and neglects finite-size effects. The theoretical curves in Figure 6.3a–d therefore serve as a rough estimation of the intrinsic decay dynamics of the green-emitting levels.

Upconversion emission spectra in different solvents

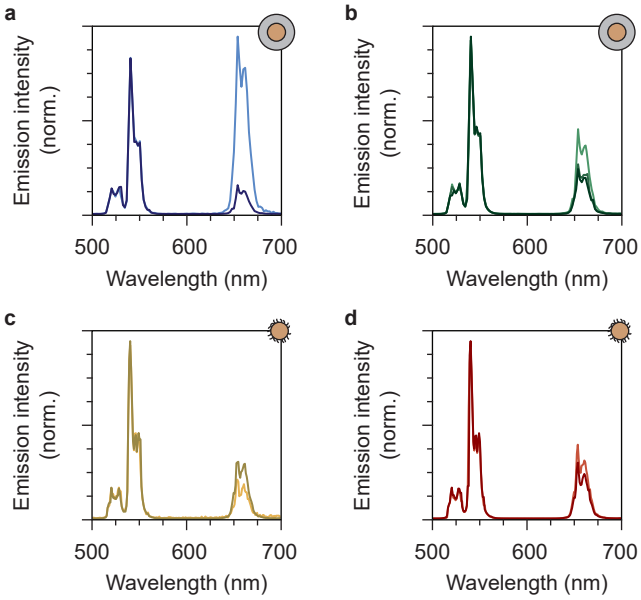

Figure 6.9 | Upconversion emission spectra in different solvents. (**a**) Upconversion emission spectra of silica-coated $NaYF_4$:Er^{3+}(2%),Yb^{3+}(18%) NCs dispersed in normal water and deuterated water (light and dark blue spectra, respectively). (**b**) Same as **a**, but for silica-coated NCs dispersed normal and deuterated isotopologues of ethanol. (**c**) Same as **a**, but for oleic-acid-coated $NaYF_4$:Er^{3+}(2%),Yb^{3+}(18%) NCs dispersed in normal and deuterated cyclohexane. (**d**) Same as **c**, but for oleic-acid-coated NCs dispersed in normal and deuterated toluene.

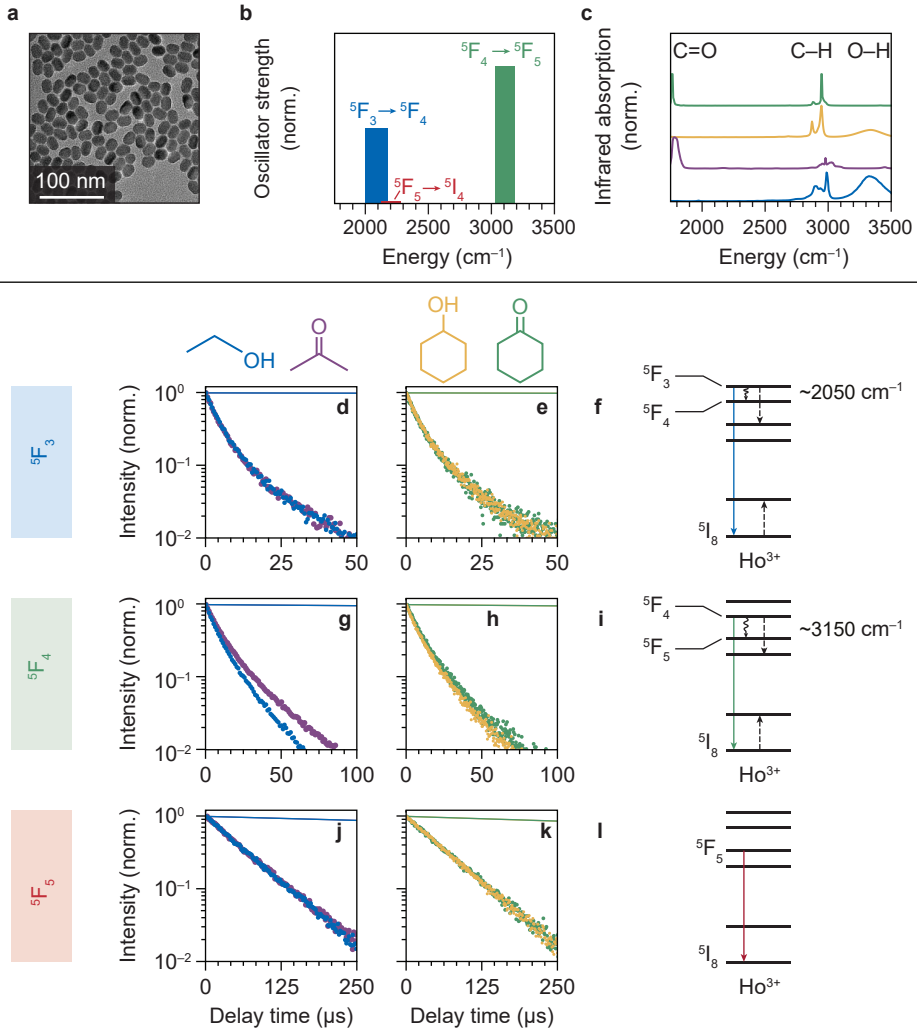

Figure 6.10 | Quenching of holmium levels in different chemical environments. (**a**) Transmission electron microscopy images of the oleic-acid-coated $NaYF_4$:Ho^{3+}(5%) NCs, with a diameter of 31 ± 3 nm. A ligand-exchange procedure, described in Ref. 221, was performed prior to dispersing the NCs in polar solvents. (**b**) Normalized oscillator strengths and energies of important relaxation transitions in Ho^{3+}, calculated using the procedure described above for Er^{3+}.[27] Oscillator strengths f_{ED} of relaxations from the blue-, green- and red-emitting levels are 3.4×10^{-7}, 6.2×10^{-7} and 4.9×10^{-9}. (**c**) Infrared absorption spectra of solvents molecules, reproduced from Ref. 222. (**d**–**e**) PL decay curves of the blue-emitting levels in acetone, ethanol, cyclohexanol and cyclohexanone are shown in purple, blue, green and yellow. Theoretical predictions for radiative decay in the absence of EVET and cross-relaxation are shown as solid lines.[186] (**f**) Schematic of EVET quenching of the blue-emitting donor level. Cross-relaxation is indicated by dashed arrows. (**g**–**i**) Same as **d**–**f**, but

for the green-emitting level. (**j**–**l**) Same as **d**–**f**, but for the red-emitting level. The blue, green and red decay curves were obtained by exciting the sample at 447, 535 and 638 nm, and collecting the luminescence at 487, 542 and 645 nm.

Power dependence of upconversion luminescence

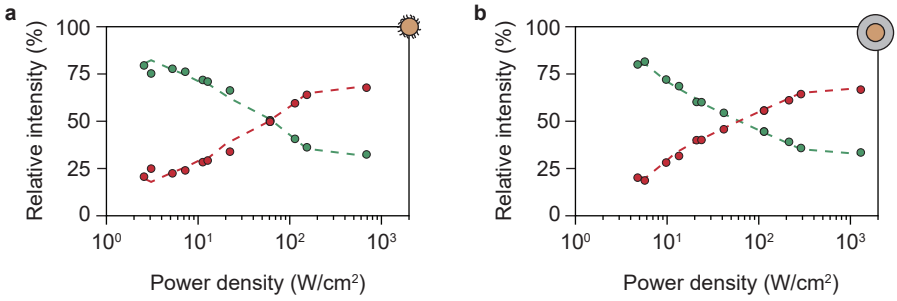

Figure 6.11 | Power-dependence of the upconversion emission spectrum. (**a**) Relative contributions of the green and red upconversion emissions from a film of oleic-acid-coated $NaYF_4$:Er^{3+}(2%),Yb^{3+}(18%) NCs, as a function of power density. The green and red data points correspond to measurements under dry nitrogen flow, and the dashed lines correspond to the same measurements under a flow containing H2O vapor at p/p_0 = 0.17. Note that the power dependence is approximately the same under these two different gas flows. (**b**) Same as a, but for a film of silica-coated $NaYF_4$:Er^{3+}(2%),Yb^{3+}(18%) NCs.

Upconversion emission spectra in different gas flows

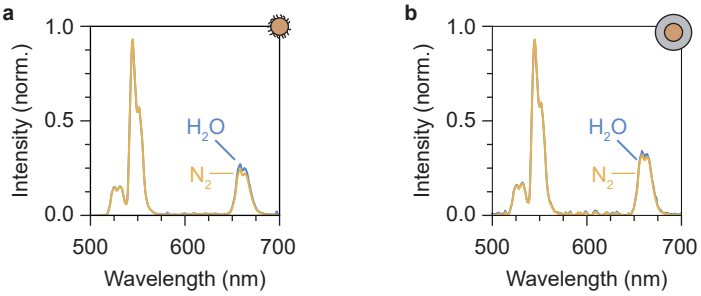

Figure 6.12 | Upconversion emission spectra of nanocrystal films under different gas glows. (**a**) Upconversion emission spectrum of $NaYF_4$:Er^{3+}(2%),Yb^{3+}(18%) oleic-acid-coated NCs under a flow of dry nitrogen and a flow containing water vapor (p/p_0 = 0.17). (**b**) Same as p/p0 = 0.17, but for a film of silica-coated $NaYF_4$:Er^{3+}(2%),Yb^{3+}(18%).

Lifetimes of the green and red upconversion emissions under different gas flows

We describe upconversion luminescence using a simple three-level system. Excitation of a lanthanide ions in the near-infrared with rate k_{exc} builds up a fractional population of ions in an intermediate, near-infrared-emitting level n_{NIR}:

$$\frac{dn_{NIR}}{dt} = +k_{exc}\left[1 - n_{NIR}(t)\right] - k_{ET}n_{NIR}^2. \tag{6.4}$$

Upconversion proceeds by ET from these near-infrared-emitting level, with rate k_{ET}. Populations of the green- and red-emitting levels n_G and n_R are

$$\frac{dn_{R,G}}{dt} = +k_{ET}n_{NIR}^2(t) - k_{R,G}n_{R,G}, \tag{6.5}$$

with $k_{R,G}$ the decay rates of the two levels. The assumption of weak excitation is valid as we estimate $k_{exc} \approx 10^{-4}$ ms^{-1} (using the absorption cross-section of ytterbium in $NaGdF_4$ 1.1×10^{-21} cm^2 (Ref. 220) and an excitation power of 10 W cm^{-2})—much slower than even the bulk radiative decay rate of ytterbium (0.58 ms^{-1}; Ref 154). Furthermore, we do not take into account the $NaYF_4$ crystal structure and ignore the effects of cross-relaxation and energy transfer. We fitted the decay curves in Figure 6.6 to the model (Eq. 6.6,6.7), assuming the limit of weak excitation and assuming a steady-state population of the green and red-emitting levels after 2 ms of laser excitation. The resulting fit parameters are $k_{NIR}^{N_2}$, $k_{NIR}^{H_2O}$, $k_G^{N_2}$, $k_G^{H_2O}$, $k_R^{N_2}$ and $k_R^{H_2O}$ of 15.7, 17.4, 7.0, 7.8, 2.5 and 2.6 ms^{-1}.

In the limit of low excitation power (i.e. $k_{exc} \ll k_{NIR}$), the steady-state intensity of the green and red emissions scales as

$$I_{RG}^{SS} \propto k_{R,G}k_{NIR}^2. \tag{6.6}$$

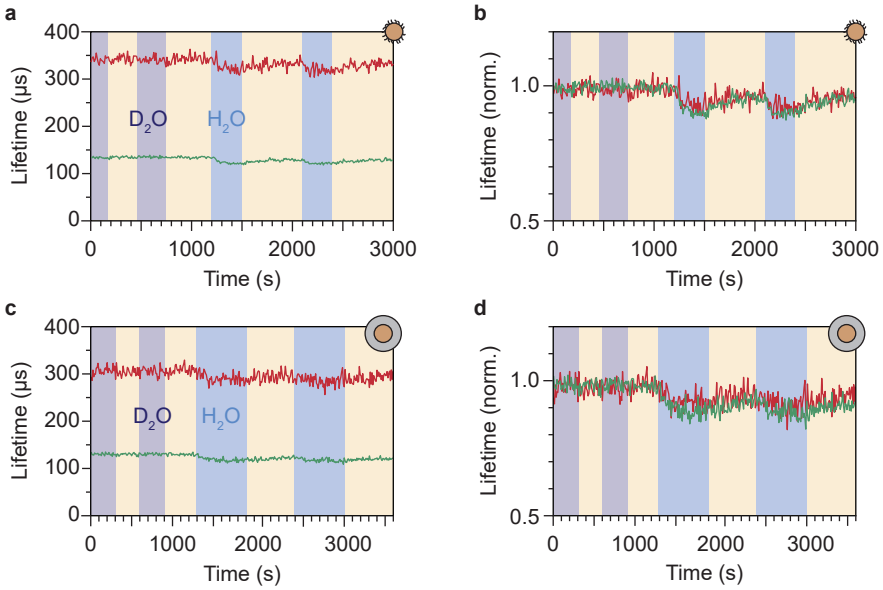

Figure 6.13 | Upconversion emission lifetimes under different gas glows. (**a**) Upconversion emission lifetimes of $NaYF_4$:Er^{3+}(2%),Yb^{3+}(18%) oleic-acid-coated NCs, under changing flows of dry nitrogen and a flow containing water vapor (p/p_0 = 0.17; blue shaded areas for H_2O and purple for D_2O). Lifetimes are obtained by fitting a single exponential to decay curves with an integration time of 10 s. (**b**) Same as **a**, but normalized to the lifetime under dry nitrogen flow. (**c**–**d**) Same as **a**–**b**, but for a film of silica-coated $NaYF_4$:Er^{3+}(2%),Yb^{3+}(18%) NCs.

Equilibrium adsorption isotherms

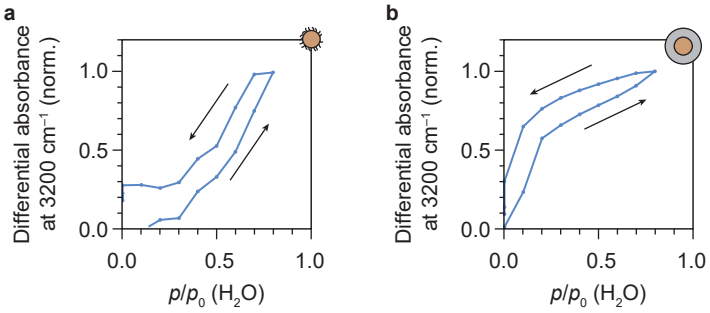

Figure 6.14 | Equilibrium adsorption isotherms of water vapor based on ATR-FTIR spectroscopy. (**a**) Differential absorbance at 3200 cm^{-1} as a function of the relative water pressure p/p_0 (H_2O), for a film of oleic-acid-coated $NaYF_4$:Er^{3+}(2%),Yb^{3+}(18%) NCs. Arrows indicate the adsorption and desorption isotherms. (b) Same as a, but for adsorption/desorption of H_2O on a film of silica-coated $NaYF_4$:Er^{3+}(2%),Yb^{3+}(18%) NCs. These isotherms were obtained under equilibrium conditions after prior exposure to water vapor.

Exchange experiments with D_2O and H_2O vapor

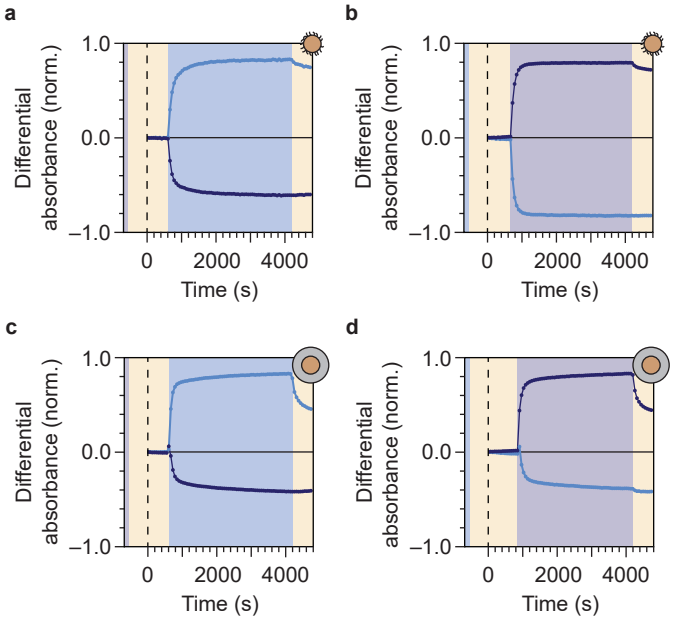

Figure 6.15 | Upconversion emission spectra in different solvents. (**a**) Normalized differential absorbance at 3200 cm^{-1} (blue data points) and 2270 cm^{-1} (purple) for a film of oleic-acid-coated $NaYF_4$:Er^{3+}(2%),Yb^{3+}(18%) NCs NCs, measured under dry nitrogen flow (yellow-shaded areas) or in the presence of H_2O vapor (p/p_0 = 0.17). The sample was purged with D_2O vapor before starting the experiment. (b) Same as a, but for the same film under exposure to D_2O vapor (p/p_0 = 0.17) and prior purging with H_2O vapor. (**c**–**d**) Same as **a**–**b**, but for a film of silica-coated $NaYF_4$:Er^{3+}(2%),Yb^{3+}(18%) NCs.

Chapter 7

Summary and outlook

We have studied the emission properties of quantum dots and lanthanide-doped nanocrystals using a variety of spectroscopic techniques. In this chapter, we summarize the most important conclusions and discuss opportunities for future research.

7.1 | Characterizing and understanding variations and fluctuations of single-quantum-dot emission properties

Developing quantum dots (QDs) for applications in future devices is a challenge on several frontiers. Control over particle sizes and shapes is a prerequisite to achieve control over the optical properties of different types of QDs. However, rational design of next-generation QDs requires a deep understanding of photoluminescence mechanisms, as well as competing pathways that quench the emission. Whereas the community has achieved an advanced level of understanding concerning the photoluminescence mechanism of quantum-dot structures based on the workhorse material CdSe, there is a great urge for new types of QDs of different compositions. For instance, we need to explore alternative materials with reduced toxicity, such as the $CuInS_2$- and InP-based QDs that we studied in **Chapters 3, 4**.

In **Chapter 3**, we used single-particle spectroscopy to characterize the peculiar emission properties of single $CuInS_2$ QDs. We found that emission line widths of single QDs are of the order of 200 meV, much broader than the typical line width of CdSe-based QDs, which are approximately 60 meV. We explain large particle-to-particle variations of the emission energy in terms of the hole, which localizes on copper-related sites at different positions within the nanocrystal. When the hole localizes off-center, attractive Coulomb interactions with the delocalized electron are weaker, and the emission energy is higher. Off-center localization of the hole also implies that CuInS2 QDs have a dipolar excited state. We explain the observed spectral diffusion in terms of the quantum-confined Stark effect, where fluctuations of an external electric field cause large fluctuations of the emission energy and lifetime.

In **Chapter 4**, we studied particle-to-particle variations of emission properties within a batch of InP-based QDs. To obtain statistically strong information about batch properties, we developed multiparticle spectroscopy (MPS) as a high-throughput method to measure (fluctuations of) many single-particle emission spectra simultaneously. The batch of InP-based QDs consisted of some emitters with a color purity on par with that of superior CdSe-based QDs. However, the particle-to-particle variations were large, and some QDs featured enormous time-to-time fluctuations of their emission spectrum. In the framework of the quantum-confined Stark effect, we proposed two different mechanisms that may be responsible for spectral diffusion in InP-based QDs. This includes the possibilities of an excited state with a (shell-) delocalized hole or a dipolar excited state with a localized (trapped) charge carrier.

We have shown that optical spectroscopy at the single-particle level is a vital tool to uncover the mechanisms of photoluminescence in new generations of QD structures. However, large particle-to-particle variations of emission properties within a batch of nominally identical QDs remain puzzling. High-resolution electron microscopy and elemental mapping are complementary techniques that will likely play an important role to understand structure-performance relationships. For instance, structural defects imaged by electron microscopy may be related to changes in the emission properties as characterized using single-particle spectroscopy. Rational design of improved QDs may then aim at combating structural defects that hamper the photoluminescence efficiency or color purity.

From a technological viewpoint, one may argue that striving for rational design of QD structures is a naive and unnecessary quest. Rather than that, synthesis conditions may be

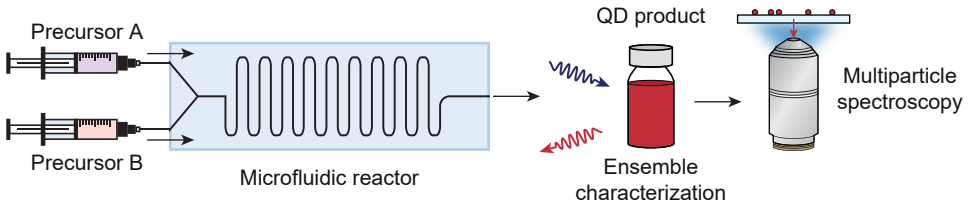

Figure 7.1 | Data-driven optimization of quantum-dot synthesis procedures. Microfluidic reactors offer excellent control over synthesis parameters such as precursor concentrations, flow rates, and temperature. These synthesis parameters can be optimized rapidly based on quantum-dot emission properties measured at the ensemble scale and single-particle level.

optimized in microfluidic continuous-flow reactors,[223–226] for instance based on real-time information about performance indicators such as the ensemble-scale emission color and brightness.[227] Tunable synthesis parameters could for instance be the concentration, flow rate, and reactivity of precursors, and the temperature on the microfluidic chip (Figure 7.1). Although MPS is probably too slow for real-time monitoring of particle-to-particle variations and time-to-time-fluctuations of the emission properties, it could serve as an important characterization technique to find synthesis conditions that yield QDs with uniform emission properties—including reduced spectral diffusion and photoluminescence blinking.

7.2 | Lanthanide-doped nanocrystals: the competition between emission and energy transfer

Optical transitions in lanthanide-doped phosphors involve a rearrangement of electrons among the 4f-orbitals of the lanthanide dopants. Emission energies are well-defined and barely affected by the host crystal in which the lanthanides are incorporated. The general belief is that, just like in bulk crystals, the emission properties of lanthanide ions in nanocrystals are independent of their local environment. In **Chapter 5**, we challenged this viewpoint by showing that dopant-to-dopant energy transfer is hampered in NCs, which alters the photoluminescence output. In **Chapter 6**, we investigate how a special type of ET—from dopant ions to molecular vibrations at the NC surface—quenches the luminescence from specific lanthanide levels. Importantly, once a lanthanide ion has acted as a donor for ET, it can no longer emit light (of the same color), and vice versa. In other words, ET and radiative decay are competing processes. The PL output of the phosphor is thus determined by the relative efficiencies of radiative decay and ET.

In co-doped phosphors, a high ET efficiency is often desired, so that the donor ion transfers all energy to acceptors that emit the desired color of light. In **Chapter 5**, we discussed YPO_4:Tb^{3+},Yb^{3+}, where the process of cooperative ET from visible-emitting Tb^{3+} to near-infrared-emitting Yb^{3+} determines the photoluminescence output. We demonstrated that the efficiency of energy transfer is reduced for donor ions close to the surface, which are coordinated by fewer acceptor ions. Interestingly, such finite-size effects can be counteracted by suppressing the competitive pathway of radiative decay of the donor ion, effectively increasing the probability of ET to the acceptor.

In **Chapter 6**, we discussed how electronic-to-vibrational energy transfer (EVET) quenches the luminescence from lanthanide-doped NCs. Mediated by EVET, the donor lanthanide ion

relaxes to a lower level, which affects the shape of the emission spectrum. EVET is efficient only in case the lanthanide donor couples efficiently to molecular vibrations, which requires proximity and resonance between the electronic donor transition and the energy of the vibrational mode. From the viewpoint of eliminating quenching processes to guarantee a high photoluminescence quantum yield, EVET is undesired and is often prevented by growing a shell around the NCs, which spatially isolates the lanthanide ions from molecular vibrations that act as EVET acceptors. We proposed instead that EVET may be exploited for the purpose of extracting information about the type of molecular vibrations in the local chemical environment of the NCs. Probing molecule-specific vibrations with lanthanide-doped NCs has great promise for applications in catalysis and biosensing, as an indirect method to locally track the diffusion, formation, or conversion of molecules.

Chapter 8

References

1. Talapin, D. V; Lee, J.; Kovalenko, M. V.; Shevchenko, E. V. Prospects of colloidal nanocrystals for electronic and optoelectronic applications. *Chem. Rev.* **2010**, *110*, 389–458

2. Meinardi, F.; Bruni, F.; Brovelli, S. Luminescent solar concentrators for building-integrated photovoltaics. *Nat. Reviews* 2017, 2, 17072

3. Talapin, D. V.; Steckel, J. Quantum dot light-emitting devices. *MRS Bull.* **2013**, 685–691

4. Bourzac, K. Quantum dots go on display. *Nature* **2013**, *493*, 283.

5. Jung, H.; Ahn, N.; Klimov, V. I. Prospects and challenges of colloidal quantum dot laser diodes. *Nat. Photonics* **2021**, *15*, 643–655

6. van de Haar, M. A.; Berends, A. C.; Krames, M. R.; Chepyga, L.; Rabouw, F. T.; Meijerink, A. Eu^{3+} Sensitization via nonradiative interparticle energy transfer using inorganic nanoparticles. *J. Phys. Chem. Lett*. **2020**, *11*, 689–695

7. van der Ende, B. M.; Aarts, L.; Meijerink, A. Lanthanide ions as spectral converters for solar cells. *Phys. Chem. Chem. Phys*. **2009**, *11*, 11081–11095

8. Fan, Y.; Zhang, F. A new generation of NIR-II probes: lanthanide-based nanocrystals for bioimaging and biosensing. *Adv. Opt. Mater*. **2019**, *7*, 1801417.

9. Li, H.; Wang, X. Ohulchanskyy, T. Y.; Chen, G. Lanthanide-doped near-infrared nanopaticles for biophotonics. *Adv. Mater*. **2021**, *33*, 2000678

10. Liu, Q.; Sun, Y.; Yang, T.; Feng, W.; Li, C.; Li, F. Sub-10 nm hexagonal lanthanide-doped $NaLuF_4$ upconversion nanocrystals for sensitive bioimaging in vivo. *J. Am. Chem. Soc*. **2011**, *133*, 17122–17125

11. Tu, D.; Liu, L.; Ju, Q.; Liu, Y.; Zhu, H.; Li, R.; Chen, X. Time-resolved FRET biosensor based on amine-functionalized lanthanide-doped $NaYF_4$ nanocrystals. *Angew. Chem. Int. Ed*. **2011**, *50*, 6306–6310.

12. Boyer, J. C.; Manseau, M. P.; Murray, J. I.; van Veggel, F. C. J. M. Surface modification of upconverting $NaYF_4$ nanoparticles with PEG-phosphate ligands for NIR (800 nm) biolabeling within the biological window. *Langmuir* **2010**, *26*, 1157–1164.

13. Ma, Q.; Wang, J.; Li, Z.; Lv, X.; Liang, L.; Yuan, Q. Recent progress in time-resolved biosensing and bioimaging based on lanthanide-doped nanoparticles. *Small*, **2019**, *15*, 1804969.

14. Hartman, T.; Geitenbeek, R. G.; Whiting, G. T.; Weckhuysen, B. M. Operando monitoring of temperature and active species at the single catalyst particle level. *Nat. Catal*. **2019**, *2*, 986–996.

15. van Swieten, T. P.; van Omme, T.; van den Heuvel, D. J.; Vonk, S. J. W.; Spruit, R. G.; Meirer, F.; Pérez Garza, H. H., Weckhuysen, B. M.; Meijerink, A.; Rabouw, F. T.; Geitenbeek, R. G. Mapping elevated temperatures with a micrometer resolution using the luminescence of chemically Stable upconversion Nanocrystals. *ACS Appl. Nano Mater*. **2021**, *4*, 4208–4215

16. Brus, L. E. A simple model for the ionization potential, electron affinity, and aqueous redox potentials of small semiconductor crystallites. *J. Chem. Phys.* **1983**, *79*, 5566–5571

17. Brus, L. E. Electron-electron and electron-hole interactions in small semiconductor crystallites: the size dependence of the lowest excited electronic state. *J. Chem. Phys*. **1984**, *80*, 4403–4409

18. Norris, D.J.; Bawendi, M.G. Measurement and assignment of the size-dependent optical spectrum in CdSe quantum dots. *Phys. Rev. B* **1996**, *53*, 16338

19. Ekimov, A. I.; Hache, F.; Schanne-Klein, M. C.; Ricard, D.; Flytzanis, C.; Kudryavtsev, I. A.; Yazeva, T. V.; Rodina, A. V.; Efros, Al. L. Absorption and intensity-dependent photoluminescence measurements on CdSe quantum dots: assignment of the first electronic transitions. *J. Opt. Soc. Am. B* **1993**, *10*, 100–107

20. Empedocles, S. A.; Bawendi, M. G. Quantum-confined Stark effect in single CdSe nanocrystallite quantum dots. *Science* **1997**, *278*, 2114–2117

21. Neuhauser, R. G.; Shimizu, K. T.; Woo, W. K.; Empedocles, S. A.; Bawendi, M. G. Correlation between fluorescence intermittency and spectral diffusion in single semiconductor quantum dots. *Phys. Rev. Lett.* **2000**, *85*, 3301

22. Rothenberg, E.; Kazes, M.; Shaviv, E.; Banin, U. Electric field induced switching of the fluorescence of single semiconductor quantum rods. *Nano Lett.* **2005**, *5*, 1581–1586

23. van de Haar, M. A.; Tachikirt, M.; Berends, A. C.; Krames, M. R.; Meijerink, A.; Rabouw, F. T. Saturation mechanisms in common LED phosphors. *ACS Photonics* **2021**, *8*, 1784–1793

24. Wang, F.; Deng, R.; Liu, X. Preparation of $NaGdF_4$ nanoparticles doped with luminescent lanthanide ions to be used as upconversion-based probes. *Nat. Protoc.* **2014**, *9*, 1634–1644

25. Peijzel, P. S.; Meijerink, A.; Wegh, R. T.; Reid, M. F.; Burdick, G. W. A complete $4f^n$ energy level diagram for all trivalent lanthanide ions. *J. Solid State Chem.* **2005**, *178*, 448–453

26. Dieke, G. *Spectra and energy levels of rare earth ions in crystals*.; Crosswhite, H. M., Crosswhite, H., Eds.; Wiley: New York, **1968**.

27. Carnall, W. T.; Crosswhite, H.; Crosswhite, H. M. *Energy levels structure and transition probabilities in the spectra of the trivalent lanthanides in* LaF_3. Argonne National Laboratory, **1977**.

28. Förster, T. Zwischenmolekulare Energiewanderung und Fluoreszenz. *Ann. Phys.* **1948**, *437*, 55–75

29. Auzel, F. Upconversion and anti-Stokes processes with f and d Ions in solids. *Chem. Rev.* **2004**, *104*, 139–174

30. Dexter, D. L. Possibility of luminescent quantum yields greater than unity. *Phys. Rev*. **1957**, *108*, 630–633

31. de Jong, M.; Meijerink, A.; Rabouw, F. T. Non-Poissonian photon statistics from macroscopic photon cutting materials. *Nat. Commun*. **2017**, *8*, 15537

32. Crane, M. J.; Kroupa, D. M.; Gamelin, D. R. Detailed-balance analysis of Yb^{3+}:$CsPb(Cl_{1-x}Br_x)_3$ quantum-cutting layers for high-efficiency photovoltaics under real-world conditions. *Energy Environ. Sci.* **2019**, *12*, 2486–2495

33. Trupke, T.; Green, M. A.; Würfel, P. Improving solar cell efficiencies by down-conversion of high-energy photons. *J. Appl. Phys.* **2002**, *92*, 1668–1674

34. Trupke, T.; Green, M. A.; Würfel, P. Improving solar cell efficiencies by up-conversion of sub-band-gap light. *J. Appl. Phys*. **2002**, *92*, 4117–4122

35. Talapin, D. V; Lee, J.; Kovalenko, M. V; Shevchenko, E. V. Prospects of colloidal nanocrystals for electronic and optoelectronic applications. *Chem. Rev*. **2010**, *110*, 389–458

36. Reiss, P.; Carrière, M.; Lincheneau, C.; Vaure, L.; Tamang, S. Synthesis of semiconductor nanocrystals, focusing on nontoxic and earth-abundant materials. *Chem. Rev*. **2016**, *116*, 10731–10819.

37. van der Stam, W.; Berends, A. C.; de Mello Donegá, C. Prospects of colloidal copper chalcogenide nanocrystals. *ChemPhysChem* **2016**, *17*, 559–581.

38. Meinardi, F.; McDaniel, H.; Carulli, F.; Colombo, A.; Velizhanin, K. A.; Makarov, N. S.; Simonutti, R.; Klimov, V. I.; Brovelli, S. Highly efficient large-area colourless luminescent solar concentrators using heavy-metal-free colloidal quantum dots. *Nat. Nanotechnol*. **2015**, *10*, 878–885.

39. Knowles, K. E.; Kilburn, T. B.; Alzate, D. G.; McDowall, S.; Gamelin, D. R. Bright $CuInS_2$/CdS nanocrystal phosphors for high-gain full-spectrum luminescent solar concentrators. *Chem. Commun*. **2015**, *51*, 9129–9132.

40. Bergren, M. R.; Makarov, N. S.; Ramasamy, K.; Jackson, A.; Guglielmetti, R.; McDaniel, H. High-performance $CuInS_2$ quantum dot laminated glass luminescent solar concentrators for windows. *ACS Energy Lett*. **2018**, *3*, 520–525.

41. Wu, K.; Li, H.; Klimov, V. I. Tandem luminescent solar concentrators based on engineered quantum dots. *Nat. Photonics* **2018**, *12*, 105–110.

42. Hu, X.; Kang, R.; Zhang, Y.; Deng, L.; Zhong, H.; Zou, B.; Shi, L.-J. Ray-trace simulation of $CuInS(Se)_2$ quantum dot based luminescent solar concentrators. *Opt. Express* **2015**, *23*, A858–A867.

43. Li, C.; Chen, W.; Wu, D.; Quan, D.; Zhou, Z.; Hao, J.; Qin, J.; Li, Y.; He, Z.; Wang, K. Large Stokes shift and high efficiency luminescent solar concentrator incorporated with $CuInS_2$/ZnS quantum dots. *Sci. Rep.* **2015**, *5*, 17777.

44. Sumner, R.; Eiselt, S.; Kilburn, T. B.; Erickson, C.; Carlson, B.; Gamelin, D. R.; McDowall, S.; Patrick, D. L. Analysis of optical losses in high-efficiency $CuInS_2$-based nanocrystal luminescent solar concentrators: Balancing Absorption versus Scattering. *J. Phys. Chem. C* **2017**, *121*, 3252–3260.

45. Berends, A. C.; Rabouw, F. T.; Spoor, F. C. M.; Bladt, E.; Grozema, F. C.; Houtepen, A. J.; Siebbeles, L. D. A.; de Mello Donegá, C. Radiative and nonradiative recombination in $CuInS_2$ nanocrystals and $CuInS_2$-based core/shell nanocrystals. *J. Phys. Chem. Lett.* **2016**, *7*, 3503–3509.

46. Rabouw, F. T.; de Mello Donega, C. Excited-state dynamics in colloidal semiconductor nanocrystals. *Top. Curr. Chem.* **2016**, *374*, 58.

47. Seo, J.; Raut, S.; Abdel-Fattah, M.; Rice, Q.; Tabibi, B.; Rich, R.; Fudala, R.; Gryczynski, I.; Gryczynski, Z.; Kim, W.-J.; Jung, S.; Hyun, R. Time-resolved and temperature-dependent photoluminescence of ternary and quaternary nanocrystals of $CuInS_2$ with ZnS capping and cation exchange. *J. Appl. Phys.* **2013**, *114*, 094310.

48. Chen, B.; Zhong, H.; Zhang, W.; Tan, Z.; Li, Y.; Yu, C.; Zhai, T.; Bando, Y.; Yang, S.; Zou, B. Highly emissive and color-tunable $CuInS_2$-based colloidal semiconductor nanocrystals: off-stoichiometry effects and improved electroluminescence Performance. *Adv. Funct. Mater.* **2012**, *22*, 2081–2088.

49. Shabaev, A.; Mehl, M. J.; Efros, A. L. Energy band structure of $CuInS_2$ and optical spectra of $CuInS_2$ nanocrystals. *Phys. Rev. B* **2015**, *92*, 035431.

50. Omata, T.; Nose, K.; Kurimoto, K.; Kita, M. Electronic transition responsible for size-dependent photoluminescence of colloidal $CuInS_2$ quantum dots. *J. Mater. Chem. C* **2014**, *2*, 6867–6872.

51. Kraatz, I. T.; Booth, M.; Whitaker, B. J.; Nix, M. G. D.; Critchley, K. Sub-bandgap emission and intraband defect-related excited-state dynamics in colloidal $CuInS_2$/ZnS quantum dots revealed by femtosecond pump-dump-probe spectroscopy. *J. Phys. Chem. C* **2014**, *118*, 24102–24109.

52. Leach, A. D. P.; Macdonald, J. E. Optoelectronic properties of $CuInS_2$ nanocrystals and their origin. *J. Phys. Chem. Lett.* **2016**, *7*, 572–583.

53. Li, L.; Pandey, A.; Werder, D. J.; Khanal, B. P.; Pietryga, J. M.; Klimov, V. I. Efficient synthesis of highly luminescent copper indium sulfide-based core/shell nanocrystals with surprisingly long-lived emission. *J. Am. Chem. Soc.* **2011**, *133*, 1176–1179.

54. Sun, J.; Zhu, D.; Zhao, J.; Ikezawa, M.; Wang, X.; Masumoto, Y. Ultrafast carrier dynamics in $CuInS_2$ quantum dots. *Appl. Phys. Lett.* **2014**, *104*, 023118.

55. Knowles, K. E.; Nelson, H. D.; Kilburn, T. B.; Gamelin, D. R. Singlet-triplet splittings in the luminescent excited states of colloidal Cu^+:CdSe, Cu^+:InP, and $CuInS_2$ nanocrystals: charge-transfer configurations and self-trapped excitons. *J. Am. Chem. Soc.* **2015**, *137*, 13138–13147.

56. Berends, A. C.; Rabouw, F. T.; Spoor, F. C. M.; Bladt, E.; Grozema, F. C.; Houtepen, A. J.; Siebbeles, L. D. A.; de Mello Donegá, C. Radiative and nonradiative recombination in $CuInS_2$ nanocrystals and $CuInS_2$-based core/shell nanocrystals. *J. Phys. Chem. Lett.* **2016**, *7*, 3503–3509.

57. Whitham, P. J.; Marchioro, A.; Knowles, K. E.; Kilburn, T. B.; Reid, P. J.; Gamelin, D. R. Single-particle photoluminescence spectra, blinking, and delayed luminescence of colloidal $CuInS_2$ nanocrystals. *J. Phys. Chem. C* **2016**, *120*, 17136–17142.

58. Nagamine, G.; Nunciaroni, H. B.; McDaniel, H.; Efros, A. L.; De Brito Cruz, C. H.; Padilha, L. A. Evidence of band-edge hole levels inversion in spherical $CuInS_2$ quantum dots. *Nano Lett.* **2018**, *18*, 6353–6359.

59. Nelson, H. D.; Gamelin, D. R. Valence-band electronic structures of Cu^+-doped ZnS, alloyed Cu-In-Zn-S, and ternary $CuInS_2$ nanocrystals: a unified description of photoluminescence across compositions. *J. Phys. Chem. C* **2018**, *122*, 18124–18133.

60. Zang, H.; Li, H.; Makarov, N. S.; Velizhanin, K. A.; Wu, K.; Park, Y.-S.; Klimov, V. I. Thick-shell $CuInS_2$/ZnS quantum dots with suppressed "blinking" and narrow single-particle emission line widths. *Nano Lett.* **2017**, *17*, 1787–1795.

61. Fuhr, A.; Yun, H. J.; Crooker, S. A.; Klimov, V. I. Spectroscopic and magneto-optical signatures of Cu^{1+} and Cu^{2+} defects in copper indium sulfide quantum dots. *ACS Nano* **2020**, *14*, 2212–2223.

62. Hu, W.; Ludwig, J.; Pattengale, B.; Yang, S.; Liu, C.; Zuo, X.; Zhang, X.; Huang, J. Unravelling the correlation of electronic structure and carrier dynamics in $CuInS_2$ nanoparticles. *J. Phys. Chem. C* **2018**, *122*, 974–980.

63. Fuhr, A. S.; Yun, H. J.; Makarov, N. S.; Li, H.; McDaniel, H.; Klimov, V. I. Light emission mechanisms in $CuInS_2$ quantum dots evaluated by spectral electrochemistry. *ACS Photonics* **2017**, *4*, 2425–2435.

64. van der Stam, W.; De Graaf, M.; Gudjonsdottir, S.; Geuchies, J. J.; Dijkema, J. J.; Kirkwood, N.; Evers, W. H.; Longo, A.; Houtepen, A. J. Tuning and probing the distribution of Cu^{+} and Cu^{2+} trap states responsible for broad-band photoluminescence in $CuInS_2$ nanocrystals. *ACS Nano* **2018**, *12*, 11244–11253.

65. Pinchetti, V.; Lorenzon, M.; McDaniel, H.; Lorenzi, R.; Meinardi, F.; Klimov, V. I.; Brovelli, S. Spectro-electrochemical probing of intrinsic and extrinsic processes in exciton recombination in I-III-VI_2 nanocrystals. *Nano Lett.* **2017**, *17*, 4508–4517.

66. Debnath, T.; Ghosh, H. N. Ternary metal chalcogenides: into the exciton and biexciton dynamics. *J. Phys. Chem. Lett.* **2019**, *10*, 6227–6238.

67. Anand, A.; Zaffalon, M. L.; Gariano, G.; Camellini, A.; Gandini, M.; Brescia, R.; Capitani, C.; Bruni, F.; Pinchetti, V.; Zavelani-Rossi, M.; Meinardi, F.; Crooker, S. A.; Brovelli, S. Evidence for the band-edge exciton of $CuInS_2$ nanocrystals enables record efficient large-area luminescent solar concentrators. *Adv. Funct. Mater.* **2020**, *30*, 1906629

68. Knowles, K. E.; Hartstein, K. H.; Kilburn, T. B.; Marchioro, A.; Nelson, H. D.; Whitham, P. J.; Gamelin, D. R. Luminescent colloidal semiconductor nanocrystals containing copper: synthesis, photophysics, and applications. *Chem. Rev.* **2016**, *116*, 10820–10851.

69. Schwartz, O.; Tenne, R.; Levitt, J. M.; Deutsch, Z.; Itzhakov, S.; Oron, D. Colloidal quantum dots as saturable fluorophores. *ACS Nano* **2012**, *6*, 8778–8782.

70. Galland, C.; Ghosh, Y.; Steinbrück, A.; Sykora, M.; Hollingsworth, J. A.; Klimov, V. I.; Htoon, H. Two types of luminescence blinking revealed by spectroelectrochemistry of single quantum dots. *Nature* **2011**, *479*, 203–207.

71. Becker, M. A.; Vaxenburg, R.; Nedelcu, G.; Sercel, P. C.; Shabaev, A.; Mehl, M. J.; Michopoulos, J. G.; Lambrakos, S. G.; Bernstein, N.; Lyons, J. L.; Stöferle, T.; Mahrt, R. F.; Kovalenko, M. V.; Norris, D. J.; Rainò, G.; Efros, A. L. Bright triplet excitons in caesium lead halide perovskites. *Nature* **2018**, *553*, 189–193.

72. Tamarat, P.; Bodnarchuk, M. I.; Trebbia, J. B.; Erni, R.; Kovalenko, M. V.; Even, J.; Lounis, B. The ground exciton state of formamidinium lead bromide perovskite nanocrystals is a singlet dark state. *Nat. Mater.* **2019**, *18*, 717–724.

73. Zhang, A.; Dong, C.; Li, L.; Yin, J.; Liu, H.; Huang, X.; Ren, J. Non-blinking (Zn)CuInS/ZnS quantum dots prepared by in situ interfacial alloying approach. *Sci. Rep.* **2015**, *5*, 15227.

74. Nguyen, A. T.; Gao, F.; Baucom, D.; Heyes, C. D. $CuInS_2$-doped ZnS quantum dots obtained via non-injection cation exchange show reduced but heterogeneous blinking and provide insights into their structure-optical property relationships. *J. Phys. Chem. C* **2020**, *124*, 10744–10754.

75. Berends, A. C.; van der Stam, W.; Hofmann, J. P.; Bladt, E.; Meeldijk, J. D.; Bals, S.; de Mello Donega, C. Interplay between Surface Chemistry, Precursor reactivity, and temperature determines outcome of ZnS shelling reactions on $CuInS_2$ nanocrystals. *Chem. Mater.* **2018**, *30*, 2400–2413.

76. Shannon, R. D. Revised effective ionic radii and systematic studies of interatomic distances. *Acta Cryst.* **1976**, *32*, 751–767.

77. Hinterding, S.O.M.; Mangnus, M.J.J.; Prins, P.T.; Jöbsis, H.J.; Busatto, S.; Vanmaekelbergh, D.; de Mello Donega, C.; Rabouw, F.T. Unusual spectral diffusion of single $CuInS_2$ quantum dots sheds light on the mechanism of radiative decay. *Nano Lett.* **2021**, *21*, 658–665

78. Xia, C.; Wu, W.; Yu, T.; Xie, X.; van Oversteeg, C.; Gerritsen, H. C.; De Mello Donega, C. Size-dependent band-gap and molar absorption coefficients of colloidal $CuInS_2$ quantum dots. *ACS Nano* **2018**, *12*, 8350–8361.

79. Ihara, T.; Kanemitsu, Y. Spectral diffusion of neutral and charged exciton transitions in single CdSe/ZnS nanocrystals due to quantum-confined Stark effect. *Phys. Rev. B* **2014**, *90*, 195302.

80. Hinterding, S. O. M.; Vonk, S. J. W.; van Harten, E. J.; Rabouw, F. T. Dynamics of intermittent delayed emission in single CdSe/CdS quantum dots. *J. Phys. Chem. Lett.* **2020**, *11*, 4755–4761.

81. Nelson, H. D.; Li, X.; Gamelin, D. R. Computational studies of the electronic structures of copper-doped CdSe nanocrystals: oxidation states, Jahn–Teller distortions, vibronic bandshapes, and singlet–triplet splittings. *J. Phys. Chem. C* **2016**, *120*, 5714–5723.

82. Müller, J.; Lupton, J. M.; Rogach, A. L.; Feldmann, J.; Talapin, D. V.; Weller, H. Monitoring surface charge migration in the spectral dynamics of single CdSe CdS nanodot/nanorod heterostructures. *Phys. Rev. B* **2005**, *72*, 205339.

83. Empedocles, S. A.; Bawendi, M. G.; Quantum-confined Stark effect in single CdSe Nanocrystallite quantum dots. *Science* **1997**, *278*, 2114–2117

84. Park, K.; Deutsch, Z.; Li, J. J.; Oron, D.; Weiss, S. Single molecule quantum-confined Stark effect measurements of semiconductor nanoparticles at room temperature. *ACS Nano* **2012**, *6*, 10013–10023

85. Janke, E. M.; Williams, N. E.; She, C.; Zherebetskyy, D.; Hudson, M. H.; Wang, L.; Gosztola, D. J.; Schaller, R. D.; Lee, B.; Sun, C.; Engel, G. S.; Talapin, D. V. Origin of broad emission spectra in InP quantum dots: contributions from structural and electronic disorder. *J. Am. Chem. Soc.* **2018**, *140*, 15791–15803

86. Efros, A. L.; Brus, L. E. Nanocrystal quantum dots: from discovery to modern development. *ACS Nano* **2021**, *15*, 6192–6210

87. Shirasaki, Y.; Supran, G.J.; Bawendi, M.G.; Bulovic, V.; Emergence of colloidal quantum-dot light-emitting technologies. *Nat. Photonics* **2013**, *7*, 12–23

88. Liu, Z.; Lin, C.-H.; Hyun, B.-R.; Sher, C.-W.; Lv, Z.; Luo, B.; Jiang, F.; Wu, T.; Ho, C.-H.; Kuo, H.-C.; He, J.-H. Micro-light-emitting diodes with quantum dots in display technology. *Light Sci. Appl.* **2020**, *9*, 83

89. Liu, X.; Braun, G. B.; Zhong, H.; Hall, D. J.; Han, W.; Qin, M.; Zhao, C.; Wang, M.; She, Z.-G.; Cao, C.; Sailor, M. J.; Stallcup, W. B.; Ruoslahti, E.; Sugahara, K. N. Tumor-targeted multimodal optical imaging with versatile cadmiun-free quantum dots. *Adv. Funct. Mater.* **2016**, *26*, 267–276

90. Kovalenko, M. V. Opportunities and challenges for quantum dot photovoltaics. *Nat. Nanotechnol.* **2015**, *10*, 994–997

91. Qiu, F.; Han, Z.; Peterson, J.J.; Odoi, M.Y.; Sowers, K.L.; Krauss, T.D. Photocatalytic hydrogen generation by CdSe/CdS nanoparticles. *Nano Lett.* **2016**, *16*, 5347–5352

92. Cohen, T. A.; Milstein, T. J.; Kroupa, D. M.; MacKenzie, J.D.; Luscombe, C. K.; Gamelin, D. R. Quantum-cutting Yb^{3+}-doped perovskite nanocrystals for monolithic bilayer luminescent solar concentrators. *J. Mater. Chem. A* **2019**, *7*, 9279–9288

93. Protesescu, L.; Yakunin, S.; Bodnarchuk, M. I.; Krieg, F.; Caputo, R.; Hendon, C. H.; Yang, R. X.; Walsh, A.; Kovalenko, M. V. Nanocrystals of cesium lead halide perovskites ($CsPbX_3$, X = Cl, Br, and I): novel optoelectronic materials showing bright emission with wide color gamut. *Nano Lett.* **2015**, *15*, 3692–3696

94. Ebenstein, Y.; Mokari, T.; Banin, U. Fluorescence quantum yield of CdSe/ZnS nanocrystals investigated by correlated atomic-force and single-particle fluorescence microscopy. *Appl. Phys. Lett.* **2002**, *80*, 4033

95. Nirmal, M.; Dabbousi, B. O.; Bawendi, M. G.; Macklin, J. J.; Trautman, J. L.; Harris, T. D.; Brus, L. E. Fluorescence intermittency in single cadmium selenide nanocrystals. *Nature* **1996**, *383*, 802–804

96. Blanton, S. A.; Hines, M. A.; Guyot-Sionnest, P. Photoluminescence wandering in single CdSe nanocrystals. *Appl. Phys. Lett.* **1996**, *69*, 3905–3907

97. Empedocles, S. A.; Bawendi, M. G. Influence of spectral diffusion on the line shapes of single CdSe nanocrystallite quantum dots. *J. Phys. Chem. B* **1999**, *103*, 1826–1830

98. Frantsuzov, P. A.; Marcus, R. A. Explanation of quantum dot blinking without the long-lived trap hypothesis. *Phys. Rev. B* **2005**, *72*, 155321

99. Gómez, D. E.; van Embden, J.; Mulvaney, P. Spectral diffusion of single semiconductor nanocrystals: the influence of the dielectric environment. *Appl. Phys.Lett.* **2006**, *88*, 154106

100. Plakhotnik, T.; Fernée, M.J.; Littleton, B.; Rubinsztein-Dunlop, H.; Potzner, C.; Mulvaney, P. Anomalous power laws of spectral diffusion in quantum dots: a connection to luminescence intermittency. *Phys. Rev. Lett.* **2010**, *105*, 167402

101. Voznyy, O. Mobile surface traps in CdSe nanocrystals with carboxylic acid ligands. *J. Phys. Chem. C* **2011**, *115*, 15927–15932

102. Fernée, M. J.; Plakhotnik, T.; Louyer, Y.; Littleton, B. N.; Potzner, C.; Tamarat, P.; Mulvaney, P.; Lounis, B. Spontaneous spectral diffusion in CdSe quantum dots. *J. Phys. Chem. Lett.* **2012**, *3*, 1716–1720

103. Efros, A. L.; Nesbitt, D. J. Origin and control of blinking in quantum dots. *Nat. Nanotechnol.* **2016**, *11*, 661–671. 6210

104. Mahler, B.; Spinicelli, P. ; Buil, S.; Quelin, X. ; Hermier, J.-P. ; Dubertret, B. Towards non-blinking colloidal quantum dots. *Nat. Mater.* **2008**, *7*, 659–664

105. Chen, O.; Zhao, J.; Chauhan, V. P.; Cui, J.; Wong, C.; Harris, D. K.; Wei, H.; Han, H.-S.; Fukumura, D.; Jain, R. K.; Bawendi, M. G. Compact high-quality CdSe-CdS core-shell nanocrystals with narrow emission linewidths and suppressed blinking. *Nat. Mater.* **2013**, *12*, 448–451

106. Park, Y.-S.; Lim, J.; Klimov, V. I. Asymmetrically strained quantum dots with non-fluctuating single-dot emission spectra and subthermal room-temperature linewidths. *Nat. Mater.* **2019**, *18*, 249–255

107. Reid, K. R.; McBride, J. R.; Freymeyer, N. J.; Thal, L. B.; Rosenthal, S. J. Chemical structure, ensemble and single-particle spectroscopy of thick-shell InP–ZnSe quantum dots. *Nano Lett.* **2018**, *18*, 709–716

108. Chandrasekaran, V.; Tessier, M. D.; Dupont, D. ; Geiregat, P.; Hens, Z.; Brainis, E. Nearly blinking-free, high-purity single-photon emission by colloidal InP/ZnSe quantum dots. *Nano Lett.* **2017**, *17*, 6104–6109

109. Kim, T.; Won, Y.-H.; Jang, E.; Kim, D. Negative trion Auger recombination in highly luminescent InP/ZnSe/ZnS quantum dots. *Nano Lett.* **2021**, *21*, 2111–2116

110. Lee, Y.; Jo, D.-Y.; Kim, T.; Jo, J.-H.; Park, J.; Yang, H.; Kim, D. Effectual interface and defect engineering for Auger recombination suppression in bright InP/ZnSeS/ZnS quantum dots. *ACS Appl. Mater. Interfaces* **2022**, *14*, 12479–12487

111. Won, Y.-H.; Cho, O.; Kim, T.; Chung, D.-Y.; Kim, T.; Chung, H.; Jang, H.; Lee, J.; Kim, D.; Jang, E. Highly efficient and stable InP/ZnSe/ZnS quantum dot light-emitting diodes. *Nature* **2019**, *575*, 634–638

112. van Avermaet, H.; Schiettecatte, P.; Hinz, S.; Giordano, L.; Ferrati, F.; Nayral, C.; Delpech, F.; Maultzsch, J.; Lange, H.; Hens, Z. Full-spectrum InP-based quantum dots with near-unity photoluminescence quantum efficiency. *ACS Nano* **2022**, *16*, 9701–9712

113. Sousa Velosa, F.; van Avermaet, H.; Schiettecatte, P.; Mingabudinova, L.; Geiregat, P.; Hens, Z. State filling and stimulated emission by colloidal InP/ZnSe core/shell quantum dots. *Adv. Opt. Mater.* **2022**, *10*, 2200328

114. Berkinsky, D. B.; Proppe, A. H.; Utzat, H.; Krajewska, C. J.; Sun, W.; Sverko, T.; Yoo, J. J.; Chung, H.; Won, Y.-H.; Kim, T.; Jang, E.; Bawendi, M. G. Narrow intrinsic line widths and electron–phonon coupling of InP quantum dots. *ACS Nano* **2023**, *17*, 3598–3609

115. Jeong, B. G.; Chang, J. H.; Hahm, D.; Rhee, S.; Park, M.; Lee, S.; Kim, Y.; Shin, D.; Park, J. W.; Lee, C.; Lee, D. C.; Park, K.; Hwang, E.; Bae, W. K. Interface polarization in heterovalent core–shell nanocrystals. *Nat. Mater.* **2022**, *21*, 246–252

116. Hughes, K. E.; Stein, J. L.; Friedfeld, M. R.; Cossairt, B. M.; Gamelin, D. R. Effects of surface chemistry on the photophysics of colloidal InP nanocrystals. *ACS Nano* **2019**, *13*, 14198–14207

117. Nguyen, A. T.; Jen-La Plante, I.; Ippen, C.; Ma, R.; Kelley, D. F. Extremely slow trap-mediated hole relaxation in room-temperature InP/ZnSe/ZnS quantum dots. *J. Phys. Chem. C* **2021**, *125*, 4110–4118

118. Kelley, A. M.; Cavanaugh, P.; Sun, H.; Wang, X. Bautista, M. J.; Jen-La Plante, I.; Ippen, C.; Kelley, D. F. Identity of the reversible hole traps in InP/ZnSe core/shell quantum dots. *J. Chem. Phys.* **2022**, *157*, 174701.

119. Cui, J.; Beyler, A. P. ; Marshall, L. F.; Chen, O.; Harris, D. K.; Wanger, D. D.; Brokmann, X.; Bawendi, M. G. Direct probe of spectral inhomogeneity reveals synthetic tunability of single-nanocrystal linewidths. *Nat. Chem.* **2013**, *5*, 602–606

120. Beyler, A. P.; Bischof, T. S.; Cui, J.; Coropceanu, I.; Harris, D. K.; Bawendi, M. G. Sample-averaged biexciton quantum yield measured by solution-phase photon correlation. *Nano Lett.* **2014**, *14*, 6792–6798

121. Marchioro, A.; Whitham, P. J.; Knowles, K. E.; Kilburn, T. B.; Reid, P. J.; Gamelin, D. R. Tunneling in the delayed luminescence of colloidal CdSe, Cu^{+}-doped CdSe, and $CuInS_2$ semiconductor nanocrystals and relationship to blinking. *J. Phys. Chem. C* **2016**, *120*, 27040–27049

122. Utzat, H.; Schulenberger, K. E.; Achorn, O. B.; Nasilowski, M.; Sinclair, T. S.; Bawendi, M. G. Probing linewidths and biexciton quantum yields of single cesium lead halide nanocrystals in solution. *Nano Lett.* **2017**, *17*, 6838–6846

123. Empedocles, S. A.; Norris, D. J.; Bawendi, M. G. Photoluminescence spectroscopy of single CdSe nanocrystallite quantum dots. *Phys. Rev. Lett*. **1996**, *77*, 3873

124. Houel, J.; Doan, Q. T.; Cajgfinger, T.; Ledoux, G.; Amans, D.; Aubret, A.; Dominjon, A.; Ferriol, S.; Barbier, R.; Nasilowski, M.; Lhuillier, E.; Dubertret, B.; Dujardin, C.; Kulzer, F. Autocorrelation analysis for the unbiased determination of power-law exponents in single-quantum-dot blinking. *ACS Nano* **2015**, *9*, 886–893

125. Howell, S. B. *Handbook of CCD Astronomy*, 2nd ed.; Cambridge University Press, **2006**; pp 157–165

126. Zhang, Z.; Kenny, S.; Hauser, M.; Li, W.; Xu, K. Ultrahigh-throughput single-molecule spectroscopy and spectrally resolved super-resolution microscopy. *Nat. Methods* **2015**, *12*, 935–938

127. Martens, K. J. A.; Gobes, M.; Archontakis, E.; Brillas, R. R.; Zijlstra, N.; Albertazzi, L.; Hohlbein, J. Enabling spectrally resolved single-molecule localization at high emitter densities. *Nano Lett*. **2022**, *22*, 8618–8625

128. Brokmann, X. Bawendi, M. G.; Coolen, L.; Hermier, J.-P. Photon-correlation spectroscopy. *Opt. Express* **2006**, *14*, 6333–6341

129. Marshall, L. F.; Cui, J.; Brokmann, X.; Bawendi, M. G. Extracting spectral dynamics from single chromophores in solution. P*hys. Rev. Lett*. **2010**, *105*, 053005

130. Vonk, S. J. W.; Heemskerk, B. A. J.; Keitel, R. C.; Hinterding, S. O. M.; Geuchies, J. J.; Houtepen, A. J.; Rabouw, F. T. Biexciton binding energy and line width of single quantum dots at room temperature. *Nano Lett*. **2021**, *21*, 5760–5766

131. Brodu, A.; Ballottin, M. V.; Buhot, J.; van Harten, E. J.; Dupont, D.; La Porta, A.; Prins, P. T.; Tessier, M. D.; Versteegh, M. A. M.; Zwiller, V.; Bals, S.; Hens, Z.; Rabouw, F. T.; Christianen, P. C. M.; de Mello Donega, C.; Vanmaekelbergh, D. Exciton fine structure and lattice dynamics in InP/ZnSe core/shell quantum dots. *ACS Photonics*. **2018**, *5*, 3353–3362

132. Beyler, A. P.; Marshall, L. F.; Cui, J.; Brokmann, X.; Bawendi, M. G. Direct observation of rapid discrete spectral dynamics in single colloidal CdSe-CdS core-shell quantum dots. *Phys. Rev. Lett.* **2013**, *111*, 177401

133. Neuhauser, R. G.; Shimizu, K. T.; Woo, W. K.; Empedocles, S. A.; Bawendi, M. G. Correlation between fluorescence intermittency and spectral diffusion in single semiconductor quantum dots. *Phys. Rev. Lett.* **2000**, *85*, 3301

134. Brichkin, S. B.; Spirin, M. G.; Tovstun, S. A.; Gak, V. Y.; Mart'yanova E. G.; Razumov, V. F. Colloidal quantum dots InP@ZnS: inhomogeneous broadening and distribution of luminescence lifetimes. *High Energy Chem.* **2016**, *50*, 395–399

135. De, C. K.; Routh, T.; Roy, D.; Mandal, S.; Mandal, P. K. Highly photoluminescent InP based core alloy shell QDs from air-stable precursors: excitation wavelength dependent photoluminescence quantum yield, photoluminescence decay dynamics, and single particle blinking dynamics. *J. Phys. Chem. C* **2018**, *122*, 964–973

136. Tessier, M. D.; Dupont, D.; De Nolf, K.; De Roo, J. ; Hens, Z. Economic and size-tunable synthesis of InP/ZnE (E = S, Se) colloidal quantum dots. *Chem. Mater.* **2015**, *27*, 4893–4898

137. Loiudice, A.; Lecina, O. S.; Bornet, A.; Luther, J.M. ; Buonsanti, R. Ligand locking on quantum dot surfaces via a mild reactive surface treatment. *J. Am. Chem. Soc.* **2021**, *143*, 13418–13427

138. Chen. X.; Nazzal, A.; Goorskey, D.; Xiao, M.; Peng, Z.A.; Peng, X. Polarization spectroscopy of single CdSe quatum rods. *Phys. Rev. B* **2001**, *64*, 245304

139. van Sark, W. G. J. H. M.; Frederix, P. L. T. M.; Bol, A. A.; Gerritsen, H. C.; Meijerink, A. Blueing, bleaching, and blinking of single CdSe/ZnSe quantum dots. *ChemPhysChem* **2002**, *3*, 871–879.

140. Inokuti, M.; Hirayama, F. Influence of energy transfer by the exchange mechanism on donor luminescence. *J. Chem. Phys.* **1965**, *43*, 1978–1989

141. Yokota, M.; Tanimoto, O. Effects of diffusion on energy transfer by resonance. *J. Phys. Soc. Jpn.* **1967**, *22*, 779–784

142. Vergeer, P.; Vlugt, T. J. H.; Kox, M. H. F.; den Hertog, M. I.; van der Eerden, J. P. J. M.; Meijerink, A. Quantum cutting by cooperative energy transfer in $Yb_xY_{1-x}PO_4:Tb^{3+}$. *Phys. Rev. B* **2005**, *71*, 014119

143. van Wijngaarden, J. T.; Scheidelaar, S.; Vlugt, T. J. H.; Reid, M. F.; Meijerink, A. Energy transfer mechanism for downconversion in the (Pr^{3+}, Yb^{3+}) couple. *Phys. Rev. B* **2010**, *81*, 155112

144. Yu, D. C.; Rabouw, F. T.; Boon, W. Q.; Kieboom, T., Ye S.; Zhang, Q. Y.; Meijerink, A. Insights into the energy transfer mechanism in Ce^{3+}-Yb^{3+} codoped YAG phosphors. *Phys. Rev. B* **2014**, *90*, 165126

145. Brites, C. D. S.; Lima, P. P.; Silva, N. J. O.; Millán, A., Amaral, V. S., Palacio, F., Carlos, L. D. Thermometry at the nanoscale. *Nanoscale* **2012**, *4*, 4799–4829

146. Jaque, D.; Vetrone, F. Luminescence nanothermometry. *Nanoscale* **2012**, *4*, 4301–4326

147. Zhou, B.; Shi, B.; Jin, D.; Liu, X. Controlling upconversion nanocrystals for emerging applications. *Nat. Nanotechnol.* **2015**, *10*, 924–936

148. Wang, F.; Wang, J.; Liu, X. Direct evidence of a surface quenching effect on size-dependent luminescence of upconversion nanoparticles. *Angew. Chem. Int. Ed*. **2010**, *49*, 7456–7460.

149. Zhao, J.; Lu, Z.; Yin, Y.; McRae, C.; Piper, J. A.; Dawes, J. M.; Jin, D.; Goldys, E. M. Upconversion luminescence with tunable lifetime in $NaYF_4$:Yb,Er nanocrystals: role of nanocrystal size. *Nanoscale* **2013**, *5*, 944–952

150. Stouwdam, J. W.; Hebbink, G. A.; Huskens, J.; Veggel, F. C. J. M. Lanthanide-doped nanoparticles with excellent luminescent properties in organic media. *Chem. Mater.* **2003**, *15*, 4604–4616

151. Gargas, D. J.; Chan, E. M.; Ostrowski, A. D.; Aloni, S.; Altoe, M. V. P.; Barnard, E. S.; Sanii, B.; Urban, J. J.; Milliron, D. J.; Cohen, B. E.; Schuck, P. J. Engineering bright sub-10-nm upconverting nanocrystals for single-molecule imaging. *Nat. Nanotechnol*. **2014**, *9*, 300–305

152. Fischer, S.; Johnson, N. J. J.; Pichaandi, J.; Goldschmidt, J. C.; van Veggel, F. C. J. M. Upconverting core-shell nanocrystals with high quantum yield under low irradiance: on the role of isotropic and thick shells. *J. Appl. Phys.* **2015**, *118*, 193105

153. Fischer, S.; Bronstein, N. D.; Swabeck, J. K.; Chan, E. M.; Alivisatos, A. P. Precise tuning of surface quenching for luminescence enhancement in core–shell lanthanide-doped nanocrystals. *Nano Lett.* **2016**, *16*, 7241–7247

154. Rabouw, F. T.; Prins, P. T.; Villaneuva-Delgado, P.; Castelijns, M.; Geitenbeek, R. G.; Meijerink, A. Quenching pathways in $NaYF_4$:Er^{3+},Yb^{3+} upconversion nanocrystals. *ACS Nano* **2018**, *12*, 4812–4823

155. Homann, C.; Krukewitt, L.; Frenzel, F.; Grauel, B.; Würth, C.; Resch-Genger, U.; Haase, M. $NaYF_4$:Yb,Er/$NaYF_4$ core/shell nanocrystals with high upconversion luminescence quantum yield. *Angew. Chem. Int. Ed.* **2018**, *57*, 8765–8769

156. Rabouw, F. T.; den Hartog, S. A.; Senden, T.; Meijerink, A. Photonic effects on the Förster resonance energy transfer efficiency. *Nat. Commun*. **2014**, *5*, 3610

157. Senden, T.; Rabouw, F. T.; Meijerink, A. Photonic effects on the radiative decay rate and luminescence quantum yield of doped nanocrystals. *ACS Nano* **2015**, *9*, 1801–1808

158. Oertel, A.; Lengler, C.; Walther, T.; Haase, M. Photonic properties of inverse opals fabricated from lanthanide-doped $LaPO_4$ nanocrystals. *Chem. Mater*. **2009**, *21*, 3883–3888

159. Guan, H.; Lv, C.; Han, C.; Zhu, D. Luminescent and magnetism properties of YPO_4:Eu^{3+} octahedron microcrystals. *Mater. Lett*. **2012**, *81*, 92–94

160. Shao, B.; Feng, Y.; Zhao, S.; Yuan, S.; Huo, J.; Lü, W.; You, H. Phase-tunable synthesis of monodisperse YPO_4:Ln^{3+} (Ln = Ce, Eu, Tb) micro/nanocrystals via topotactic transformation route with multicolor luminescence properties. *Inorg. Chem*. **2017**, *56*, 6114–6121

161. Rabouw, F. T.; Meijerink, A. Modeling the cooperative energy transfer dynamics of quantum cutting for solar cells. J. *Phys. Chem. C* **2015**, *119*, 2364–2370

162. Siebold, H.; Heber, J., "Discrete shell model" for analysing time-resolved energy transfer in solids, *J. Lumin.* **1981**, *22*, 297–319

163. Milligan, W. O.; Mullica, D. F.; Beall, G. W.; Boatner, L. A. Structural investigations of YPO_4, $ScPO_4$, and $LuPO_4$. *Inorg. Chim. Acta* **1982**, *60*, 39–43

164. Ni, Y.; Hughes, J. M.; Mariano, A. N. Crystal chemistry of the monazite and xenotime structures. *Am. Mineral.* **1995**, *80*, 21–26

165. Meltzer, R. S.; Feofilov, S. P.; Tissue, B.; Yuan, H. B. Dependence of fluorescence lifetimes of Y_2O_3:Eu^{3+} nanoparticles on the surrounding medium. *Phys. Rev. B* **1999**, *60*, R14012–R14015

166. Kozma, I. Z.; Krok, P.; Riedle, E. Direct measurement of the group-velocity mismatch and derivation of the refractive-index dispersion for a variety of solvents in the ultraviolet. *J. Opt. Soc. Am. B* **2005**, *22*, 1479–1485

167. Kedenburg, S.; Vieweg, M.; Gissibl, T.; Giessen, H. Linear refractive index and absorption measurements of nonlinear optical liquids in the visible and near-infrared spectral region. *Opt. Mater. Express* **2012**, *2*, 1588–1611

168. Jellison, G. E.; Boatner, L. A.; Chen, C. Spectroscopic refractive indices of metalorthophosphates with the zircon-type structure. *Opt. Mater.* **2000**, *15*, 103–109

169. Toptygin, D. Effects of the solvent refractive index and its dispersion on the radiative decay rate and extinction coefficient of a fluorescent solute. *J. Fluoresc.* **2003**, *13*, 201–219

170. Malta, O. L. Mechanisms of non-radiative energy transfer involving lanthanide ions revisited. *J. Non-Cryst. Solids.* **2008**, *354*, 4770–4776

171. Wyckoff, R. W. G. Fluorite structure. *In Crystal Structures 1*; 2nd ed., Interscience Publishers: New York, **1963**, pp 239–444

172. Villanueva-Delgado, P.; Krämer, K. W.; Valiente, R. Simulating energy transfer and upconversion in *β*-$NaYF_4$: Yb^{3+}, Tm^{3+}. *J. Phys. Chem. C* **2015**, *119*, 23648–23657

173. Aebischer, A; Hostettler, M; Hauser, J.; Krämer, K.; Weber, T.; Güdel, H. U.; Bürgi, H. B. Structural and spectroscopic characterization of active sites in a family of light-emitting sodium lanthanide tetrafluorides. *Angew. Chem. Int. Ed.* **2006**, *45*, 2802–2806

174. Wang, F.; Lin, X. Recent advances in the chemistry of lanthanide-doped upconversion nanocrystals. *Chem. Soc. Rev.* **2009**, *38*, 976–989

175. Wang, G.; Peng, Q.; Li, Y. Lanthanide-doped nanocrystals: synthesis, optical-magnetic properties, and applications. *Acc. Chem. Res.* **2011**, *44*, 322–332

176. Chen, D.; Huang, P. Highly intense upconversion luminescence in Yb/Er:$NaGdF_4$@$NaYF_4$ core-shell nanocrystals with complete shell enclosure of the core. *Dalton Trans.* **2014**, *43*, 11299–11304.

177. Arppe, R.; Hyppänen, I.; Perälä, N.; Peltomaa, R.; Kaiser, M.; Würth, C.; Christ, S.; Resch-Genger, U.; Schäferling, M.; Soukka, T. Quenching of the upconversion luminescence of $NaYF_4$:Yb^{3+},Er^{3+} and $NaYF_4$:Yb^{3+},Tm^{3+} nanophosphors by water: the role of the sensitizer Yb^{3+} in non-radiative relaxation. *Nanoscale* **2015**, *7*, 11746–11757.

178. Kraft, M.; Würth, C.; Muhr, V.; Hirsch, T.; Resch-Genger, U. Particle-size-dependent upconversion luminescence of $NaYF_4$:Yb,Er nanoparticles in organic solvents and water at different excitation power densities. *Nano Res.* **2018**, *11*, 6360–6374.

179. Grauel, B.; Würth, C.; Homann, C.; Krukewitt, L.; Andresen, E.; Roik, J.; Recknagel, S.; Haase, M.; Resch-Genger, U. Volume and surface effects on two-photonic and three-photonic processes in dry co-doped upconversion nanocrystals. *Nano Res.* **2022**, *15*, 2362–2373.

180. Aharoni, A.; Oron, D.; Banin, U.; Rabani, E.; Jortner, J. Long-range electronic-to-vibrational energy transfer from nanocrystals to their surrounding matrix environment. *Phys. Rev. Lett.* **2008**, *100*, 057404.

181. Hyppänen, I.; Höysniemi, N.; Arppe, R.; Schäferling, M.; Soukka, T. Environmental impact on the excitation path of the red upconversion emission of nanocrystalline $NaYF_4$:Yb^{3+},Er^{3+}. *J. Phys. Chem. C* **2017**, *121*, 6924–6929.

182. Hu, Y.; Shao, Q.; Dong, Y.; Jiang, J. Energy loss mechanism of upconversion core/shell nanocrystals. *J. Phys. Chem. C* **2019**, *123*, 22674–22679.

183. Ren, P.; Zheng, X.; Zhang, J.; De Camillis, S.; Jia, J.; Wang, H.; Liao, X.; Piper, J. A.; Lu, Y. Quantifying the influence of inert shell coating on luminescence brightness of lanthanide upconversion nanoparticles. *ACS Photonics* **2022**, *9*, 758–764.

184. Mulder, J. T.; Meijer, M. S.; van Blaaderen, J. J.; du Fosse, I.; Jenkinson, K.; Bals, S.; Manna, L.; Houtepen, A. J. Understanding and preventing photoluminescence quenching to achieve unity photoluminescence quantum yield in Yb:YLF nanocrystals. *ACS Appl. Mater. Interfaces* **2023**, *15*, 3274–3286.

185. Rabouw, F. T.; Prins, P. T.; Villaneuva-Delgado, P.; Castelijns, M.; Geitenbeek, R. G.; Meijerink, A. Quenching pathways in $NaYF_4$:Er^{3+},Yb^{3+} upconversion nanocrystals. *ACS Nano* **2018**, *12*, 4812–4823

186. van Swieten, T. P.; Yu, D.; Yu, T.; Vonk, S. J. W.; Suta, M.; Zhang, Q.; Meijerink, A.; Rabouw, F. T. A Ho^{3+}-based luminescent thermometer for sensitive sensing over a wide temperature range. *Adv. Opt. Mater.* **2021**, *9*, 2001518.

187. Anderson, R. B.; Smith, S. J.; May, P. S.; Berry, M. T. Revisiting the NIR-to-visible upconversion mechanism in β-$NaYF_4$:Yb^{3+},Er^{3+}. *J. Phys. Chem. Lett*. **2014**, *5*, 36–42.

188. Berry, M. T.; May, P. S. Disputed mechanism for NIR-to-red upconversion luminescence in $NaYF_4$:Yb^{3+},Er^{3+}. *J. Phys. Chem. A* **2015**, *119*, 9805–9811.

189. Würth, C.; Kaiser, M.; Wilhelm, S.; Grauel, B.; Hirsch, T.; Resch-Genger, U. Excitation power dependent population pathways and absolute quantum yields of upconversion nanoparticles in different solvents. *Nanoscale* **2017**, *9*, 4283–4294.

190. Kaiser, M.; Würth, C.; Kraft, M.; Hyppänen, I.; Soukka, T.; Resch-Genger, U. Power-dependent upconversion quantum yield of $NaYF_4$:Yb^{3+},Er^{3+} nano- and micrometer-sized particles-measurements and simulations. *Nanoscale* **2017**, *9*, 10051–10058.

191. van Blaaderen, A.; Kentgens, A. P. M. Particle morphology and chemical microstructure of colloidal silica spheres made from alkoxysilanes. *J. Non. Cryst. Sol.* **1992**, *149*, 161–178.

192. Koole, R.; van Schooneveld, M. M.; Hilhorst, J.; de Mello Donega, C.; 't Hart, D. C.; van Blaaderen, A.; Vanmaekelbergh, D.; Meijerink, A. On the incorporation mechanism of hydrophobic quantum dots in silica spheres by a reverse microemulsion method. *Chem. Mater*. **2008**, *20*, 2503–2512.

193. Bazuła, P. A.; Arnal, P. M.; Galeano, C.; Zibrowius, B.; Schmidt, W.; Schüth, F. Highly microporous monodisperse silica spheres synthesized by the Stöber process. *Microporous Mesoporous Mater*. **2014**, *200*, 317–325.

194. SpectraBase, https://spectrabase.com/, (accessed March 20th, 2023), Compound/Spectrum ID = GJRW0aSjL2q, 9IQ9plOczUJ, TR4aB7OBWB, 3yQVfjEXCCn, H7KdKI7UNSz and Dv5ShhC99Xg.

195. NIST Chemistry WebBook, NIST Standard Reference Database Number 69, https://doi.org/10.18434/T4D303, (accessed March 20th, 2023), Spectrum ID = C108883, C110827, B6006735.

196. J. Workman Jr., L. Weyer, in *Practical guide and spectral atlas for interpretive near-infrared spectroscopy*; CRC Press: Boca Raton, FL, 2012, Water, pp 56–61.

197. Huang, B.; Bergstrand, J.; Duan, S.; Zhan, Q.; Widengren, J.; Ågren, H.; Liu, H. Overtone vibrational transition-induced lanthanide excited-state quenching in Yb^{3+}/Er^{3+}-doped upconversion nanocrystals. *ACS Nano* **2018**, *12*, 10572–10575.

198. Krämer, K. W.; Biner, D.; Frei, G.; Güdel, H. U.; Hehlen, M. P.; Lüthi, S. R. Hexagonal sodium yttrium fluoride based green and blue emitting upconversion phosphors. *Chem. Mater*. **2004**, *16*, 1244–1251.

199. Feng, Y.; Li, Z.; Li, Q.; Yuan, J.; Tu, L.; Ning, L.; Zhang, H. Internal OH– induced cascade quenching of upconversion luminescence in $NaYF_4$:Yb/Er nanocrystals. *Light Sci. Appl.* **2021**, *10*, 105.

200. Thommes, M.; Kaneko, K.; Neimark, A. V.; Olivier, J. P.; Rodriguez-Reinoso, F.; Rouquerol, J.; Sing, K. S. W. Physisorption of gases, with special reference to the evaluation of surface area and pore size distribution (IUPAC technical report). *Pure Appl. Chem*. **2015**, *87*, 1051–1069.

201. Piletic, I. R.; Moilanen, D. E.; Spry, D. B.; Levinger, N. E.; Fayer, M. D. Testing the core/shell model of nanoconfined water in reverse micelles using linear and nonlinear IR spectroscopy. *J. Phys. Chem. A* **2006**, *110*, 4985–4999.

202. Moilanen, D. E.; Levinger, N. E.; Spry, D. B.; Fayer, M. D. Confinement or the nature of the interface? Dynamics of Nanoscopic Water. *J. Am. Chem. Soc.* **2007**, *129*, 14311–14318.

203. Toda, S.; Shigeto, S. Distinct effects of external electric field on interfacial and bulk-like water confined in reverse micelles. *J. Phys. Chem. C* **2018**, *122*, 25515–25523.

204. Rinkel, T.; Raj, A. N.; Dühnen, S.; Haase, M. Synthesis of 10 nm β-$NaYF_4$:Yb,Er/$NaYF_4$ core/shell upconversion nanocrystals with 5 nm particle cores. *Angew. Chem. Int. Ed.* **2016**, *55*, 1164–1167.

205. Takahashi, R.; Sato, S.; Sodesawa, T.; Kawakita, M.; Ogura, K. High surface-area silica with controlled pore size prepared from nanocomposite of silica and citric acid. *J. Phys. Chem. B* **2000**, *104*, 12184–12191.

206. Lin, C. H.; Chang, J. H.; Yeh, Y. Q.; Wu, S. H.; Liu, Y. H.; Mou, C. Y. Formation of hollow silica nanospheres by reverse microemulsion. *Nanoscale* **2015**, *7*, 9614–9626.

207. Gorelikov, I.; Matsuura, N. Single-step coating of mesoporous silica on cetyltrimethyl ammonium bromide-capped nanoparticles. *Nano Lett*. **2008**, *8*, 369–373.

208. Li, D.; Shao, Q.; Dong, Y.; Jiang, J. Anomalous temperature-dependent upconversion luminescence of small-sized $NaYF_4$:Yb^{3+}, Er^{3+} nanoparticles. *J. Phys. Chem. C* **2014**, *118*, 22807–22813.

209. Shi, R.; Martinez, E. D.; Brites, C. D. S.; Carlos, L. D. Thermal enhancement of upconversion emission in nanocrystals: a comprehensive summary. *Phys. Chem. Chem. Phys.* **2021**, *23*, 20–42.

210. Zhou, Y.; Cheng, Y.; Huang, Q.; Xu, J.; Lin, H.; Wang, Y. Abnormal thermally enhanced upconversion luminescence of lanthanide-doped phosphors: proposed mechanisms and potential applications. *J. Mater. Chem. C.* **2021**, *9*, 2220–2230.

211. Suyver, J. F.; Grimm, J.; Krämer, K. W.; Güdel, H. U. Highly efficient near-infrared to visible up-conversion process in $NaYF_4$:Er^{3+},Yb^{3+}. *J. Lumin.* **2005**, *114*, 53–59.

212. Chen, B.; Kong, W.; Wang, N.; Zhu, G.; Wang, F. Oleylamine-mediated synthesis of small $NaYbF_4$ nanoparticles with tunable size. *Chem. Mater*. **2019**, *31*, 4779–4786.

213. Shao, Q.; Zhang, G.; Ouyang, L.; Hu, Y.; Dong, Y.; Jiang, J. Emission color tuning of core/shell upconversion nanoparticles through modulation of laser power or temperature. *Nanoscale* **2017**, *9*, 12132–12141.

214. Hu, Y.; Shao, Q.; Zhang, P.; Dong, Y.; Fang, F.; Jiang, J. Mechanistic investigations on the dramatic thermally induced luminescence enhancement in upconversion nanocrystals. *J. Phys. Chem. C* **2018**, *122*, 26142–26152.

215. Wang, Z.; Christiansen, J.; Wezendonk, D.; Xie, X.; van Huis, M. A.; Meijerink, A. Thermal enhancement and quenching of upconversion emission in nanocrystals. *Nanoscale* **2019**, *11*, 12188–12197.

216. Lemmon, E. W. *Fluid Properties: Vapor Pressure, Enthalpy of Vaporization, and Surface Tension of Water*. In *CRC Handbook of Chemistry and Physics* (Internet Version); Rumble, J. R., Ed.; CRC Press/Taylor & Francis: Boca Raton, FL, 2022.

217. Baumgartner, B.; Hayden, J.; Lendl, B. Mesoporous silica films for sensing volatile organic compounds using attenuated total reflection spectroscopy. *Sens. Actuators B: Chem.* **2020**, *302*, 127194.

218. Baumgartner, B.; Mashita, R.; Fukatsu, A.; Okada, K.; Takahashi, M. Guest alignment and defect formation during pore filling in metal–organic framework films. *Angew. Chem. Int. Ed*. **2022**, *61*, e202201725.

219. Sharpe, S. W.; Johnson, T. J.; Sams, R. L.; Chu, P. M.; Rhoderick, G. C.; Johnson, P. A. Gas-phase databases for quantitative infrared spectroscopy. *Appl. Spectrosc*. **2004**, *58*, 1452–1461.

220. Villanueva-Delgado, P.; Biner, D.; Krämer, K. W. Judd–Ofelt analysis of β-NaGdF4: Yb3+, Tm3+ and β-$NaGdF_4$:Er^{3+} single crystals. *J Lumin.* **2017**, *189*, 84–90.

221. Himmelstoss, S. F.; Hirsch, T. Long-term colloidal and chemical stability in aqueous media of $NaYF_4$-type upconversion nanoparticles modified by ligand-exchange. *Part. Part. Syst. Charact*. **2019**, *36*, 1900235

222. NIST Chemistry WebBook, *NIST Standard Reference Database Number 69*, https://doi.org/10.18434/T4D303, (accessed March 20th, 2023), Spectrum ID = C108883, C108941, C67641, C64175.

223. Kubendhiran, S.; Bao, Z.; Dave, K.; Liu, R. S. Microfluidic synthesis of semiconducting colloidal quantum dots and their applications. *ACS Appl. Nano Mater.* **2019**, *2*, 1773–1790.

224. Baek, J.; Shen, Y.; Lignos, I.; Bawendi, M. G.; Jensen, K. F. Multistage microfluidic platform for the continuous synthesis of III–V core/shell quantum dots. *Angew. Chem*. **2018**, *130*, 11081–11084.

225. Nightingale, A. M.; De Mello, J. C. Microscale synthesis of quantum dots. *J. Mater. Chem.* **2010**, *20*, 8454–8463.

226. Edel, J. B.; Fortt, R.; De Mello, J. C.; De Mello, A. J. Microfluidic routes to the controlled production of nanoparticles. *Chem. Commun*. **2002**, *2*, 1136–1137.

227. Krishnadasan, S.; Brown, R. J. C.; De Mello, A. J.; De Mello, J. C. Intelligent routes to the controlled synthesis of nanoparticles. *Lab Chip* **2007**, *7*, 1434–1441

Samenvatting in het Nederlands

Wat zou er overblijven van onze maatschappij, als we afscheid moesten nemen van kunstmatige lichtbronnen? Een straat zonder straatverlichting, een kantoor zonder computer, en een tiener zonder smartphone. Het spreekt voor zich dat kunstmatige lichtbronnen onmisbaar zijn. De consument is veeleisend en vraagt om lichtbronnen met eigenschappen die geschikt zijn voor gebruik in verschillende apparaten. Denk bijvoorbeeld aan televisies of smartphones die heldere en zuivere kleuren moeten laten zien, of de woonkamerlamp die juist warm wit licht moet geven. We zijn continu opzoek naar nieuwe soorten lichtgevende materialen, om te blijven voldoen aan de uiteenlopende wensen van de consument en om nieuwe technologieën te ontwikkelen, zoals sensoren voor temperatuur of chemicaliën.

In dit proefschrift hebben we materialen bestudeerd die licht geven op basis van fotoluminescentie. Fotoluminescente materialen zijn in staat om licht van een bepaalde kleur te absorberen, om daarna zelf een andere kleur licht uit te zenden. Het doel van ons onderzoek is niet alleen om beter te begrijpen hoe fotoluminescentie werkt in deze materialen, maar ook om inzicht te krijgen in processen die fotoluminescentie verstoren. We richten ons op twee soorten lichtgevende materialen: kwantumstippen en lanthanide-gedoteerde nanokristallen.

Om het vervolg van deze samenvatting goed te begrijpen, is het belangrijk om te beseffen dat licht bestaat uit deeltjes, die we fotonen noemen. Een foton draagt een bepaalde hoeveelheid energie met zich mee en kan dus ook wel gezien worden als een energiepakketje. De hoeveelheid energie in zo'n pakketje is afhankelijk van de kleur licht: een blauw foton heeft meer energie dan een groen foton, dat op zijn beurt weer meer energie heeft dan een rood foton.

Nieuwe kwantumstippen: kleurrijk en milieuvriendelijk

Kwantumstippen bestaan slechts uit duizenden atomen, waardoor ze ongeveer duizend tot tienduizend keer in de dikte van een menselijke haar passen. In vergelijking met traditionele lichtbronnen zijn kwantumstippen in staat om zuiverdere en helderdere kleuren uit te zenden, waardoor ze inmiddels al commercieel gebruikt worden in sommige televisies. Blauw licht wordt door kwantumstippen van verschillende groottes omgezet in verschillende andere kleuren licht, zoals groen of rood. Zo zijn kwantumstippen van verschillende groottes in staat om blauw licht om te zetten in verschillende kleuren, zoals groen en rood. Door de kleuren blauw, groen en rood te combineren kunnen we alle kleuren licht maken die het menselijk oog kan waarnemen.

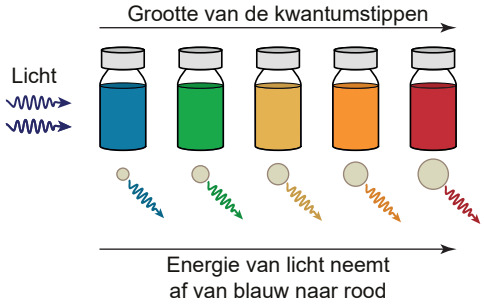

Wanneer we blauw licht schijnen op kleine kwantumstippen, zullen ze bijna dezelfde kleur blauw licht uitzenden. Grotere kwantumstippen zullen datzelfde blauwe licht omzetten in rood licht. Hoe groter de kwantumstip, hoe lager de energie is van het licht dat wordt uitgezonden.

Figuur 1 | Grootte-afhankelijke fotoluminescentiekleur van kwantumstippen.

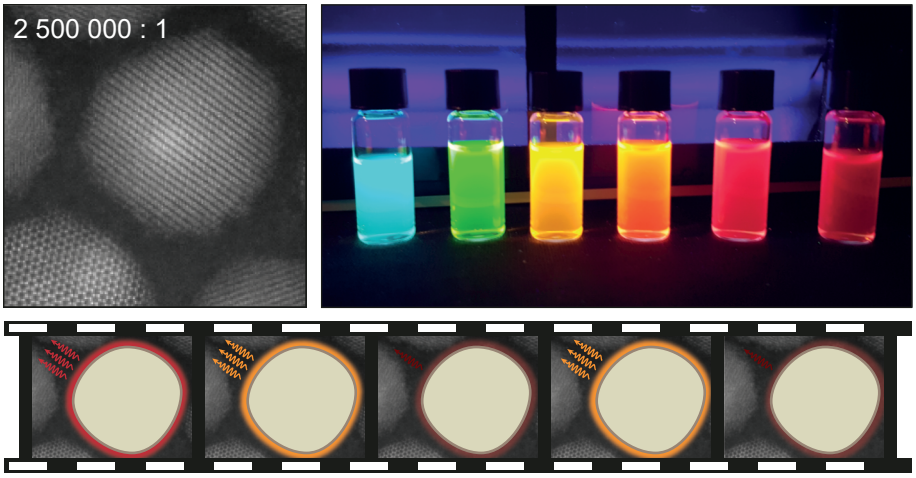

Figuur 2 | Experimenten met kwantumstippen. Linksboven: een kwantumstip in beeld gebracht met een geavanceerde elektronenmicroscoop van de Universiteit van Antwerpen. De vergroting is 2,5 miljoen keer. De kwantumstip is ongeveer bolvormig, maar niet helemaal perfect. Rechtsboven: kwantumstippen in oplossing die met ultraviolet (UV) licht worden beschenen. Onder: wanneer we een enkele kwantumstip filmen met een optische microscoop, zien we dat de eigenschappen in de loop van tijd variëren. Zo kan dezelfde kwantumstip het ene moment fel oranje licht uitzenden, en het andere moment zwak rood licht. Het tegengaan van deze ongewenste fluctuaties blijft tot op heden een uitdaging.

De bekendste soort kwantumstippen bestaat uit een rooster van cadmiumatomen (Cd) en seleniumatomen (Se). Deze CdSe-gebaseerde kwantumstippen zijn in staat om licht met veel energie om te zetten in licht met minder energie. Het gebruik van kwantumstippen op basis van cadmium is echter verboden, omdat het giftig is. Onderzoekers houden zich daarom bezig met het vinden van alternatieve, milieuvriendelijke bouwstenen voor kwantumstippen. Kwantumstippen op basis van koperindiumsulfide (KIS) of indiumfosfide (InP) zijn interessante kandidaten, maar vormen op dit moment nog geen gelijkwaardig alternatief. In **Hoofdstuk 3** en **Hoofdstuk 4** bestuderen we hun fotoluminescentie.

Om de eigenschappen van KIS- en InP-kwantumstippen beter te begrijpen hebben wij ze onder een optische microscoop bekeken. Een verrassende waarneming was dat zowel de kleur als de felheid van deze kwantumstippen fluctueert. We hebben bijvoorbeeld gezien dat een kwantumstip het ene moment fel oranje licht uitstraalt, maar het andere moment zwak rood licht. Schommelingen in kleur en felheid leveren minder zuiver en minder helder licht op, wat verklaart waarom de fotoluminescentie afkomstig van KIS- en InP-kwantumstippen zoveel minder mooi is dan het licht afkomstig van traditionele CdSe-kwantumstippen. Door fluctuaties in kleur en felheid te bestuderen hebben wij inzichten gekregen in het mechanisme van fotoluminescentie. Scheikundigen kunnen deze inzichten gebruiken om in de toekomst betere kwantumstippen te maken, die continu dezelfde heldere kleur licht uitzenden zonder schommelingen in felheid.

De fotoluminescentie van lanthaniden wordt bepaald door hun omgeving

Nanokristallen zijn de tweede soort lichtgevende stoffen die we hebben onderzocht. Nanokristallen zijn ongeveer even groot als kwantumstippen, en bestaan ook uit enkele duizenden tot tienduizenden atomen. Hun gedrag is echter fundamenteel anders: ze geven van zichzelf geen licht, maar doen dit pas wanneer bepaalde onzuiverheden in het kristal worden ingebouwd. Scheikundigen kunnen de eigenschappen van nanokristallen bepalen door te kiezen welke lichtgevende atomen ze inbouwen. De atomen die wij gebruikt hebben heten lanthaniden. Dit zijn scheikundige elementen, waaronder de atoomsoorten erbium, terbium, en ytterbium vallen.

In **Hoofdstuk 5** hebben we nanokristallen bestudeerd met daarin de lanthanide-elementen terbium en ytterbium ingebouwd. Dankzij de combinatie van terbium- en ytterbiumatomen gedragen deze nanokristallen zich als kwantumknippers. Kwantumknippers zijn in staat om één blauw foton (met veel energie) op te knippen in twee fotonen met ieder de helft van de energie. Zo ontstaan twee nabij-infrarode fotonen die net iets minder energie bevatten dan rode fotonen. Nabij-infrarood licht kan niet waargenomen worden met het menselijk oog. Wij hebben factoren ontdekt die de efficiëntie van kwantumknippen bepalen (zoals de grootte van de nanokristallen) en hebben manieren gevonden om kwantumknippers effectiever te maken.

Deze effectievere kwantumknippers zijn veelbelovend om zonlicht efficiënter om te zetten in zonne-energie. Zonnecellen kunnen slechts een bepaalde hoeveelheid energie van een foton omzetten in nuttige energie voor het opwekken van stroom. Als een foton teveel energie heeft, gaat het energieoverschot verloren in de vorm van warmte. Om die reden levert één blauw foton net zoveel energie op als één nabij-infrarood foton, ondanks het feit dat een blauw foton meer energie met zich mee draagt dan een nabij-infrarood foton. Als we kwantumknippers gebruiken om blauwe fotonen op te knippen in tweemaal zoveel nabij-infrarode fotonen,

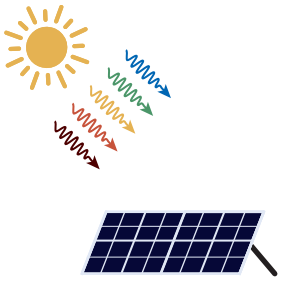

Zonlicht is een verdeling van alle kleuren fotonen. Dat omvat zichtbaar licht, maar ook UV, en (nabij-)infrarood.

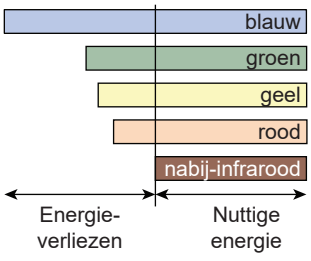

Niet alle kleuren fotonen zijn even effectief: blauwe fotonen hebben meer energie dan rode of nabij-infrarode fotonen maar leveren evenveel stroom op.

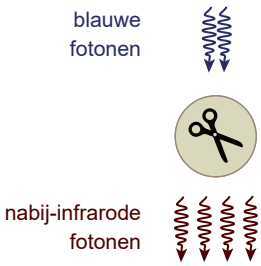

Kwantumknippers gebruiken de niet-nuttige energie van een blauw foton om twee nabij-infrarode fotonen te maken. Dat levert dubbel zoveel stroom op.

Figuur 3 | Kwantumknippers voor efficiëntere zonnecellen. Nanokristallen met de lanthaniden terbium en ytterbium zetten blauwe fotonen van zonlicht om in twee keer zoveel nabij-infrarode fotonen. Grote (nano)kristallen zijn efficiëntere kwantumknippers dan kleine nanokristallen.

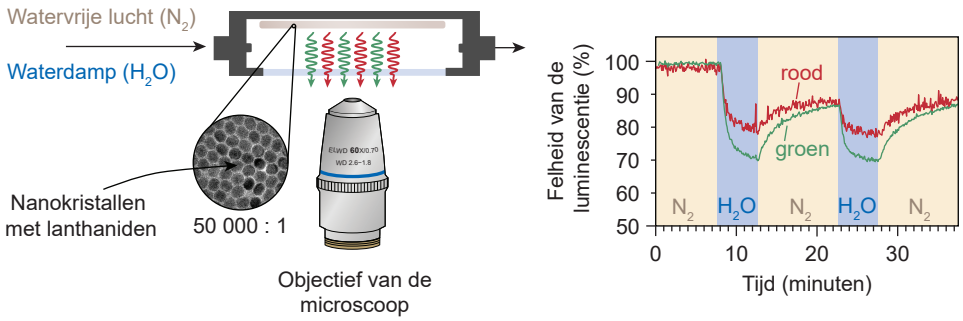

Figuur 4 | Fotoluminescentie van erbium-houdende sensor-nanokristallen. Links: experiment waarbij een laagje met sensor-nanokristallen afwisselend wordt blootgesteld aan watervrije lucht (N_2), of juist lucht met waterdamp (H_2O) daarin. We bekijken onder een microscoop welke kleur licht wordt uitgezonden door de sensor-nanokristallen. Rechts: resultaten van het experiment, waarin we zien dat de rode en groene luminescentie van erbium afzwakt in felheid in de periodes dat de sensor-nanokristallen zijn blootgesteld aan waterdamp, maar weer herstelt als de lucht weer watervrij wordt gemaakt.

kunnen we het zonlicht effectiever gebruiken om zonne-energie mee op te wekken. Er gaat dan minder energie verloren als warmte.

In **Hoofdstuk 6** hebben we onderzoek gedaan naar nanokristallen waarin een ander lanthanide-element is ingebouwd: erbium. Deze nanokristallen gedragen zich heel anders dan de eerder genoemde kwantumknippers, die geen erbium bevatten, maar terbium én ytterbium. Wij hebben waargenomen dat erbiumatomen een deel van hun energie kunnen afgeven aan moleculen in de omgeving. Hierdoor houden de erbiumatomen zelf minder energie over en zenden ze ander licht uit. Dit soort energieoverdracht gaat efficiënt als er specifieke moleculen in de omgeving van de nanokristallen aanwezig zijn, maar minder goed of helemaal niet als de omgeving bestaat uit andere moleculen. Door te kijken naar het licht dat wordt uitgezonden zijn we in staat om moleculen te detecteren. Zo werken onze nanokristallen met erbium-atomen als sensoren voor moleculen. We kunnen er bijvoorbeeld watermoleculen (H_2O) in lucht mee opsporen, zoals omschreven in Figuur 4. Het detecteren of opsporen van chemicaliën op basis van onze sensor-nanokristallen kan nuttig zijn voor verschillende toepassingen, zoals het volgen van een chemische reactie.

Hoe nu verder?

Lichtgevende materialen zijn een onmisbaar onderdeel van ons dagelijks leven, en dat zullen ze ook altijd blijven. Het onderzoek uit dit proefschrift helpt ons om fotoluminescentie in kwantumstippen en lanthanide-gebaseerde materialen beter te begrijpen. De toekomst zal uitwijzen of deze inzichten gebruikt gaan worden om bestaande apparaten te verbeteren, of misschien zelfs om verrassende nieuwe technologieën te ontwikkelen.

Acknowledgements

Dankwoord

We zijn aanbeland bij het dankwoord. Dat betekent gek genoeg dat mijn tijd aan de Universiteit Utrecht na bijna 10 jaar op zijn eind loopt. Met de eindstreep van deze metaforische marathon in zicht wil ik graag een aantal mensen bedanken. Zij hebben voor mij het parcours uitgezet, me op weg geholpen, en vooruit geschreeuwd. Dankzij hun steun heb ik het parcours grotendeels met een lach op mijn gezicht kunnen doorlopen.

Ik wil graag bij jou beginnen, **Freddy**. Toen je mij in 2015 als bachelorstudent begeleidde bij het schrijven van mijn onderzoeksvoorstel, had je zelf net je eigen proefschrift afgemaakt. Ik heb dat boekje altijd als een groot voorbeeld gezien. Ik hoefde niet lang na te denken, toen je me benaderde met de vraag of ik een PhD-project in jouw groep wilde doen. Je hebt me de kans gegeven om zo veel mogelijk zelf mijn onderzoek vorm te geven, waar ik veel van heb geleerd. Ondanks je vrije aanpak, was je altijd benaderbaar en snel met feedback. Jouw sterke theoretische achtergrond en wetenschappelijke intuïtie hebben me gelukkig vaak de goede kant op gestuurd. We konden het goed met elkaar vinden en ik vond het leuk om samen te klieren en grappen te maken. Daarnaast ben ik trots op het feit dat ik jou heb kunnen helpen bij het behalen van mijlpalen zoals het uitlopen van je eerste 21,1 kilometer (zonder klagen). Ongetwijfeld zul je me ook in de toekomst op de hoogte houden van de laatste roddels, bijvoorbeeld tijdens een rondje hardlopen.

Bert, hoewel mijn onderzoek maar weinig overlap had met katalyse, ben je toch zeer betrokken geweest. Je was altijd geïnteresseerd als we mijn resultaten bespraken en je motiveerde met je enthousiasme over projecten waarin ik het zelf nog niet helemaal zag zitten. Ik bewonder jouw kritische blik en je vermogen om de bredere context van een project te zien.

Alfons, jouw enorme kennis van de wetenschappelijke literatuur is voor veel mensen in de groep van grote waarde. Je hebt een sterk gevoel voor veelbelovende experimenten, die je ook tijdens onze discussies over mijn experimenten vaak aandroeg. Het was een prettige gedachte om mijn resultaten met jou te kunnen bespreken.

Andries, ook jij hebt een grote rol gespeeld in mijn periode aan de UU. Vanaf mijn eerste studiejaar ben ik door jouw colleges geënthousiasmeerd geraakt over luminescentie en spectroscopie, en later mocht ik samen met Freddy, Robin en Mathijs aan de slag op een project over kwantumknippende nanokristallen. Tijdens mijn PhD mocht ik ook nog geregeld bij je aankloppen, waarna we leuke discussies hebben gehad over lanthaniden en quantum dots.

Stijn, als échte allround-wetenschapper deinsde je er niet voor terug om het chemisch lab op te gaan (als enige braveling ooit?), en jouw microscopie-vakmanschap vormt nog steeds de basis voor hoe wij onze optische experimenten doen. Je hebt me wegwijs gemaakt met de opstelling, en later ook met de data-analyse, waarvoor ik je heel dankbaar ben. Daarnaast kon ik altijd lachen om je humor, vooral als je even wat minder braaf was dan iedereen van je zou verwachten.

Sander, jouw handigheid en doortastendheid op het lab maken je een sterke onderzoeker, zeker in combinatie met jouw theoretische vaardigheden. Als kantoorgenoot in OL 0.18 dacht je vaak mee over mijn experimenten en resultaten en ik heb heel veel aan je input gehad. Het was daarnaast altijd gezellig op ons kantoor en tijdens onze reisjes naar Gent, Bad Honnef en Bünzliland. Ik ben benieuwd hoe jouw pad verder loopt na het afronden van je mooie onderzoek in Utrecht.

Tijdens mijn PhD heb ik een aantal studenten mogen begeleiden bij hun BSc. en MSc. projecten. **Martijn**, dankjewel voor je enthousiasme en je mooie simulaties over anion-exchange in perovskieten. **Mitchell**, jouw enthousiasme werkte aanstekelijk. Het was een genot om samen met jou en **Thomas** te werken aan de temperatuur-afhankelijke eigenschappen van perovskietjes. **Sten**, jij hebt interessante inzichten gevonden over de potentie van inverted-shell lanthanide-gedoteerde nanokristallen. Helaas bleek het in de praktijk lastig om met ze te werken. **Ayla**, jij werkte als bachelorstudent op een bijzonder hoog niveau. Het is een mooi vooruitzicht voor de groep dat je straks als nieuwste braveling wordt gepresenteerd. **Jeffrey**, je hebt bevlogen gewerkt aan kwantumknippers. Ik ben benieuwd of ze daadwerkelijk gebruikt gaan worden in zonnepanelen. **Larse**, jij was mijn laatste student. Jouw metingen met de VAHEAT opstelling gaan ongetwijfeld nog een aanzet vormen tot veelbelovende experimenten.

Jur, het was lekker om na een zware ochtend of middag bij jou langs te kunnen lopen voor een potje pingpong. Dat pingpongen werkte meestal niet bevorderend voor mijn zelfvertrouwen maar was wel altijd gezellig. Samen met **Luc** spraken we ook regelmatig af voor een avond vol culinaire hoogstandjes, waar ik vaak erg naar uit zag.

Erik, hoewel we allebei onze experimenten hebben gedaan op de microscoop, verschilden onze onderwerpen nogal. Desondanks kwamen we elkaar geregeld tegen om even te lachen over van alles en nog wat, bijvoorbeeld bij de MCEC events of andere borrels. Dankjewel ook voor je hulp met het opmaken van dit proefschrift in InDesign.

Thomas, ook met jou was het altijd gezellig. Toen ik zelf nog toekomst zag in perovskieten, maakte ik nog wel eens flauwe opmerkingen over jouw 'laffe emitters'. Ik beloof je dat ik in de toekomst nooit meer zo over "jouw" lanthaniden zal praten.

Tim, jij bent enorm goed op de hoogte van de literatuur over zowel quantum dots als lanthaniden. Je had vaak leuke en realistische ideeën voor experimenten (een bijzondere combinatie). Richting het einde van mijn PhD-project heb je me geholpen om het initiatief te pakken en daar ben ik je heel dankbaar voor.

Maarten, gedurende bijna mijn hele PhD-project was je een gewaardeerd medebewoner van kantoor OL 0.18. Het was leuk om met je te discussiëren over van alles. **Vincent**, dankjewel voor je enthousiasme en vrolijkheid. Ik heb fijn met je gewerkt om samen de laatste mooie resultaten binnen kunnen halen waarmee ik dit proefschrift af kon sluiten. **Tjom**, jij was mijn laatste kantoorgenoot in OL 0.18. Ik ben benieuwd naar je toekomstige vindingen op het gebied van correlatie-analyse, waar je altijd enthousiast over sprak. Ik wil graag alle andere bravelingen bedanken voor de leuke meetings in het Ornsteingebouw: **Robin**, **Huygen**, **Thimo**, **Just Pé**, **Raimon** en **Rafael**. Daarnaast wil ik graag alle collega's van de **SCMB**-groep, de **ICC**-groep en het **MCEC**-consortium bedanken voor de gezellige sfeer.

I would like to express my gratitude to all people with whom I collaborated. **Bettina**, I very much enjoyed working with you on the lanthanide-doped nanocrystals. Your ATR setup and your sensing background gave the project with lanthanide sensors a great impulse. **Tom**, dankjewel voor je mooie COMSOL berekeningen van de local-field factors. **Jaco** en **Arjan** (Houtepen), bedankt voor de interessante discussies over de experimenten met CdSe en InP-gebaseerde quantum dots.

Niet alle experimenten waren meteen een doorslaand succes. Desondanks dragen alle minder goed gelukte experimenten bij aan het vinden van meer veelbelovende experimenten. **Bas** en **Jara**, de single-particle metingen op nanoringen bleken helaas te lastig, maar waren in potentie erg interessant. Wie weet komt er binnenkort een procedure om stabielere deeltjes te maken die we beter kunnen meten. **Raimon**, the multiparticle spectroscopy experiments with your pretty CIS quantum dots were very challenging but nonetheless exciting.

Relinde, **Elleke**, **Peter** en **Dave**, dankjewel voor jullie hulp bij experimenten en labbenodigdheden. **Hester**, bedankt voor alle hulp met secretariële zaken.

Tot slot mijn trouwe supporters aan de zijlijn. **Pappa**, **Mamma**, **Tom** en **Laurèlle**, en **Annemarie**, het was fijn om thuis even niet over lichtgevende deeltjes en andere werkzaken te praten. Ik vond het leuk om met jullie feedback en input een mooie populaire samenvatting van mijn onderzoek te schrijven. **Oma**, je zal het wel vermoeiend hebben gevonden, om te horen dat ik na al die jaren nog stéédS bezig was met "*nano*". **Opa**, ik weet nog goed hoe ik op de middelbare school een dagje heb gespijbeld om samen met jou in de sprinter naar Delft te gaan voor een open dag van de studie scheikunde. En dan jij als allerlaatste, **Celine**. We houden van het Bourgondische leven, en met jou kan ik altijd goed ontspannen. Het was niet altijd makkelijk om mij op te peppen, maar als iemand het kan dan ben jij het wel. Dankjewel voor alle mooie momenten samen. Ik zie uit naar nog vele mooie jaren samen.

List of publications

1. **Probing nearby molecular vibrations with lanthanide-doped nanocrystals.**
Mangnus, M. J. J.; Benning, V. R. M.; Baumgartner, B.; Prins, P. T.; van Swieten, T. P.; Dekker, A. J. H.; van Blaaderen, A.; Weckhuysen, B. M. W.; Meijerink, A.; Rabouw, F. T.
Nanoscale **2023**, *15*, 16601–16611

2. **High-throughput characterization of single-quantum-dot emission spectra and spectral diffusion by multiparticle spectroscopy.**
Mangnus, M. J. J.; de Wit, J. W.; Vonk, S. J. W.; Geuchies, J. J. G.; Albrecht, W.; Bals, S.; Houtepen, A. J.; Rabouw, F. T.
ACS Photonics **2023**, *10*, 2688–2698

3. **Slow hole localization and fast electron cooling in Cu-doped InP/ZnSe quantum dots.**
Prins, P. T.; Spruijt, D. A. W.; Mangnus, M. J. J.; Rabouw, F. T.; Vanmaekelbergh, D.; de Mello Donega, C.; Geiregat, P.
The Journal of Physical Chemistry Letters **2022**, *13*, 9950–9956

4. **Charge transport in topological graphene nanoribbons and nanoribbon heterostructures.**
Mangnus, M. J. J.; Fischer, F. R.; Crommie, M. F.; Swart, I.; Jacobse, P. H.
Physical Review B **2022**, *105*, 115424

5. **Finite-size effects on energy transfer between dopants in nanocrystals.**
Mangnus, M. J. J.; Zom, J.; Welling, T. A. J.; Meijerink, A.; Rabouw, F. T.
ACS Nanoscience Au **2021**, *2*, 111–118

6. **Unusual spectral diffusion of single $CuInS_2$ quantum dots sheds light on the mechanism of radiative decay.**
Hinterding, S. O. M.; Mangnus, M. J. J.; Prins, P. T.; Jöbsis, H. J.; Busatto, S.; Vanmaekelbergh, D.; de Mello Donega, C.; Rabouw, F.T.
Nano Letters **2021**, *21*, 658–665

7. **Trapping and detrapping in colloidal perovskite nanoplatelets: elucidation and prevention of nonradiative processes through chemical treatment.**
Vonk, S. J. W.; Fridriksson, M. B.; Hinterding, S. O. M.; Mangnus, M. J. J.; van Swieten, T. P.; Grozema, F. C.; Rabouw, F. T.; van der Stam, W.
The Journal of Physical Chemistry C **2020**, *14*, 8047–8054

8. **One precursor but two types of graphene nanoribbons: on-surface transformations of 10, 10'-dichloro-9, 9'-bianthryl on Ag(111).**
Jacobse, P. H.; Simonov, K. A.; Mangnus, M. J. J.; Svirskiy, G. I.; Generalov, A. V.; Vinogradov, A. S.; Sandell, A.; Mårtensson, N.; Preobajenski, A. B.; Swart, I.
The Journal of Physical Chemistry C **2019**, *123*, 8892–8901

9. **Optoelectronic properties of ternary I-III-VI_2 semiconductor nanocrystals: bright prospects with elusive origins.**
Berends, A. C.; Mangnus, M. J. J.; Xia, C.; Rabouw, F. T.; de Mello Donega, C.
The Journal of Physical Chemistry Letters **2019**, *10*, 1600–1616

10. **Mapping the conductance of electronically decoupled graphene nanoribbons.**
Jacobse, P. H.; Mangnus, M. J. J.; Zevenhuizen, S. J. M.; Swart, I.
ACS Nano **2018**, *12*, 7048–7056

List of presentations

Tracking diffusion with perovskite quantum dots (poster)
MCEC annual meeting, Enschede, the Netherlands, June 2019

Dynamics of anion-exchange reactions in perovskite nanocrystals (poster)
Physics@Veldhoven, Veldhoven, the Netherlands, January 2020

Dynamics of anion-exchange reactions in perovskite nanocrystals (e-poster)
nanoGe online meetup conference, online seminar, May 2020

Unusual spectral diffusion of single CuInS2 quantum dots sheds light on the mechanism of radiative decay (oral)
Let's get physical, Ghent, September 2021

Finite-size effects on energy transfer between dopants in nanocrystals (e-poster)
NWO Chains, Veldhoven, the Netherlands, December 2021

Finite-size effects on energy transfer between dopants in nanocrystals (e-poster, video)
Physics@Veldhoven, Veldhoven, the Netherlands, February 2022

Finite-size effects on energy transfer between dopants in nanocrystals (poster)
Wilhelm und Else Heraeus-Seminar on Optoelectronic processes at nanostructured interfaces, Bad Honnef, Germany, March 2022 (winner of the poster prize)

Detecting molecular vibrations with lanthanide-based nanosensors (oral)
MCEC annual meeting, Utrecht, the Netherlands, June 2022

Blinking and spectral diffusion of single colloidal quantum dots at device temperatures (poster)
Gordon Research Conference (GRC) on Colloidal Semiconductor Nanocrystals, les Diablerets, Switzerland, July 2022

Finite-size effects on energy transfer between dopants in nanocrystals (oral)
NWO Chains, Veldhoven, the Netherlands, September 2022

About the author

Mark Mangnus was born in Goes, the Netherlands, on June 6th 1996. He graduated from Regionale Scholengemeenschap 't Rijks, Bergen op Zoom, in 2013. After that, he moved to Utrecht, where he studied chemistry at Utrecht University. He obtained his bachelor's degree *cum laude* in 2016, after completing his thesis on lanthanide-doped quantum-cutting nanocrystals, under supervision of Andries Meijerink, Freddy Rabouw, Mathijs de Jong and Robin Geitenbeek. After a summer internship at Philips Lighting, he continued his studies in nanomaterials science. His master's project, supervised by Ingmar Swart and Peter Jacobse, focused on the formation and electronic properties of graphene nanoribbons. To conclude his master's programme, Mark did a research internship at the ETH Zurich, where he fabricated optical nano-antennas and modelled their optical properties under supervision of David Norris and Nolan Lassaline. He obtained his master's degree cum laude in 2018. The scientific work he did during his master's programme contributed to 4 scientific publications.

Mark returned to Utrecht at the beginning of 2019, as a PhD-candiate within the Multiscale Catalytic Energy Conversion (MCEC) consortium under the supervision of Freddy Rabouw, Alfons van Blaaderen and Bert Weckhuysen. His work focused on photoluminescent nanomaterials, including quantum dots and lanthanide-doped nanocrystals. He performed nanocrystal synthesis, designed and built experimental setups, and carried out data analysis and theoretical modelling. The most important results of his work are described in this thesis and were presented to the scientific community at international meetings and conferences. During his PhD, Mark was a representative for fellow PhD-students in the Debye PhD Committee. He was a teaching assistant in several courses and supervised 3 master's and 3 bachelor's students during their final research projects.